8-2011

DISCOVERY AND DEVELOPMENT OF RARE EARTH ACTIVATED BINARY METAL HALIDE SCINTILLATORS FOR NEXT GENERATION RADIATION DETECTORS

Kan Yang
kyang5@utk.edu

To the Graduate Council:

I am submitting herewith a dissertation written by Kan Yang entitled "DISCOVERY AND DEVELOPMENT OF RARE EARTH ACTIVATED BINARY METAL HALIDE SCINTILLATORS FOR NEXT GENERATION RADIATION DETECTORS." I have examined the final electronic copy of this dissertation for form and content and recommend that it be accepted in partial fulfillment of the requirements for the degree of Doctor of Philosophy, with a major in Materials Science and Engineering.

Charles L. Melcher, Major Professor

We have read this dissertation and recommend its acceptance:

Philip D. Rack, Lars Eriksson, Laurence F. Miller

Accepted for the Council:

Carolyn R. Hodges

Vice Provost and Dean of the Graduate School

(Original signatures are on file with official student records.)

DISCOVERY AND DEVELOPMENT OF RARE EARTH ACTIVATED BINARY METAL HALIDE SCINTILLATORS FOR NEXT GENERATION RADIATION DETECTORS

A Dissertation Presented for the

Doctor of Philosophy

Degree

The University of Tennessee, Knoxville

Kan Yang (杨侃)

August 2011

TO XIANG

给吴翔

ACKNOWLEDGEMENTS

I would first like to express my sincere appreciation to my academic advisor, Dr. Chuck Melcher, for his guidance, mentoring, support and friendship. Dr. Chuck Melcher is an exceptional advisor and marvelous human being to work with. I am very grateful for all the freedom of thought, inspiration and support he provided throughout my entire graduate career. I feel fortunate that I came to the Scintillation Materials Research Center five years ago. I would not have made it to where I am today without the support from him.

I would like to thank Merry Koschan for introducing me into the world of crystal growth, for giving me all the priceless advices, and for her thoughtfulness which bonds our research group together like a family. I would send my special thanks to Dr. Mariya Zhuravleva for being the best research partner. I truly appreciate the fruitful discussions with her and her valuable comments.

I would like to thank all my dissertation committee members, Dr. Lars Eriksson, Dr. Philip Rack and Dr. Laurence Miller, for giving their time to read and advise on this dissertation. I would to express my thanks to Harold Rothfuss for sharing his knowledge of nuclear instrumentations, furnace design and being my best friend; to Dr. Jonathan Peak for his insightful comments about Ce luminescence; to Dr. Piotr Szupryczynski for valuable discussions about scintillation mechanisms and the industrial needs for scintillation materials; to Dr.

George Schweitzer for being our chemistry guru and helping with improving the design of crystal growth ampoule.

A special thank would be given to Arthur (Art) Pratt for his excellent glass-blowing service. I would not be able to grow any halide single crystal without quartz ampoules made by Art.

I would thank Doug Fielden, Larry Smith and Danny Hackworth for their excellent mechanical service. It was a real pleasure to work with them. I would like to thank Matthew Urffer for helping with neutron measurements, thank Andrew Chuang and Dr. Peter Liaw for helping with DSC measurements. I would like to thank my past and present colleagues in the Scintillation Materials Research Center. Paul Cutler, Kurt Johanns, Hua Wei, Jon Bohling, Brandon Goodwin, Bonnie Blalock, Brett Lewis, Aaron Hall and Breana Harvell. I have enjoyed working with them and appreciated their support to my research.

I would also like to thank my parents Shaoqing Yang and Yeqing Wu for their love and support throughout my life. It was them who supported me to come to the United States to pursue my Ph.D at the first place. Finally, I would like to thank my wife, Xiang Wu, for the care, trust and patience. It is my biggest fortune to have her in my life. I would not have been able to finish my dissertation without her support.

ABSTRACT

This work focuses on discovery and development of novel binary halide scintillation materials for radiation detection applications. A complete laboratory for raw materials handling, ampoule preparation, material rapid synthesis screening, single crystal growth, sample cutting, polishing and packaging of hygroscopic halide scintillation materials has been established. Ce^{3+} and Eu^{2+} activated scintillators in three binary systems: Alkali Halide – Rare Earth Halide ($AX–REX_3$), Alkali Halide – Alkaline Earth Halide ($AX–AEX_2$) and Alkaline Earth Halide – Rare Earth Halide ($AEX_2–REX_3$) were systematically studied. Candidates for new scintillation materials in the three systems were selected based on a set of selection rules. A total of 42 Ce^{3+} or Eu^{2+} activated binary halide scintillation material candidates were synthesized and characterized. Among all synthesized candidates, 10 - 15 candidate materials were found to be highly promising in terms of high scintillation light output, fast scintillation decay or desirable emission wavelength.

Three most promising candidates, Cs_3EuI_5, $CsGd_2Cl_7:Ce^{3+}$ and $CsSrI_3:Eu^{2+}$ were selected for single crystal growth and further evaluation. Technologies for single crystal growth of hygroscopic halide scintillation materials were developed. Detailed design of experimental apparatuses was discussed. Single crystals were successfully grown via Bridgman or Vertical Gradient Freeze techniques. Study on optical and scintillation properties was performed. Possibility of using $CsGd_2Cl_7:Ce^{3+}$ as a neutron detector was confirmed.

$CsSrI_3:Eu^{2+}$ shows extraordinary scintillation light output (73,000 ph/MeV), excellent energy resolution (3.9%) and ease for crystal growth. A scaled-up crystal growth was carried out. A bulk crystal of 1" diameter $CsSrI_3:Eu^{2+}$ was successfully grown. Energy level structure and charge carrier traps in $CsSrI_3:Eu^{2+}$ were investigated. Potential of $CsSrI_3:Eu^{2+}$ in various radiation detection applications were evaluated.

PREFACE

One hundred and sixteen years have passed since the German physicist Wilhelm C. Röngten noticed a faint glimmer of fluorescence through the corner of his eye. The unknown knowledge of “X” rays at the time has grown by leaps and bounds into an enormous and profound field of science. The science of radiation and radiation detection has provided a solid ground for technologies which significantly benefit human beings in numerous ways.

Doctors now can examine bone fractures, internal organ diseases and tumors without a single use of the scalpel. Astronomers now can comprehend and predict the future of a celestial body from billions of light years away. Geologists now can pinpoint the exact location, depth, and analyze the chemical composition of an underground oil or gas reservoir by drilling a single tiny hole. Policepersons now can easily identify potential threats without a dangerous personal inspection and even without the notice from the inspected. The technology of radiation detection has grown its branches into every people’s daily life. It is great fortune to be able to contribute a small leaf to the tip of one of the branches.

TABLE OF CONTENTS

LIST OF TABLES

LIST OF FIGURES

CHAPTER 1 INTRODUCTION

Scintillation materials (scintillators) refer to a group of material which is capable of detecting various ionizing radiations and converting them to visible light. Scintillation materials are widely used in radiation detection applications like medical imaging, well-logging and security applications. This dissertation is about discovery and development of new rare earth activated binary halide scintillation materials.

1.1. Historical background and motivation

The past one hundred years have witnessed an intense research and development effort devoted to discovering and improving scintillation materials In the year of 1896, $CaWO_4$ was first discovered after a comprehensive study of thousands of compounds by Edison in order to detect the equally new X-rays which was just discovered by Röngten [1, 2]. However, it was not until Hofstadter who found the exceptionally bright scintillation material NaI:Tl in 1948 [3, 4] that the research on new scintillation materials started taking off. In the year of 1973, another important scintillation material, $Bi_4Ge_3O_{12}$ was discovered by Weber [5]. $Bi_4Ge_3O_{12}$ exhibited extraordinarily high stopping power and was later selected as the scintillation materials for the L3 detector at CERN [6]. Lu_2SiO_5:Ce was introduced in the 1990s as a high resolution and fast scintillation material [7, 8]. In 2001, Siemens/CTI introduced the first Lu_2SiO_5:Ce based high resolution research tomograph (HRRT) for brain imaging [9]. In the same year, van Loef

reported the discovery of another high light output and high resolution scintillation material, $LaBr_3$:Ce [10]. The energy resolution of an inorganic scintillator for the first time was measured below 3%. Originally discovered by Hofstadter in 1968 [11], SrI_2:Eu was brought back into people's attention in 2008 by a large collaboration led by Cherepy among national labs, a university and a company [12]. This scintillation material is also featured with high scintillation light output as well as high energy resolution. Figure 1.1 shows the history of the discovery of major inorganic scintillation materials (year 2000 and before) [13].

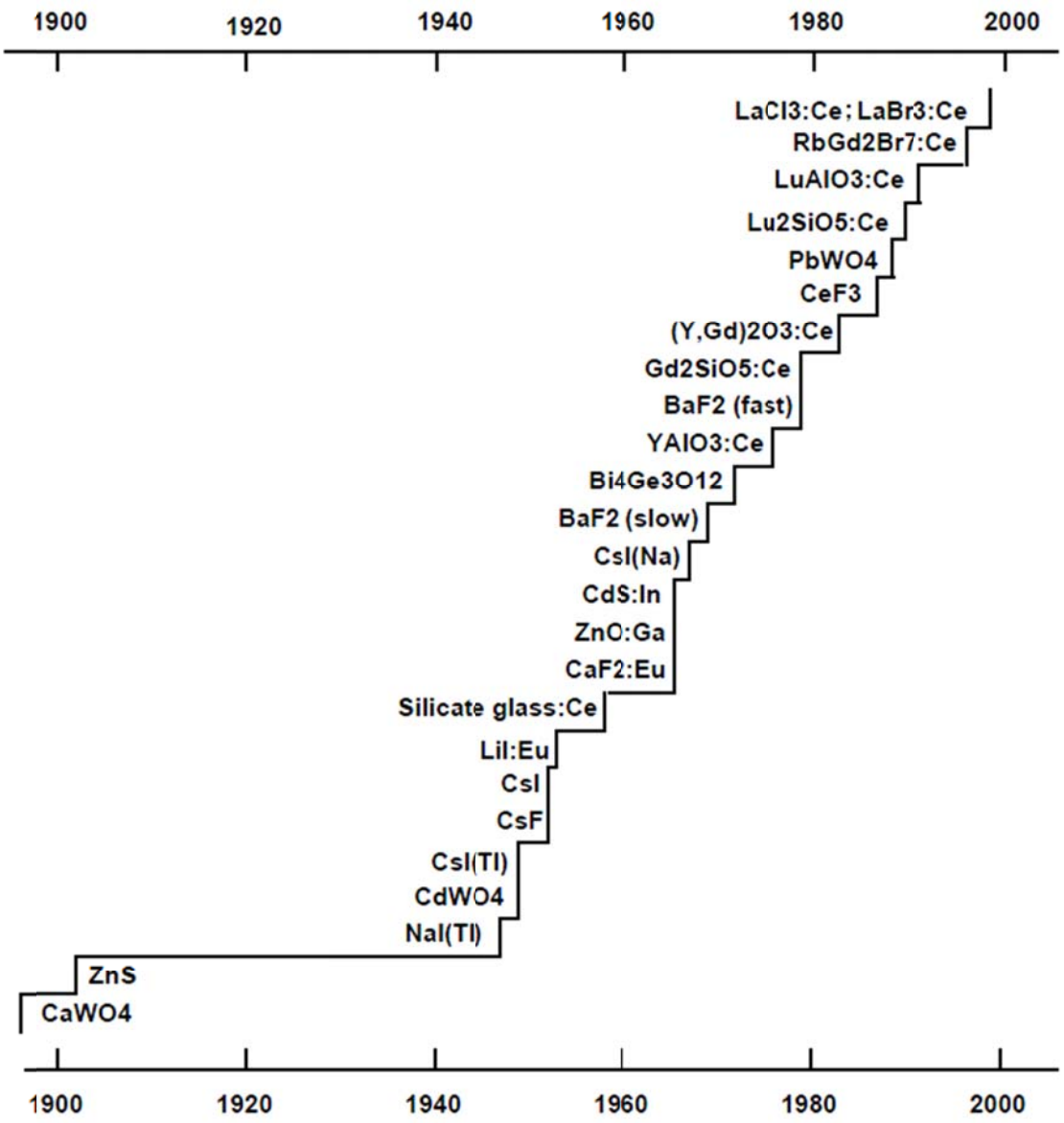

Figure 1.1 History of the discovery of major inorganic scintillation materials

Although numerous scintillation materials with various scintillation characteristics have been discovered in the past decays, the drive for new scintillation materials discovery is still strong. There are several reasons behind that. First of all, no scintillation material is “perfect” in the real world. Whether a scintillation material is “good” solely depends on the specific application for the material. There is always compromise we need to make when selecting a particular scintillation material. For example, there are two types of γ-ray scintillation materials. One is featured with high density, high detection efficiency but with low scintillation light output and low energy resolution, like $Bi_4Ge_3O_{12}$ and $PbWO_4$. This type of scintillators is good for applications where high stopping power is required like calorimeters for high energy physics. Another type is featured with high scintillation light output, good energy resolution, but with low density and low detection efficiency, like NaI:Tl and $LaBr_3$:Ce. This type of scintillator is good for applications where high sensitivity is required like Single Photon Emission Computed Tomography (SPECT), radiation monitors used in security applications and other radiation spectroscopy related applications. There is so far no scintillation material which meets all the requirements. Lu_2SiO_5:Ce is an excellent scintillation material which combines good features like high density, good detection efficiency with high light output and good energy resolution. However, the intrinsic β decay from ^{176}Lu produces a certain level of background radiation and limits the use of Lu_2SiO_5:Ce in low count rate applications where

high sensitivity is required, for example SPECT and radiation monitors used in security applications.

Another reason lies in the requirements of commercialization of scintillation materials. The recently discovered $LaBr_3$:Ce shows excellent scintillation properties. However, the crystal growth of this material is very difficult. $LaBr_3$:Ce was reported to easily cleave during crystal growth [14]. Special seeding techniques have to be applied in single crystal growth to minimize the possibility of cracking and cleaving. The tendency of cleaving limits the size of single crystal which can be grown for this material. This significantly increases the production cost and makes this material less commercially competitive.

The last reason comes from the demand in technologies revolution. A good example for this is a recently brought-up issue on the ^3He shortage. ^3He gas-filled proportional detectors are one of most commonly used neutron detector featured with high neutron sensitivity combined with nearly zero γ sensitivity. Unfortunately, the worldwide shortage of ^3He might result in a complete retirement of this technology, which consequently has become a major motivation for discovery and development of new neutron detection scintillation materials.

As to inorganic scintillation materials, halides and oxide are two most important types of scintillation materials. Halide materials include fluoride, chloride, bromide, iodide and mixed halide compounds. Oxide materials include

single oxides, aluminate, silicate, tungstate, germanate and other similar oxygen-bearing compounds. Comparing to oxide scintillation materials, halide materials usually have much lower melting temperature (usually below 1000℃), which make the synthesis process significantly less expensive. Resistance heated furnace would be enough for synthesis and crystal growth of halide materials, while radio frequency induction heated furnace has to be used in crystal growth of many oxide materials (e.g. the melting point for Lu_2SiO_5 is ~ 2020℃, for $Lu_3Al_5O_{12}$ is ~ 1980℃). Economical crystal growth is always one of the dominant criteria of scintillation materials selection.

The vast majority of attentions in halide scintillation materials discovery have been drawn towards the unitary halide materials in the past few decays. Limited efforts have been made toward the discovery of binary halides. Not until recently, a handful of binary halide materials with promising scintillation properties, namely $K_2LaCl_5:Ce^{3+}$, $RbGd_2Br_7:Ce^{3+}$, $BaBrI:Eu^{2+}$ and $CsBa_2I_5:Eu^{2+}$, were discovered. [15-19].

Due to the great potential lying in the binary halide material system, a systematic screening on a large number of binary halide compounds selected by the requirements of single crystal growth would be highly rewarding. Subsequent development of large scale single crystal growth of the promising candidate materials would demonstrate the possibility of commercialization for the particular material in terms of practical application and future mass production.

1.2. Ionizing radiation

In physics, radiation is a process in which energetic particles or waves travel through a medium or space. Ionizing radiation refers to the types of radiation which have sufficient energy to ionize an atom.

In general, ionizing radiation can be categorized into four types: (1) heavy charged particles, (2) Fast electrons, (3) Electromagnetic radiation, and (4) Neutrons. Heavy charged particles include all energetic ions with mass of one atomic mass unit or greater, such as alpha particle, protons, etc. Fast electrons include beta particles (positive or negative) emitted in nuclear decay, as well as energetic electrons produced by any other process. Electromagnetic radiation includes X-rays emitted in the rearrangement of electron shells of atoms, and γ rays that originate from transitions within the nucleus itself. Neutrons generated in various nuclear processes is often further divided into slow neutron and fast neutron depending on their energy.

1.3. Interaction of radiation with matter

The first step in a scintillation process is the interaction between the ionizing radiation and the scintillation matter. In part, since the scope of this research is scintillation materials for γ and neutron detection, discussion on interaction of radiation with mater would be focused mainly on γ and neutron radiation.

1.3.1. Interaction of gamma-rays with matter

There are many known interactions of γ radiation interacting with matter. However, only three major types of interaction are important for radiation detection measurements. They are (1) photoelectric absorption, (2) Compton scattering, and pair production.

1.3.1.1. Photoelectric absorption

In the photoelectric absorption, a photon transfers all its energy to an electron located in one of the atomic shells. The electron is ejected from the atom by this energy and begins to pass through the surrounding matter. The photoelectron rapidly loses its energy and moves only a relatively short distance from its original location. The photon's energy is, therefore, deposited in the matter close to the site of the photoelectric interaction.

Photoelectric interactions usually occur with electrons that are firmly bound to the atom. This means that the binding energy needs to be relatively high. Photoelectric interactions are most probable when the electron binding energy is only slightly less than the energy of the photon. If the binding energy is more than the energy of the photon, a photoelectric interaction cannot occur. This interaction is possible only when the photon has sufficient energy to overcome the binding energy and remove the electron from the atom.

The photon's energy is divided into two parts by the interaction. A portion of the energy is used to overcome the electron's binding energy and to remove it

from the atom. The remaining energy is transferred to the electron as kinetic energy and is deposited near the interaction site. The energy of the ejected photoelectron is given by Albert Einstein's famous photoelectric equation:

$$E_{e^-} = h\nu - E_b$$

where E_b represents the binding energy of the photoelectron in its original shell. For γ-ray energies of more than a few hundred keV, the photoelectron carries off the majority of the original photo energy.

On the other hand, since the interaction creates a vacancy in one of the electron shells, typically the K or L, an electron moves down to fill in. The drop in energy of the filling electron often produces a characteristic x-ray photon. The energy of the characteristic radiation depends on the binding energy of the electrons involved.

1.3.1.2. Compton scattering

Compton scattering refers to a type of interaction in which only a portion of the energy is absorbed and a photon is produced with reduced energy. In this type of interaction, the incident γ-ray photon is defected through an angle θ with respect to its original direction. In effect, a portion of the incident radiation "bounces off' or is scattered by the material. The probability increases linearly with the number of electron of the target material.

The energy difference between the deflected photon and the original photon is given by:

$$\frac{1}{E'} - \frac{1}{E} = \frac{1}{m_e c^2}(1 - cos\theta)$$

Where *E* is the energy of the incident photon, *E'* is the energy of the scattered photon, m_e is the mass of the electron, *c* is the speed of light, and *θ* is the scattering angle.

As *θ* approaches zero, none of the energy is transferred to the electron. There is a limit that how much energy that can be transferred to the material through a Compton scattering. The maximum amount of energy is transferred when *θ* approaches 180°. In this case,

$$\frac{1}{E'} - \frac{1}{E} = \frac{1}{m_e c^2}\left(1 - \cos(-180)\right)$$

$$(E - E')_{max} = \frac{2E^2}{m_e c^2 + 2E}$$

In pulse height spectra measurement, which will be discussed in the following chapter, this energy $(E\text{-}E')_{max}$ is often referred as the "Compton edge".

1.3.1.3. Pair production

Pair production becomes possible only when the γ-ray energy is more than twice the rest-mass energy of an electron (1.02 MeV). In a pair production interaction, the photon interacts with the nucleus in a manner that its energy is

converted into mater, which is a “pair” of electron and positron. The positron will quickly lose its energy when traveling in the medium and finally annihilate with an electron from the surrounding medium. Two annihilation γ photons of 511 keV are produced as secondary products of the pair production interaction.

1.3.2. Interaction of neutron with matter

Because neutrons are uncharged, they cannot interact with matter through Coulomb force. The neutron can only interact with the nuclei in the material. There are many types of interaction of neutron with a nucleus. They can be divided into two major types: scattering and absorbing. When a neutron is scattered, either elastically or inelastically, the interaction changes the neutron’s speed and direction. The number of protons and neutrons in the nucleus remain the same. The nucleus will recoil in the material and induce a series of radiations. When a neutron is absorbed by a nucleus, the number of protons or neutrons in the nucleus will change, radiations can be emitted and nuclear reactions can be induced.

Neutrons can be divided into two general categories on the basis of their energy. Neutrons with energy higher than 0.5 eV are defined as “fast neutrons”, while neutrons with energy lower than 0.5 eV are defined as “slow neutrons”. In addition, slow neutrons with energy lower than 0.025 eV are often referred as “thermal neutrons”. The interactions of slow neutrons with matter include elastic scattering with the nuclei and neutron-induced nuclear reaction. In the case of

“fast neutrons”, the probability of most neutron-induced reactions potentially useful in detectors decreases. The importance of scattering becomes greater. The secondary radiations from the recoil nuclei also become more important due to the high energy of the incident neutron.

An important concept, which describes the likelihood of a target nucleus interacting with incident neutrons, is conventionally expressed as the neutron cross section. The neutron cross section is defined as the probability of neutrons being absorbed divided by the area atom density. So the cross section has units of area. “*barn”* (10^{-28} m^2) was traditionally used as the unit for neutron cross section.

1.4. Scintillation material

The detection of ionizing radiations can be realized in many ways. Technologies including ionization chambers, proportional counters, Geiger-Mueller counters, scintillator detectors and semiconductor diode detectors are widely used in fields like high energy physics, astronomy, medical imaging, well-logging, and border control. Different applications have their own unique requirements on the technology used for radiation detection. For example, Geiger-Mueller counter, introduced by Geiger and Mueller in 1928 [20] is one of the oldest radiation detector types in existence. Geiger-Mueller counter is perfectly capable for applications like field survey of radioactivity. The counter delivers accurate measurements of the number of ionizing radiation events within a certain period of time. However, this technology is not capable of radiation spectroscopy since it does not provide the information on the energy of each individual radiation.

For applications like radiation detection for medical imaging, well-logging and security screening, inorganic scintillator based detectors are the most commonly used technologies. The performance of an inorganic scintillator based detector is almost entirely based on the physical properties of the particular scintillator.

1.4.1. The ideal scintillation material

A scintillation material converts a fraction of the energy deposited by an incident ionizing radiation into a burst of visible or ultraviolet photons which is

then converted into an electrical signal by a photomultiplier tube or photodiode optically coupled to the material. Figure 1.2 illustrates a basic configuration of a scintillation material based radiation detector.

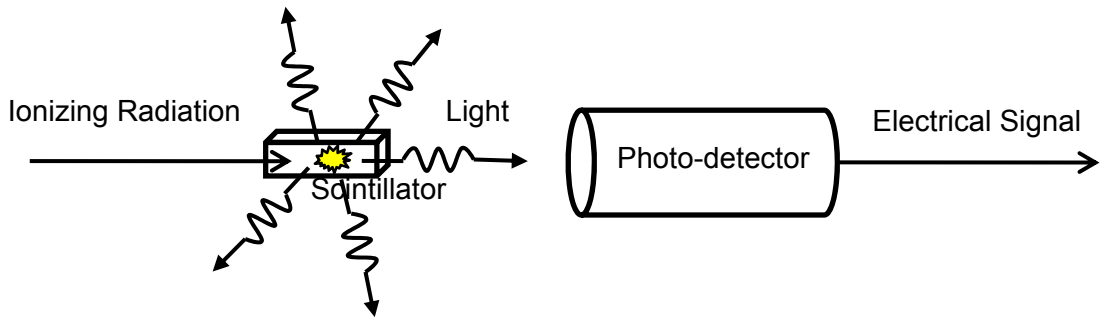

Figure 1.2 Basic configuration of a scintillation material based radiation detector

The ideal scintillation material should possess the following properties:

(1) It should convert the kinetic energy of charged particles into detectable light with high scintillation efficiency.

(2) This conversion should be linear – the light yield should be proportional to deposited energy over as wide a range as possible.

(3) The medium should be transparent to the wavelength of its own emission for good light collection.

(4) The decay time of the induced luminescence should be short so that fast signal pulse can be generated.

(5) The material should be of good optical quality and subject to manufacture in sizes large enough to be of interest as a practical detector.

(6) Its index of refraction should be near that of glass (~1.5) to permit efficient coupling of the scintillation light to a photomultiplier tube or other light sensor.

(7) For activated scintillators, the band gap of the constituent should be in the range of 2.5-5 eV in order to have maximum photon production at a useable wavelength.

(8) Thermal quenching temperature of the scintillation light should be above room temperature.

However, no material simultaneously meets all these criteria. Even widely used scintillators have at least one undesirable property. The choice of a particular scintillator is always a compromise among these and other factors. This also drives the discovery and development of new scintillation materials.

1.4.2. Scintillation process in inorganic scintillators

The scintillation process in inorganic scintillation materials usually consists of many complex physical steps. In general, the scintillation process can be described by three steps. First step is the interaction between an incident ionizing radiation and the scintillation material. Total or partial energy of the incident ionizing radiation may be deposited in the scintillation material depends on the nature of the interaction. Electron-hole pairs are created in the scintillation material as a result of energy deposition. Second step is thermal relaxation of the electron-hole pairs. After numerous interactions with the host lattice, the initial

electron-hole pairs might either transfer their energy to the crystal lattice in form of phonons or create secondary electron-hole pairs. At the end of thermal relaxation, energy of delocalized electrons would be equal to the energy of the bottom of the conduction band and energy of delocalized holes would be equal to the energy of the top of the valence band. The final step is recombination. Electrons or holes recombine at either radiatve centers where light is produced, or at non-radiative centers with no light emission, depending on the specific scintillation mechanism. There are many types of scintillation mechanism exist in inorganic scintillators [21, 22], including:

(1) Luminescent ion promptly captures electron, hole diffuses to form an excited state (CsI:Tl)
(2) Luminescent ion promptly capture hole then an electron to form an excited state (Lu_2SiO_5:Ce)
(3) Hole and electron combine to form a self-trapped exciton that transfers its energy to a luminescent ion ($LaBr_3$:Ce)
(4) Hole and electron combine to form a self-trapped exciton that radiates (NaI, CsI, BaF_2)
(5) Self-activated: luminescent ion is a major constituent of the crystal ($Bi_4Ge_3O_{12}$, $Bi_4Si_3O_{12}$, $CeBr_3$)
(6) Bound exciton: electron plus a hole bound to an isoelectronic impurity (CdS:Te)

(7) Charge exchange: ionization electron on the cation combines with a hole on the anion ($CaWO_4$, $PbWO_4$)

(8) Core-valence: valence electron drops into hole in upper core band (BaF_2)

(9) Electron-hole recombination in semiconductors

Based on various scintillation processes, inorganic scintillation materials can be generally divided into two categories: intrinsic scintillation materials and activated scintillation materials. An intrinsic scintillation material refer to a scintillation material emits light from the constituent or a constituent related defect. Scintillation process 4-9 can be categorized as intrinsic scintillations. Activated scintillation material emits light from an introduced luminescence center, usually a rare earth dopant. Scintillation process 1-3 can be categorized as activated scintillations. The scintillation efficiency is determined by the intrinsic efficiency of the luminescence center and the ionization and energy transfer process in the host material. Figure 1.3 shows a schematic diagram of various scintillation processes in inorganic scintillation materials.

Whether efficient intrinsic scintillations are possible in a certain scintillation materials is usually difficult to predict. In contrast, for activated scintillation materials, the host materials are not required to be intrinsically luminescent. Many optically inert materials can be used as host materials for activated scintillation materials. This opens up many possibilities for inorganic scintillation discovery.

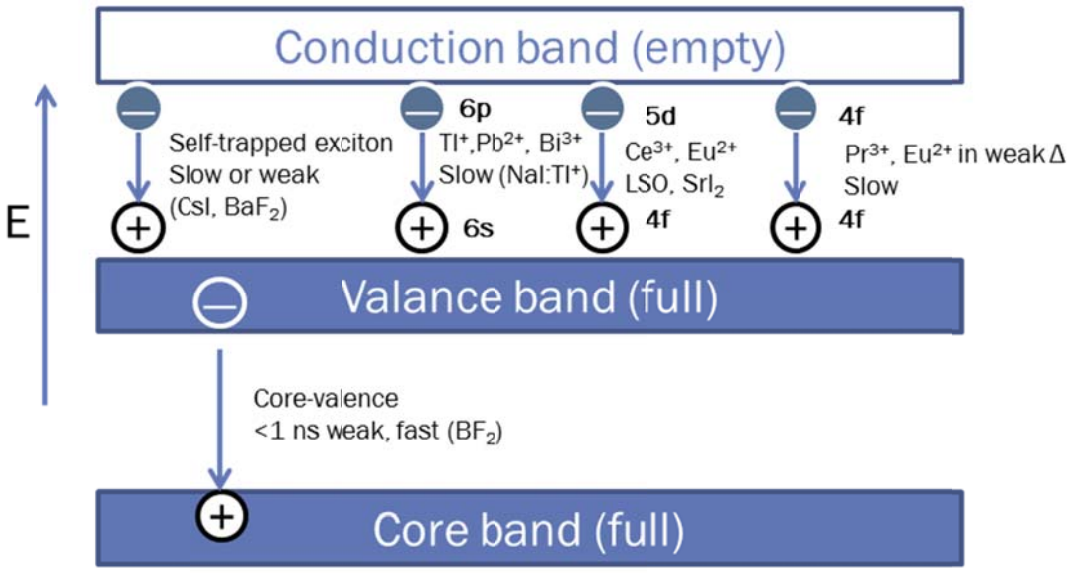

Figure 1.3 Scintillation processes in inorganic crystals; scintillation mechanisms showing in the figure are (1) defect-related self-trapped exciton emission in CsI and BaF_2; (2) 6p-6s emission from the luminescence ions: Tl^+, Pb^{2+} and Bi^{3+}; (3) parity-allowed 5d-4f emission from Ce^{3+} and Eu^{2+}; (4) emission of 4f-4f forbidden transitions from Pr^{3+} and Eu^{2+} in weak crystal field; (5) fast core-valence emission from BaF_2

1.4.3. Activated scintillation material

1.4.3.1. Activator overview

As discussed, light from activated scintillation materials is emitted by the introduced luminescent ions in the host material matrix. Many ions can be introduced to produce optical emission.

Tl^+-like ions (e.g. Sn^{2+},Sb^{3+}, Tl^+, Pb^{2+}, and Bi^{3+}) are often incorporated in alkali halides or oxygen-dominated host lattice to produce luminescence. The luminescence of these ions is from a spin-forbidden transition ($^3P_1 \rightarrow {}^1S_0$). As a result, the luminescence is usually slow and of the order of microseconds [23]. In addition these types of activators utilize the energy level transitions at the outermost shell of the ion, which is very sensitive to the crystal field of the host lattice. The luminescence properties of Tl^+-like ions activated material are highly dependent on the physical properties of the host material, which makes the discovery of good Tl^+-like ions activated scintillation materials more difficult.

Transition metal ions (e.g. Cr^{3+}, Mn^{4+}, Mn^{2+}, Fe^{3+}) are also used as luminescent activators in various host lattices. Transition metal ions activated materials are usually considered as phosphors due to their long decay time (millisecond). The emission wavelength from these materials is also in the long wavelength region and is unfavorable for conventional photo sensors used in radiation detector. Similar to the Tl^+-like ions, transition metal ions emit from their

3d levels which are also outer orbit and heavily affected by the environmental or crystal field.

Rare earth ions possess unique characteristics comparing to other types of luminescent activators. The luminescence transitions in rare earth ions usually take place either between 5d-4f or within the 4f level. In strong contrast to the above two types of ions, the 4f electrons in rare earth ions are well shielded by the outer $5s^2$ and $5p^6$ electrons. The 4f levels are not affected much by the environment.

1.4.3.2. Ce^{3+} and Eu^{2+} luminescence centers

This research focuses on two specific rare earth activators: Ce^{3+} and Eu^{2+}. These two ions are favorable as activators for scintillation materials because:

(1) Both Ce^{3+} and Eu^{2+} utilize parity and spin allowed 5d-4f transition, which results in a high luminescence efficiency.

(2) The 5d-4f emission wavelengths of both Ce^{3+} and Eu^{2+} are in the sensitive range of conventional photo sensors (photomultiplier tubes and photodiodes)

It is well known that the 4f ground state of Ce^{3+} is split into two energy levels, $^2F_{5/2}$ and $^2F_{7/2}$, due to spin–orbit coupling. Typical Ce^{3+} 4f-5d emission shows a double-peak structure due to the two terminating levels of the 4f configuration of Ce^{3+}. The decay time of the Ce^{3+} emission is 10^{-7} to 10^{-8} s. the shortest in observed lanthanide ions.

For Eu^{2+}, 4f-4f transition (^6P_j – $^8S_{7/2}$) is possible in weak crystal field. Emission spectra from 4f-4f transition are usually featured with a group of sharp peaks. This is because the 4f levels of Eu^{2+} is well shield and energy level splitting is minimized. The 5d level splits in medium to strong crystal field and the bottom of the 5d level moves lower than the ^6P_j levels in 4f. Thus the 5d - 4f transition (5d - $^8S_{7/2}$) becomes possible. Typical Eu2+ 5d-4f emission shows a single peak which represents the transition from the bottom of the 5d level to the $^8S_{7/2}$ level in 4f. The lifetime of the Eu^{2+} luminescence is 10^{-5}-10^{-6}s.

Figure 1.4 shows typical emission spectra pf Ce^{3+} and Eu^{2+} activated scintillation materials. Figure 1.5 is the well-known “Dieke diagram” for energy levels of trivalent lanthanide ions [24]. Gd^{3+} has the identical electronic configuration as Eu^{2+}.

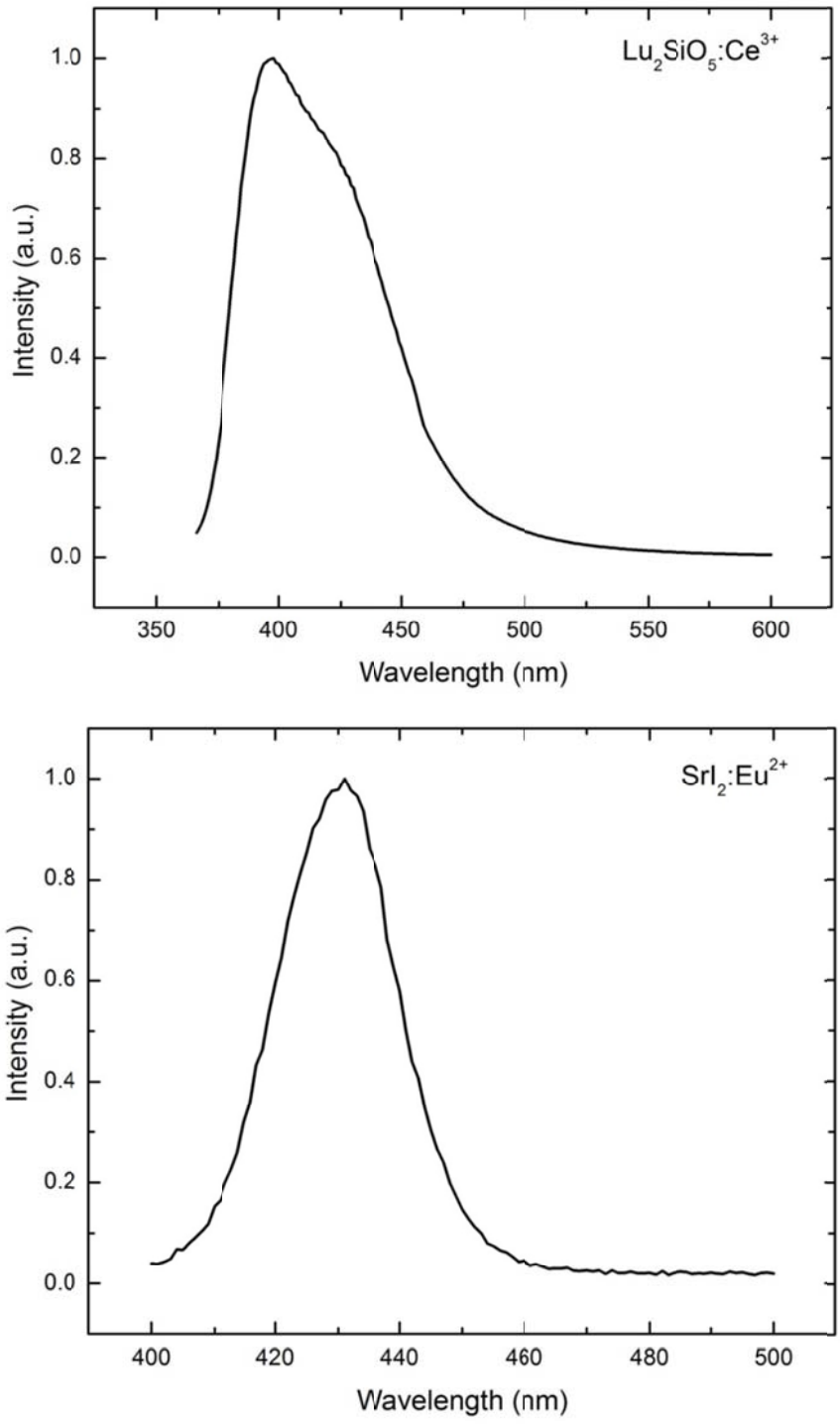

Figure 1.4 UV excited emission spectra for Ce^{3+} activated Lu_2SiO_5 (characteristic double-peak structure) and Eu^{2+} activated SrI_2 (single peak)

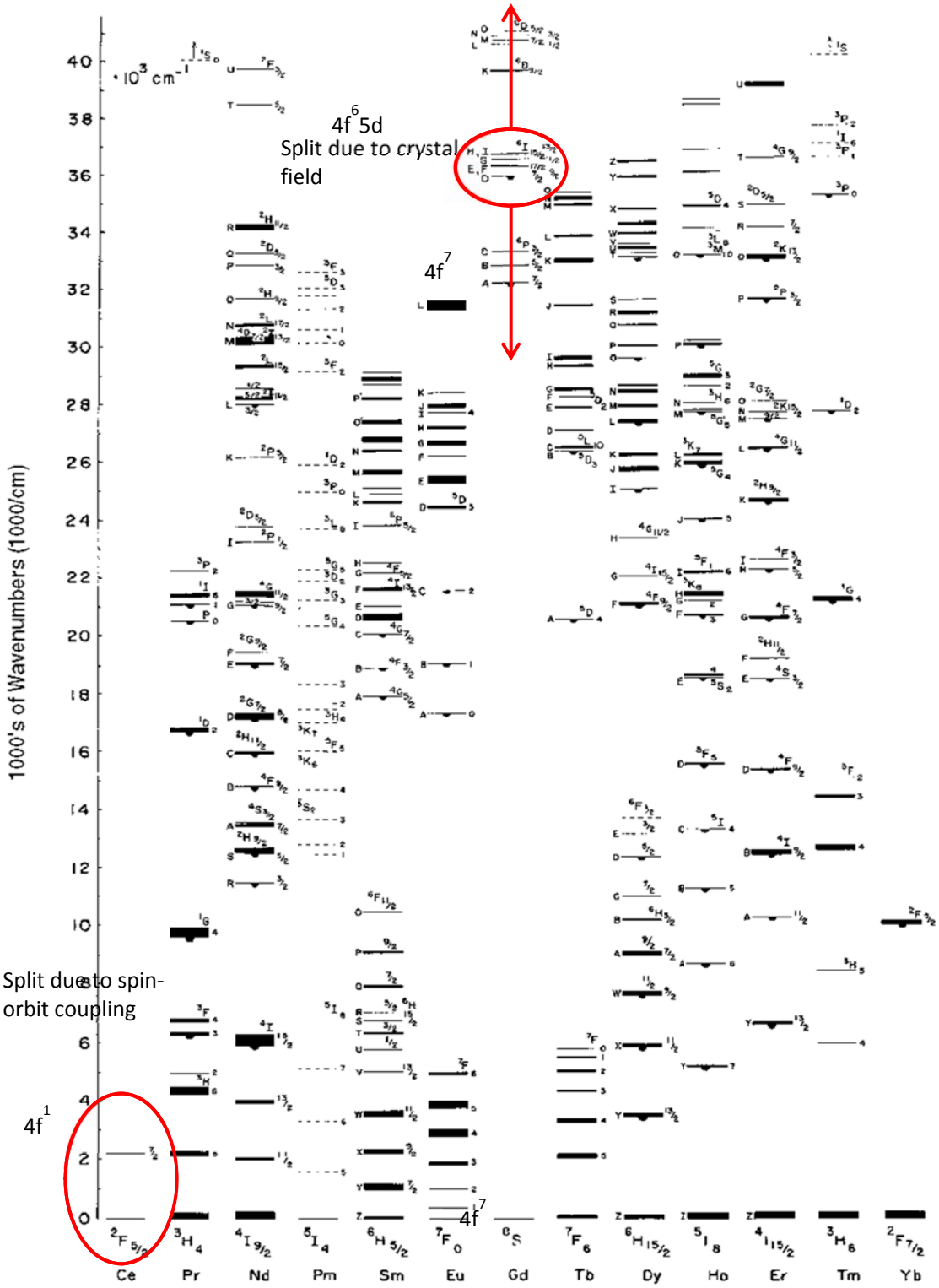

Figure 1.5 Energy levels of trivalent lanthanide ions

1.4.3.3. Configurational coordinate diagram

The energy level structure and optical properties of a rare earth luminescence center can be more accurately described by the Configurational Coordinate Diagram. The Configurational coordinate diagram explains optical properties of a luminescence center based on potential curves (parabolas), each of which represents the total energy of the luminescence center in its ground or excited state as a function of the configuration coordinate. The configurational coordinate is a simplified description of the vibrational modes of the lattice. Figure 1.6 shows a typical example for a 5d-4f configurational coordinate diagram. The 5d level is the excited state and 4f level is the ground state. Because (1) the equilibrium position for the excited state is slightly different from that of the ground state due to different environment, and (2) transitions always initiate from the bottom of a state, the excitation energy will be different from the emission energy. The difference between the excitation and emission wavelengths is defined as the Stokes Shift.

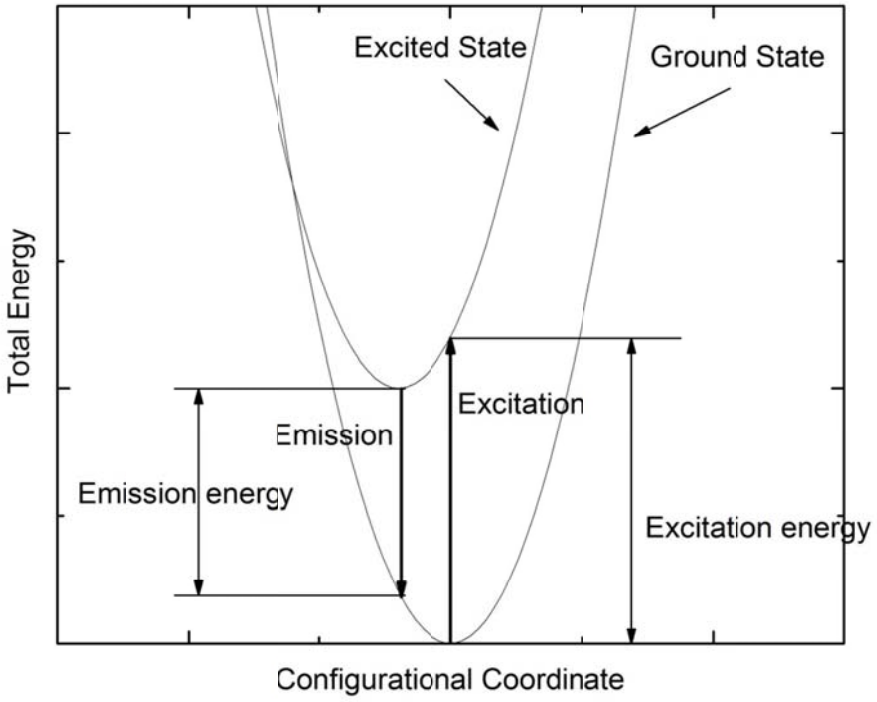

Figure 1.6 A schematic illustration of a typical 5d-4f configurational coordinate diagram

1.4.3.4. Host material

Selection criteria of host material for Ce^{3+} or Eu^{2+} activated scintillators include high density, high effective atomic number and a relatively small gap between the valence and conduction band. The host material must also be able to incorporate Ce^{3+} and Eu^{2+} ions in a controlled way.

One of the most important concerns is the band gap. As is discussed in 1.4.2., electron–hole pairs are created by the incident ionizing radiation at the beginning of the scintillation process. A certain percentage of charge carriers will be transferred to activator ions and produce light, depending on the energy transfer efficiency. The number of electron–hole pairs a scintillation material can produce under certain amount of energy deposition is directly related to its scintillation light output (number of photons the scintillation material produces under certain amount of energy deposition). The more electron–hole pair a scintillation material can produce, the "brighter" the material is. If one assumes that all charge carriers will be transferred to activator ions and that the intrinsic luminescence quantum efficiency of the activator ion is unity, the theoretical limit of scintillation light output will be fully determined by the number of electron–hole pairs $n_{e\text{-}h}$ created in the ionization track. This can be expressed as

$$n_{e-h} = \frac{E_{radiation}}{\beta E_{gap}}$$

The fundamental limit on the light output is determined by the band gap E_g of the host material. The efficiency factor β is found to be close to 2.5 [25].

On the other hand, the host band gap must contain both ground and excited levels of the activator ions. The energy between the 4f levels (ground state) and bottom of 5d levels (excited state) of a Ce^{3+} ion is typically 2 ~ 5 eV for halide and oxide materials [25, 26]. Luminescence will be quenched if there is complete overlap between the ground level of the activator and the valence band of the host, or overlap between the excited level of the activator and the conduction band of the host. One example is $Lu_2O_3:Ce^{3+}$. Lu_2O_3 has an extremely high density (9.4 g/cm^3) and cubic structure which is desirable for ceramic processing. Unfortunately, the 5d levels of trivalent cerium in Lu_2O_3 overlap those of the conduction band, which results in a complete quenching of Ce^{3+} 5d-4f luminescence [27].

Halide materials, especially chlorides, bromides and iodides, are found to have appropriate bang gap. Figure 1.7 shows the light output of scintillation materials and phosphor materials. The widths of band gap of various host materials are shown at the top of the figure. Within sulfides, iodides, bromides and chlorides maximal efficient scintillator have been found. Oxide and fluoride compounds seem to produce less light [25]. Chlorides, bromides and iodides are good host materials for activated scintillators.

Binary metal halide refers to a compound with the general formula M_1M_2X, where M_1 and M_2 stand for two metallic elements and X stands for halides. As discussed in 1.1., limited studies have been down in using binary metal halides as the host materials. One unique advantage for the binary metal halide is the binary metal halide provides the possibility of incorporating large neutron cross section atoms (Li, B and Gd) into the constituent but still maintain a relatively high effective atomic number. So the scintillation material can work simultaneously as neutron and gamma detector with proper pulse shape discrimination, like $RbGd_2Br_7$ [16, 19].

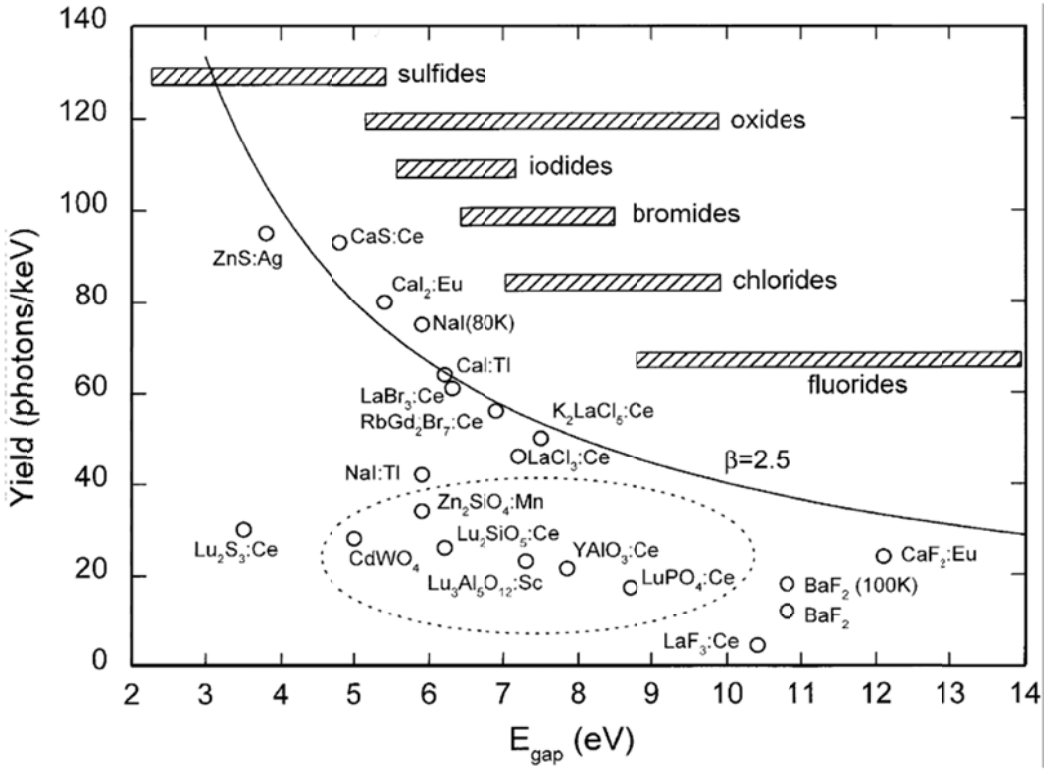

Figure 1.7 Light output of scintillation materials and cathode ray tube phosphors

1.5. Single crystal growth

Crystal growth techniques can be generally divided into four categories: (1) crystal growth from the solid, (2) crystal growth from the vapor, (3) crystal growth from solution, (4) crystal growth from the melt. Solid growth is based on atomic diffusion in solid at elevated temperature. One old example is Zone Heating technique, which was used to produce single crystal tungsten filament [28]. Vapor growth includes many widely used techniques like Chemical Vapor Deposition (CVD) and Molecular Beam Epitaxy (MBE). These techniques are capable of crystal growth in thin film form with accurately controlled doping, composition and quality on available substrate material. Solution crystal growth has its own unique advantages, such as solution growth is able to grow a compound at a temperature below its melting point. Liquid Phase Epitaxy (LPE) is commonly used in semiconductor industry for thin film crystal growth. However, solution growth is usually very slow. It is at least an order of magnitude slow than melt growth.

1.5.1. Requirements for melt growth and phase diagram

Melt growth is the best and most efficient method for growing large single crystals of high perfection. It is widely used in the electronics, optics, and synthetic gemstone industries. As to scintillation materials, melt growth is also the dominant crystal growth method used to produce single crystal scintillation materials such as $Lu_2SiO_5:Ce^{3+}$, $Bi_3Ge_4O_{12}$, $LaBr_3:Ce^{3+}$, $NaI:Tl^+$ for various applications.

Melt growth normally requires that the material melt congruently, which means the material does not decompose below or near its melting point. In addition, it would be favorable if the particular material does not have solid-to-solid phase transition at a temperature below its melting point in order to achieve the best optical quality. Solid-to-solid phase transition at low temperature may initiate cracks in the crystal due to the lattice mismatch between the old and new phases. These two requirements are essential when selecting candidate materials for melt crystal growth. The information can be obtained from the phase diagram of the particular material system. Figure 1.8 illustrates the EuI_2 - KI phase diagram [29]. The composition KEu_2I_5 melts congruently and it does not appear to have low temperature solid-to-solid phase transition. This composition is suitable for crystal growth from the melt.

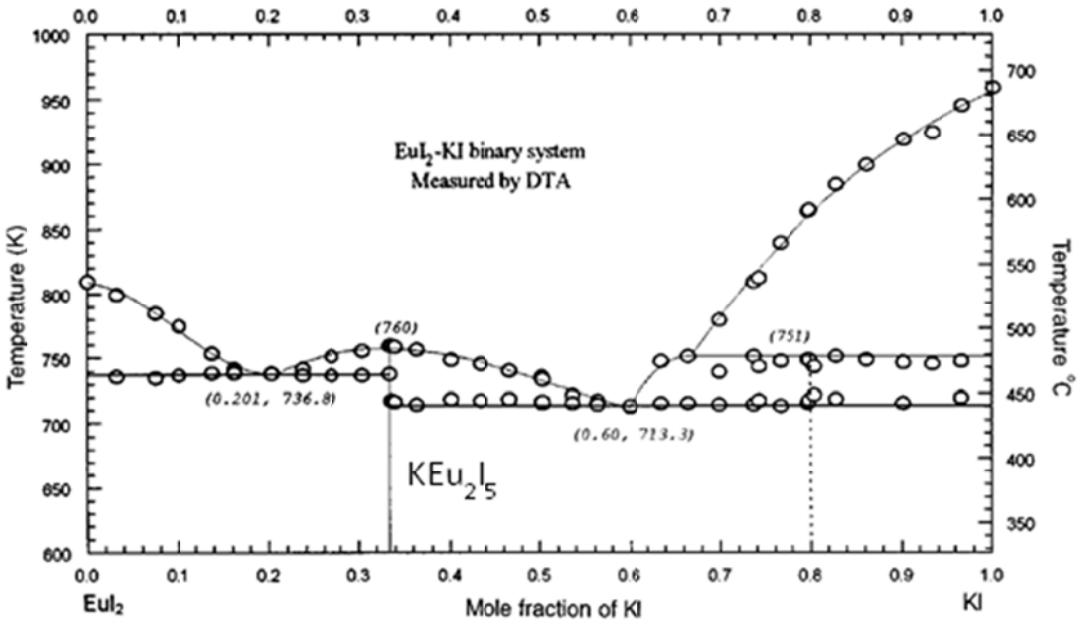

Figure 1.8 phase diagram of EuI_2 – KI binary system

1.5.2. Melt growth techniques

Crystal pulling and directional freeze are two types of important melt growth techniques. Developed in 1918 [30], Czochralski crystal growth is still one of the most widely used bulk crystal growth techniques today. Czochralski technique is capable of growing bulk single crystal of large diameter. Semiconductor industries are known for growth of single crystal silicon boule of a diameter up to 12". Commercially available scintillation crystals such as Lu_2SiO_5:Ce, $Lu_3Al_5O_{12}$:Pr, and Gd_2SiO_5:Ce are usually produced by Czochralski technique. Micro-pulling-down (μ-PD) method is an important crystal pulling technique, too. Micro-pulling-down is based on continuous transport of the molten material through micro-channel(s) made in a crucible bottom. Continuous solidification of the melt is progress on a liquid-solid interface positioned under that crucible. Micro-pulling-down method is designed for single crystal growth of crystal rods, bands and fibers. One advantage for this method is that micro-pulling-down is able to grow single crystals within a short period of time. This is suitable for rapid material exploration in research laboratories.

Another important category of crystal growth technique is directional freeze. Directional freeze can be divided into three categories based on the way of controlling the freezing interface, moving ampoule, moving gradient and cooled seed method. The most common technique for directional freeze by moving ampoule is Bridgman-Stockbarger technique [31, 32]. Moving gradient method is used in gradient freeze crystal growth by Electro-Dynamic Gradient furnace [33] .

Cooled seed method is important for crystal growth of extra-large size single crystal. Two well-known cooled seed methods are Kyropoulos method [34] and Heater Exchanger Method (HEM) [35]. Both are used in industrial crystal growth of large diameter sapphire crystals [36, 37].

1.5.2.1. Bridgman-Stockbarger and Gradient Freeze

Bridgman-Stockbarger method usually utilizes a two-zone furnace, either in vertical or horizontal position. The top zone is set at a temperature which is higher than the melting point of the material to be grown. The bottom zone is set at a temperature which is lower than the melting point. To start with, starting materials loaded in crystal growth ampoule (or crucible) is heated above its melting point in the hot zone. The ampoule slowly travels through the thermal gradient and enters the cold zone. Usually a seed crystal is located at the end of the ampoule or crucible. Along the progress of ampoule travelling, a single crystal of the same crystallographic orientation as the seed material is grown on the seed and is progressively formed along the length of the ampoule. A schematic diagram of a Bridgman-Stockbarger crystal growth furnace is shown in figure 1.9a. Because crystal growth ampoule can be designed as a sealed container, Bridgman-Stockbarger method is very useful in crystal growth of materials which are atmosphere sensitive. For example, Bridgman-Stockbarger method is widely used to grow hygroscopic halide materials (e.g. $LaBr_3$:Ce [38]) and semiconductor materials (GaAs [39]) which are easily oxidized.

Gradient Freeze crystal growth is usually carried out in a special type of furnace named “Electro-Dynamic Gradient (EDG) furnace”. Commercially available since 1978, the EDG furnace was designed with narrow heating zones which are used to shape the axial temperature gradient along the axis of the furnace [40]. In contrast to typical Bridgman-Stockbarger method, the temperature profile in the furnace core is moved electronically, rather than physically. This has several advantages over the traditional Bridgman-Stockbarger. First, there is no moving part in the entire crystal growth system. Both ends of the furnace can be completely sealed. This prevents any extraneous thermal current. Second, the thermal profile inside the furnace can be precisely controlled and measured by the furnace. This is beneficial for growth of some crystals, for example, crystals with supercooling during solidification. Thermal gradient near the solid-liquid interface and the cooling rate can be more precisely controlled. A detailed discuss about Vertical Gradient Freeze crystal growth carried out in a Mellen Sunfire 24-zone EDG furnace will be provided in the next chapter. A schematic diagram of an EDG crystal growth furnace is shown in Figure 1.9b.

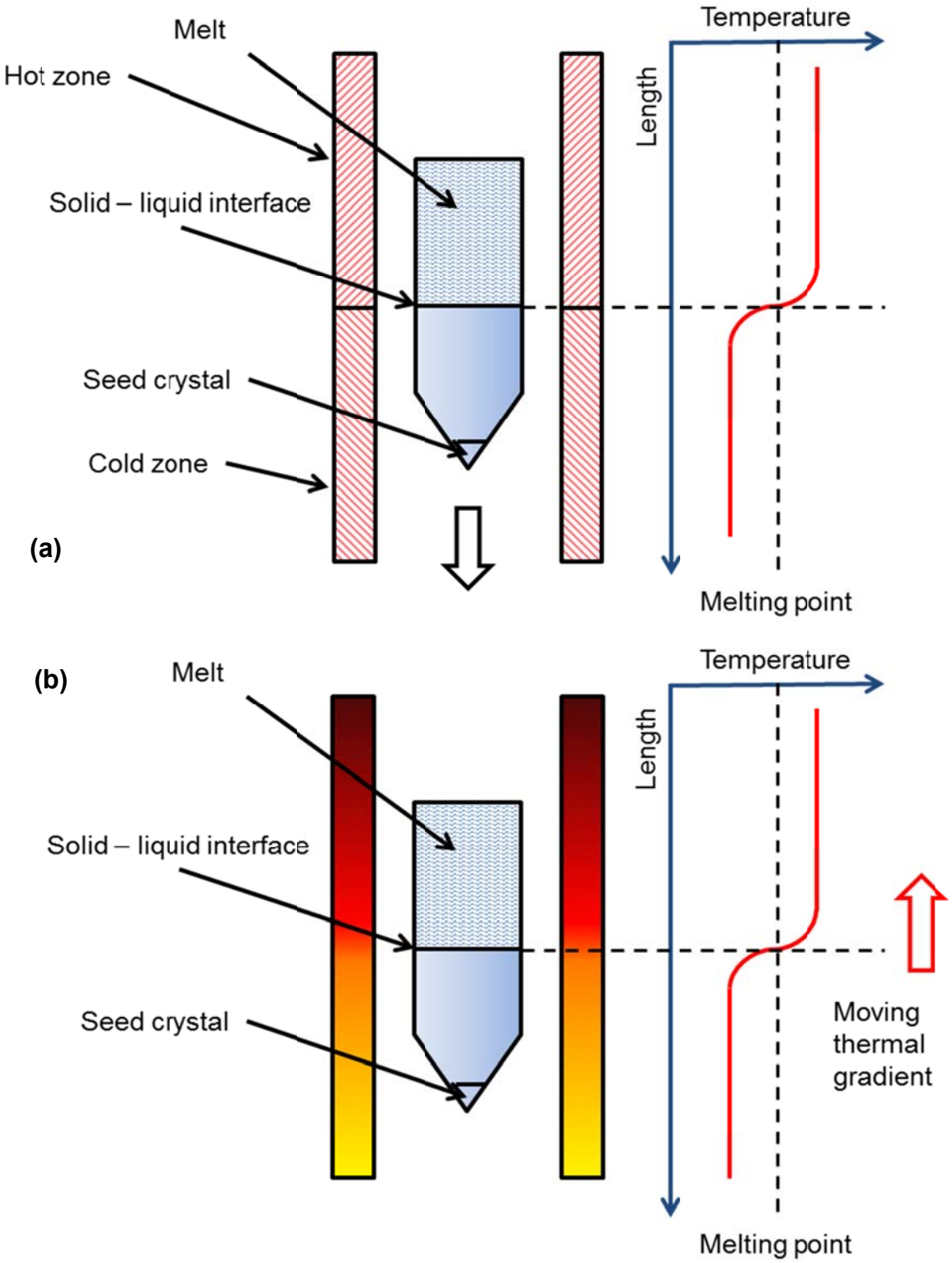

Figure 1.9 Schematic diagrams of (a) a Bridgman-Stockbarger crystal growth furnace and (b) an Electro-Dynamic Gradient (EDG) crystal growth furnace

CHAPTER II EXPERIMENTAL TECHNIQUES

2.1. Synthesis

2.1.1. Overview

The design of experimental apparatuses for synthesis of halide scintillators is based on the properties of the target materials and the requirements to grow them in single crystal form. First and the most important concern is that most halides materials are hygroscopic. This means they tend to attract and hold water molecules from the surrounding environment. The process of moisture-absorbing permanently damages the crystal quality and is irreversible. Many well-known halide scintillators (e.g. NaI:Tl and $LaBr_3$:Ce) are reported to be strongly hygroscopic [1]. Another concern is that most halides are prone to oxidization at elevated temperature. This requires that the crystal must be grown in vacuum or inert atmosphere. Special encapsulation techniques have to be developed and applied in order to synthesize and protect the halide crystals.

The goal of this research includes both new scintillators discovery and development of promising candidates. Two sets of experimental procedures were developed. Specialized apparatuses were designed and fabricated for both rapid melt synthesis and bulk single crystal growth of halide materials.

2.1.2. Ampoule preparation system

Custom-designed vacuum sealed quartz ampoules were used to protect halide materials from moisture and oxygen during synthesis. An ampoule preparation system was designed to prepare ampoules for both rapid melt synthesis and single crystal growth. The design requirements were:

1) The system must be capable of producing adequate vacuum inside the melt synthesis and crystal growth ampoules

2) The system must be able to heat the materials under vacuum for an extended period of time in order to remove all residual moisture

3) The system must be resistive to corrosion

Figure 2.1 shows a photo and a schematic diagram for the ampoule preparation system. The system consists of two main parts: a vacuum manifold and a vertical clamshell furnace. The vacuum manifold utilizes a two-stage pumping system, a roughing pump (Edwards RV 12, not shown) and a turbomolecular pump (Adixen ATP400), to evacuate ampoules to a vacuum lower than 10^{-6} mbar. Our previous experiments showed that a vacuum manifold which was capable of producing 10^{-6} mBar vacuum would be advantageous in preparation of ampoules for hygroscopic materials. A foreline trap (Kurt J. Lesker metal wool foreline trap) was installed on the inlet of the roughing pump to remove any oil particles released by the roughing pump. Turbomolecular pump was selected as the second stage high vacuum pump because it would not

produce oil mist and introduce any foreign contamination into the system. The vacuum manifold was built by stainless steel parts with Viton O-rings for better corrosion resistivity. An Edwards Pirani vacuum gauge and an Edwards Penning vacuum gauge were used to measure both low and high level vacuum. The vertical clamshell furnace is capable of heating the ampoule to a temperature as high as 1000 ℃. The clamshell furnace is retractable so that ampoule can be sealed under continuous evacuation.

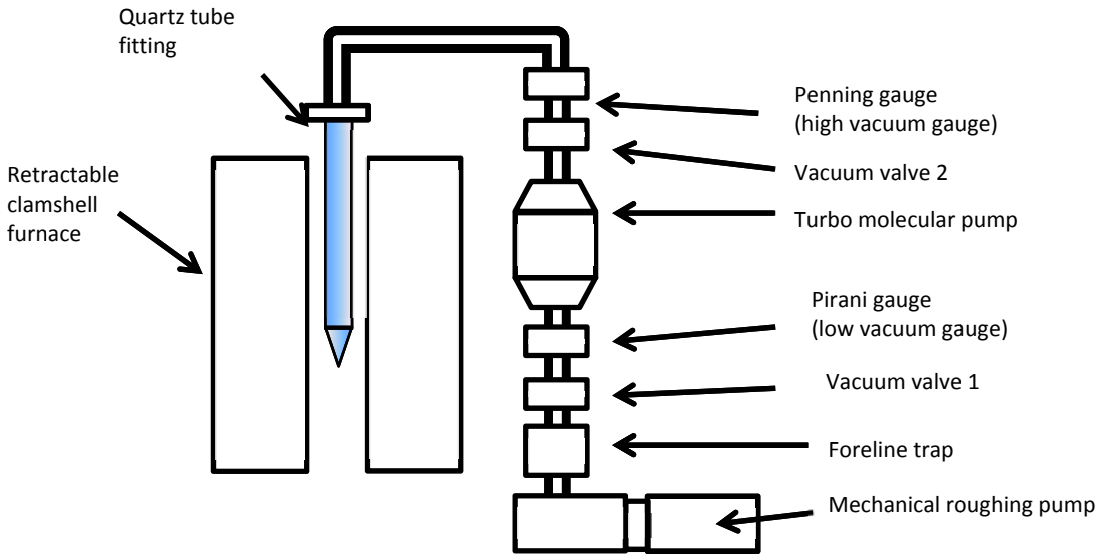

Figure 2.1 The vacuum ampoule preparation system

2.1.3. Rapid screening

To evaluate the potential of a candidate material as a single crystal scintillator, melt synthesis was used for rapid screening of candidate binary halide materials. A simple quartz ampoule design was chosen for materials melt synthesis. All synthesis ampoules were hand-made from quartz tubes to keep the cost down. The synthesis ampoule was approximately 25 mm long with 8 mm diameter. One end of the ampoule was sealed by a hydrogen torch before loading the materials. The open end was sealed directly after required vacuum was achieved. No additional tube was used.

Each ampoule was rinsed with diluted hydrofluoric acid (4.80 – 5.00%) and de-ionized water before use. Small amount of stoichiometric mixture (typically 5 g) of 99.99% pure raw materials from Sigma Aldrich was prepared inside a N_2 purged glove box (MBraun Unilab glovebox). Both oxygen and moisture concentrations inside the glovebox were lower than 1 ppm since most raw materials were hygroscopic (e.g. SrI_2, $CeBr_3$, $CeCl_3$, etc.). Starting materials were purchased in beads form (powder if beads were not available) for better flow property. Due to the dry environment inside the glovebox, starting materials (beads or powder) were highly charged and difficult to handle. Only metal or anti-static plastic apparatuses were used to overcome the static charge problem. The prepared stoichiometric mixture was then loaded into the melt synthesis ampoule. The melt synthesis ampoule was temporarily sealed with a Parafilm M sealing film until it was transferred out of the glove box and connected to the vacuum

system. The melt synthesis ampoules were evacuated and heated at 300 ℃ for at least 12 hours before they were sealed by a H_2-O_2 torch. This was to remove any residual moisture in the raw materials. In addition to its detrimental effect on material properties, residual moisture must be removed to avoid any pressure buildup in the ampoule. The vacuum inside the ampoule was evacuated to at least 10^{-6} mbar at the time of sealing.

After the melt synthesis ampoules were sealed, they were hand-shaken for 10 ~ 15 minutes to ensure homogeneous mixing. Then ampoules were then transferred to a box furnace (Lindberg 1500 ^{o}C box furnace) for melt synthesis. Setpoint of the furnace was usually chosen at ~ 50 ^{o}C above the melting point of the compound based on the available phase diagram. Often the exact melting point of the compound was unknown due to lack of information. In this case, ~50 ^{o}C above the highest melting point of all starting materials was selected as the temperature for melt synthesis. Melt synthesis ampoules were kept at the selected temperature for 12 hours before cooling to ensure the completion of reaction.

Since no single crystal growth technique was applied, the material was synthesized in the form of a polycrystalline ingot. The polycrystalline ingot was later evaluated in terms of scintillation light output, scintillation decay time, UV and X-ray excited luminescence and hygroscopicity. Figure 2.2 illustrates four synthesized candidate materials under nature light and the excitation of 255 nm

UV. Candidates with promising optical and scintillation properties were selected and crystal growth of these materials was pursued.

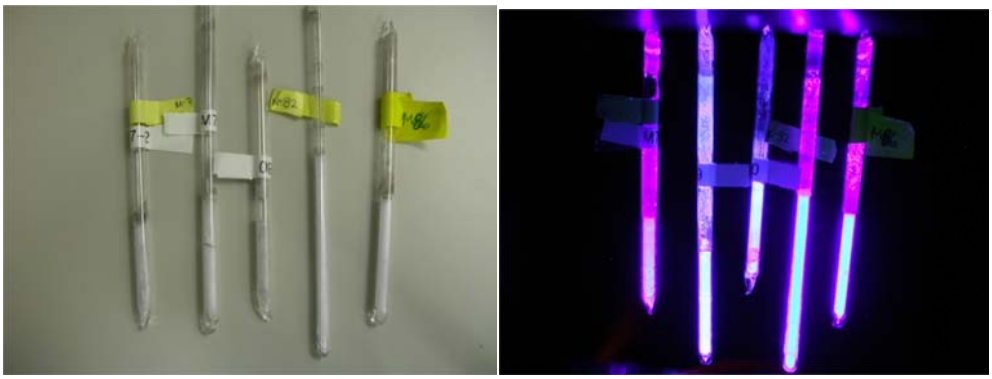

Figure 2.2 Melt synthesized candidate materials under natural light and the excitation of 255 nm UV

2.1.4. Crystal growth

2.1.4.1. Overview

Single crystal growth was performed on promising material candidates which were selected by rapid synthesis screening. Vacuum sealed ampoules loaded with stoichiometric mixture of starting materials and dopants were prepared prior to crystal growth. An Electro-Dynamic Gradient (EDG) furnace (Mellen Sunfire 24-zone Electro-Dynamic Gradient furnace) was used for crystal growth. Both vertical gradient freeze and Bridgman crystal growth techniques were applied for best single crystal yields.

2.1.4.2. Design of crystal growth ampoule

The design of crystal growth ampoule has been modified multiple times to deal with various issues encountered in the process of development. Some of the typical issues include refractory contaminations in the raw material and material decomposition during sealing. Pictures of crystal growth ampoules with these issues are show in Figure 2.3.

Figure 2.3a shows a layer of contaminated materials at the top of a grown single crystal. This black contamination is considered to be carbon particles from the raw materials. According to discussions with our raw materials provider Sigma Aldrich, carbon particles were possibly introduced into the raw materials during the manufacturer's purification process. Since the carbon particles have lower density than the halide melt, they gather near the surface of the melt. Due to the existence of this contamination, about 5 mm thick layer of crystal material has to be discarded. Carbon particles can potentially initiate cracks during cooling down, for their thermal expansion coefficient is different from the halide crystal.

Another issue is materials decomposition during ampoule sealing. Figure 2.3b shows photos from a previous design of crystal growth ampoule of which the seal is made at a thin tube ("neck") above the crystal growth volume. It is highly possible that the "neck" part of the ampoule is contaminated by a small amount of raw materials when they are loaded into the ampoule. If seal is made near the contaminated area, halide materials may decompose under the heat from the H_2-

O_2 flame (around 2000 ^oC). In Figure 2.3b, iodide materials decomposed under the heat and released iodine gas which condensated at the bottom part of the ampoule (showing dark brown). Figure 2.3c shows the iodine diffused through and colorized the entire crystal after re-melt. Small amount of material decomposition is highly detrimental to the optical transparency of the crystal.

Crystal growth ampoules were designed to address the above-mentioned issues during development.

Figure 2.3 Materials were contaminated by (a) refractory contaminations from raw materials (b) iodine released from material decomposed during ampoule sealing; (c) iodine contaminations diffused throughout the crystal after melt

The crystal growth ampoule assembly consists of three major parts: (1) crystal growth volume and outer tube; (2) melt filtration tube; (3) sealing tube. These three parts work together as a complete crystal growth ampoule. The bottom part of (1) is the crystal growth volume, in which crystal growth takes place. A 2 mm outer diameter and 1 mm inner diameter capillary tube is connected to the bottom of the crystal growth volume with one end sealed. Single crystal is initiated from the lower tip of the capillary tube. The long capillary tube serves as a crystal orientation selector, which ensures that only a single grain with a certain crystal orientation will grow into the melt body in the crystal growth volume. Seed crystals are not available since all crystals investigated were new materials. The grown crystals have spontaneous orientation. Part (2) is for melt filtration, which is assembled by fusing a quartz fritz (filter) to the end of a quartz tube. The function of this part is to remove all the refractory contaminations in the raw materials. The refractory contamination is considered to be source of crack and light scattering center, and is detrimental to the crystal quality. The detailed crystal growth procedure will be discussed in the following section. Figure 2.4 illustrates an example showing the refractory contamination was successfully removed by the melt filtration tube before entering the crystal growth volume.

Figure 2.4 Crystal growth ampoule with a melt filtration tube

2.1.4.3. Ampoule preparation

In order to remove both inorganic and organic, each crystal growth ampoule was rinsed by diluted hydrofluoric acid (4.80 – 5.00 %) and de-ionized water before use. Stoichiometric mixture of 99.99% pure raw materials from Sigma Aldrich was prepared inside the MBraun Unilab glove box. Raw materials mixture was weight and fully mixed in an aluminum weighing boat and loaded to the melt filtration tube (2) by an anti-static plastic funnel. Both melt filtration tube (2) and the sealing tube (3) were then inserted into the outer tube (1). Extra caution was taken to make sure sealing tube (3) was not contaminated by the raw materials.

After crystal growth ampoule was properly loaded, it was temporarily sealed with a piece of Parafilm M and transferred out of the glovebox. The ampoule was

then transported to the vicinity of the vacuum system. Temporary seal was removed and the crystal growth ampoule was quickly connected to the vacuum manifold. Evacuation was started immediately. The ampoule was heated at 300 ℃ by the clamshell furnace and continuously evacuated for at least 12 hours. The vacuum drying process ensured the removal of all residual moisture in the raw materials.

A H_2-O_2 torch was used for ampoule sealing. The seal was made at the upper part of the outer tube, where the sealing tube was located. First, a wide flame with low O_2 flow (low temperature) was used to slowly heat the ampoule and soften the quartz. The heat was applied to the area of about 1" wide surrounding the upper part of outer ampoule. During this process, the wall of the outer tube was slowly deformed and collapsed to the sealing tube. Caution was taken not to overheat any particular spot which might cause implosion and ampoule break, since the ampoule held vacuum inside. The upper part of outer tube was heated uniformly 360^o around the tube. After a "ring" of out tube had completely collapsed against the inner sealing tube, a thinner but hotter flame was used to fuse the two tubes together. A circular seal was then completed. In some cases, a white cloudy "ring" structure would show near the seal. This was the de-vitrified region which consisted of micro-cracks induced by the high thermal gradient across the quartz ampoule. A lower temperature flame could be applied to anneal the ampoule and remove the devitrified region.

After crystal growth ampoule was properly sealed. The clamshell temperature was set to a temperature which was 30 - 50 ^{o}C above the melting point of the target compound to melt the raw materials in a vertical position. Molten materials in the melt filtration tube (2) were filtered by the quartz fritz before entering the crystal growth volume at the bottom of the ampoule. Refractory contaminations like carbon or oxy-halides were removed from the material. The ampoule was kept at this temperature for another 12 hours before cooling down to ensure homogeneous mixing. The molten material would also enter the capillary tube at the bottom of the crystal growth volume and later become the seed part for crystal growth. The ampoule was then ready for crystal growth.

2.1.4.4. Vertical Gradient Freeze and Bridgman crystal growth

A Mellen Sunfire Electro-Dynamic Gradient (EDG) Furnace with 24 independent temperature zones was used for single crystal growth. Each zone was heated by resistive heating elements and independently controlled. The length of a single zone was 1”. The furnace was custom modified and a linear translation stage was installed for single crystals growth by conventional Bridgman method. Both Vertical Gradient Freeze (VGF) and Bridgman crystal growth techniques were applied to grow crystals. Figure 2.5 shows a picture of the Mellen EDG furnace and the schematic diagram of thermal zone arrangement.

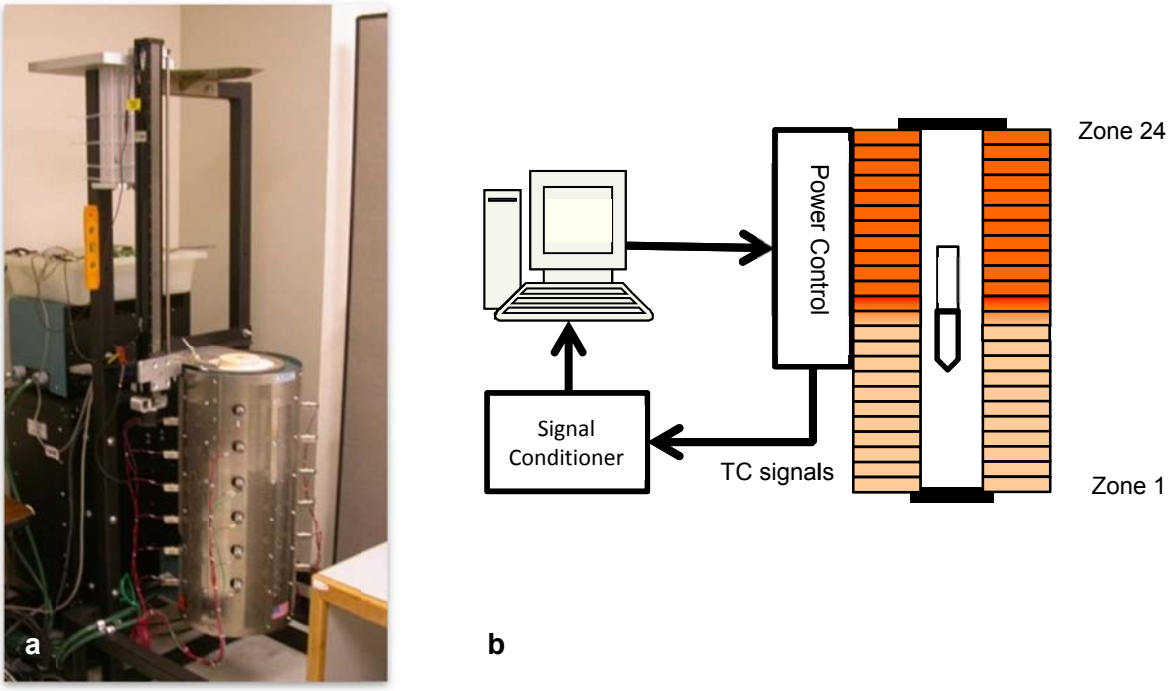

Figure 2.5 Photo (a) and schematic diagram (b) of Mellen Sunfire Electro-Dynamic Gradient (EDG) furnace

In an arrangement for Vertical Gradient Freeze growth, the ampoule was situated and kept stationary in the center of the EDG furnace. The EDG furnace was programmed to have three thermal zones. Upper part of the furnace was programed to perform as one isothermal hot zone, of which the temperature was 20 – 50 ^{o}C higher than the melting point of the compound. Bottom part of the furnace was programed to perform as one isothermal cold zone, which was ~ 50~150 ^{o}C lower than the melting point of the compound. The middle 2~4 zones were used as a transition zone, which connects the hot and cold zone with a thermal gradient of 25~50 ^{o}C/inch. At the beginning the entire ampoule was inside the hot zone. Then thermal gradient was programed to travel through the ampoule from bottom to top at a constant speed of 1 ~ 2 mm/hour. Crystal growth was initiated from the capillary tube at the bottom of the ampoule. Since no seed crystal was used, the grown crystal has spontaneous orientation. Crystal growth was completed when the entire crystal was the cold zone. Then the furnace ramped down at a constant rate of 10 ~ 15 ^{o}C/hour to room temperature. A typical temperature program (crystal growth recipe) for VGF crystal growth was shown in Figure 2.6. In this particular program, the hot zone was set at 750 ^{o}C and the cold zone was set at 600 ^{o}C.

The furnace was also operated in the Bridgman mode. In this case, the hot, cold and transition zones were set at the beginning and kept constant throughout the growth process. A linear translation stage was used to travel the crystal growth ampoule through the thermal gradient at a constant speed of 1 ~ 2

mm/hour. Crystal growth was completed when the entire crystal had been moved into the cold zone. Crystal was then ramped down at a constant rate of 10 ~ 15 ^{o}C/hour to room temperature. Figure 2.7 compares the Vertical Gradient Freeze crystal growth method and the Bridgman crystal growth method.

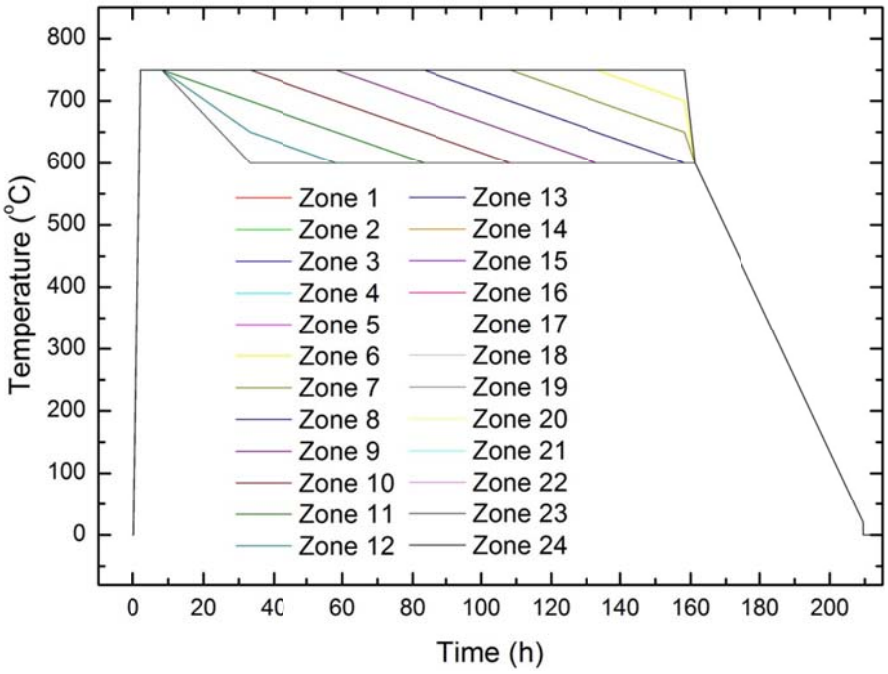

Figure 2.6 Typical temperature programs for Vertical Gradient Freeze crystal growth in Mellen 24 zone Electro-Dynamic Gradient furnace; the hot zone was set at 750 ^{o}C and the cold zone was set at 600 ^{o}C.

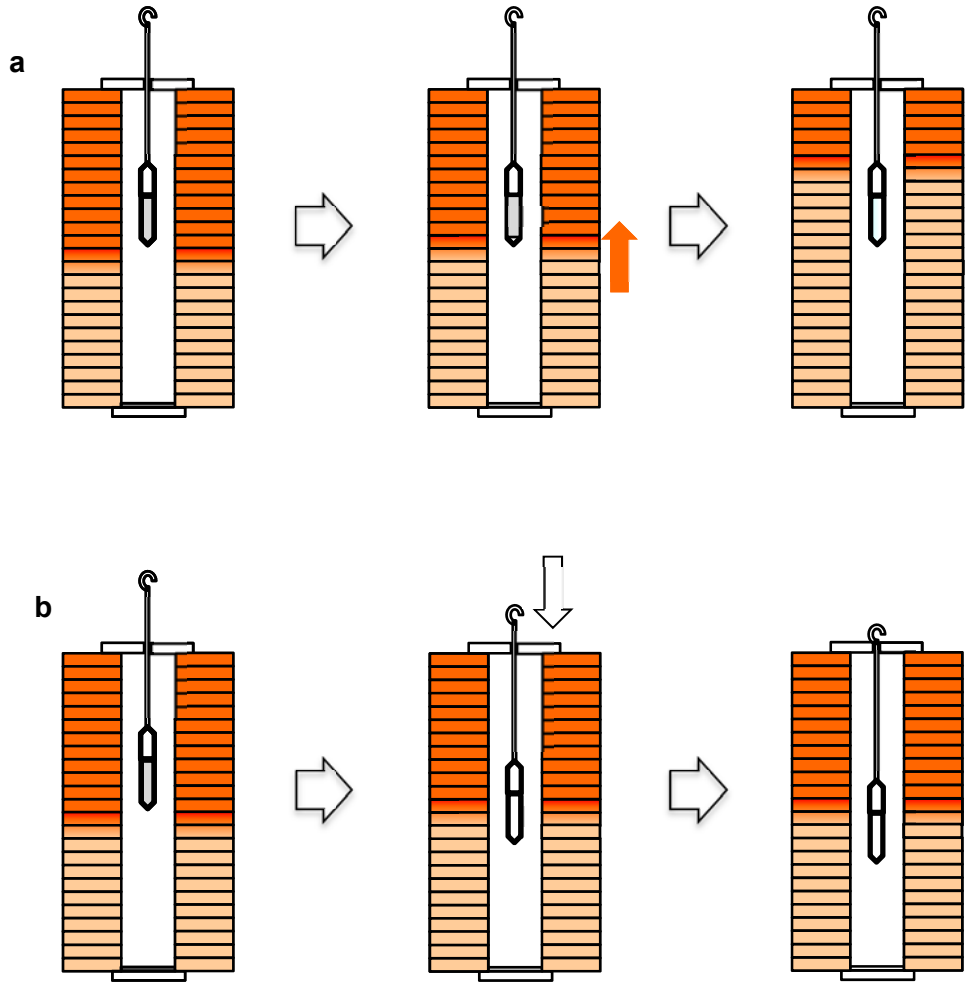

Figure 2.7 Schematic diagrams of (a) Vertical Gradient Freeze crystal growth and (b) Bridgman crystal growth in the Mellen Electro-Dynamic Gradient furnace

2.1.5. Sample preparation

2.1.5.1. Sample cutting and polishing

Due to the hygroscopic nature of the halide materials, special techniques have to be applied to protect the crystal sample from air exposure. As to cutting, conventional high speed disc saw is not applicable since it utilizes aquatic coolant. A diamond wire saw (South Bay Technology model 810) was used to cut the hygroscopic crystals (see Figure 2.8). This saw used 0.001" diamond impregnated stainless steel cutting wire and 99.9% pure glycerin cutting fluid. The saw is capable of executing precise and gentle cuts without using any aquatic cutting fluid. The saw is also compact in size so that it is possible to cut hygroscopic crystals inside a glovebox with inert atmosphere. Figure 2.8 shows a picture of the South Bay Technology 810 diamond wire saw.

Figure 2.8 South Bay Technology 810 diamond wire saw

First, crystal sample was mounted to a graphite sacrificial mounting block by Crystalbond 509 adhesive. The graphite sacrificial mounting block was then bonded to another alumina mounting block by the same kind of adhesive (Figure 2.9). The alumina block fit the sample holder on the wire saw. The mounted sample was then installed on the sample holder and aligned for cutting. The cutting process was done inside a N_2 purged glovebox (LC Technology Solutions benchtop glovebox). Glycerin cutting fluid of 99.9% purity was used to lubricate the wire saw, which did not have any water content and thus protected the samples. Sample polishing was done inside the same glovebox. Samples were hand polished by diamond polishing paste mixed with paraffin oil on Buehler Micro-cloth polishing sheets. Polished surface was then rinsed by pure paraffin oil to remove polishing particles.

Figure 2.9 A mounted single crystal sample for wire saw cutting

2.1.5.2. Hermetic packaging

In order to characterize the candidate samples in room air without damaging its integrity, special protective techniques were developed. For measurements on small polycrystalline samples synthesized during the screening stage, samples were immersed in paraffin oil during measurement. Paraffin oil not only protected the samples from direct air exposure but also optically coupled the samples to the photo sensor. Since paraffin oil does not completely prevent moisture from diffusing into the sample, this technique is only for short term measurements.

For characterizations on large single crystal samples, a special hermetic packaging device was developed. Figure 2.10 shows the picture and the schematic diagram of the hermetic packaging device which was used in the research. Polished samples were first wrapped with two layers of Tetratex PTFE reflective film. One side of the sample was left open for light collection. The unwrapped surface was then bonded to an optical quartz window by Norland Optical Adhesive 60. Light from the sample passed through the window to be collected by the photo sensor. $BaSO_4$ powder was pre-dried at 200 ℃ for 12 hours to remove all residual moisture before using. A scoop of molecular sieve power (desiccant) was later added to the $BaSO_4$ power in order to keep it dry. The mixture was packed in a container and covered the wrapped sample for

better light collection efficiency and drying purpose. The container was then sealed by high vacuum epoxy. The entire preparation process was done inside a N_2-purged glovebox to avoid any moisture exposure.

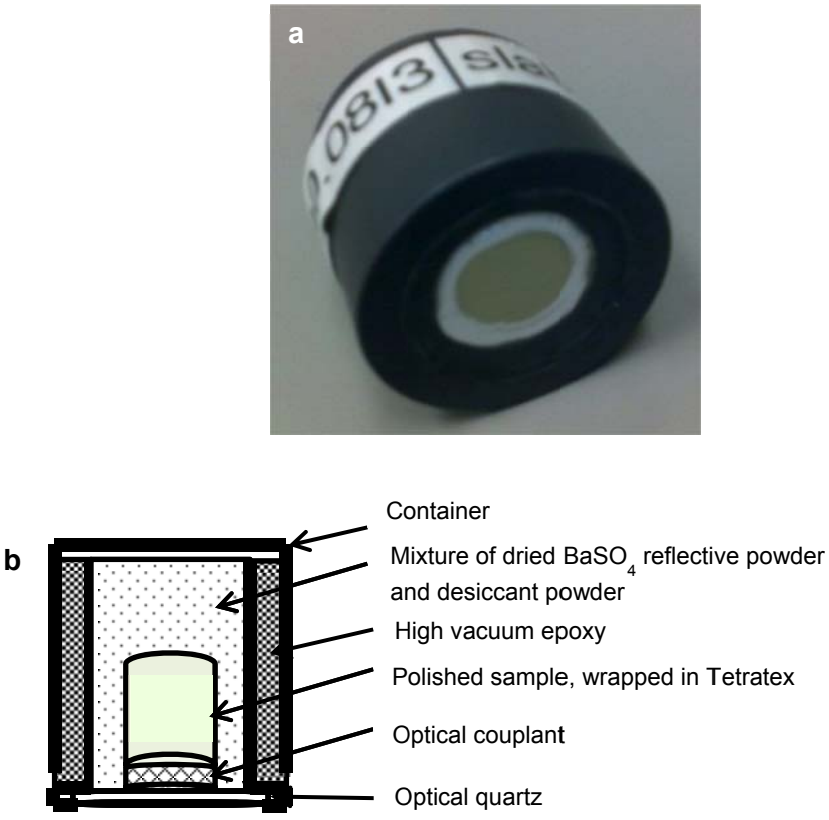

Figure 2.10 Photo (a) and schematic diagram (b) of a hermetic packaging device

2.2. Characterizations

Various characterization techniques were performed to evaluate the scintillation properties and investigate the luminescence mechanism of the halide scintillators. The instrument setups, experimental procedures and methods used to analyze the data are presented for each measurement in the following sections.

2.2.1. X-ray excited luminescence

One of the most important characteristics of a scintillation material is the wavelength of its maximum emission under the excitation from ionizing radiation. To make full use of the scintillation light of a certain scintillation material, its emission spectrum should fall near the wavelength region of maximum sensitivity for the device used to detect the light. For a conventional photomultiplier tube (PMT), the maximum sensitivity is usually around 400 – 430 nm. For example, sensitivity of a Hamamatsu R2059 PMT is at 420 nm. The maximum sensitivity of an avalanche photo diode (APD) is usually located at a longer wavelength. For example, the Hamamatsu C5331-11 APD has its highest sensitivity at 620 nm. For a specific photo-sensor, it is important to select a scintillation material with matching emission wavelength to maximize the conversion efficiency.

X-ray excited luminescence of scintillation materials was measured under continuous X-ray irradiation from an X-ray tube operating at 35 kV and 0.1 mA. Steady state luminescence from the sample was recorded from 200 nm to 800

nm by a spectrometer (ACTON Spectropro 2150i) spectrometer. Emission light of the sample was collected from the same surface which was irradiated by the incident X-rays, which minimizes the effect from sample self-absorption. The experimental setup was shown in Figure 2.11.

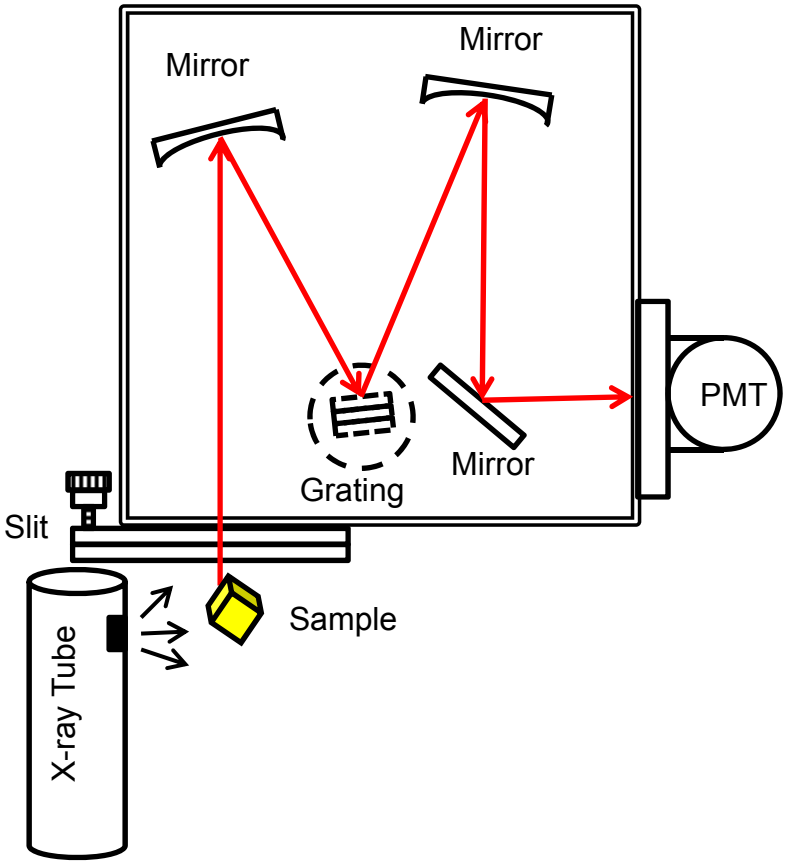

Figure 2.11 Schematic diagram of the experimental setup for X-ray excited luminescence measurements

2.2.2. UV excited excitation and emission spectra

Different from the X-ray, which creates electron-hole pairs in the host material, UV photon excites the luminescence centers (rare earth ions) directly. UV excitation and emission spectra are useful tools to investigate the energy level structure of the luminescence center in scintillation materials.

UV excitation and emission spectra were measured using a UV-Vis spectrofluorometer (Horiba Jobin Yvon Fluorolog-3 spectrofluorometer, Figure 2.12). The spectrofluorometer is equipped with a 450 W Xenon lamp as the light source. The light from the Xenon lamp was selected by the excitation monochromator before reaching the sample. The excitation monochromator ensures that light of a specific wavelength can excite the sample. The sample was placed in the sample chamber and was approximately at 50~60^{o} angle to the incident light beam. This excludes the reflection light from entering the emission monochromator directly. The light emitted from the same surface of the sample pass through the emission monochromator before being detected by a Hamamatsu R928 photomultiplier tube (PMT). The final spectra were corrected for both variation of Xenon lamp intensity at different wavelength and spectral response of the PMT.

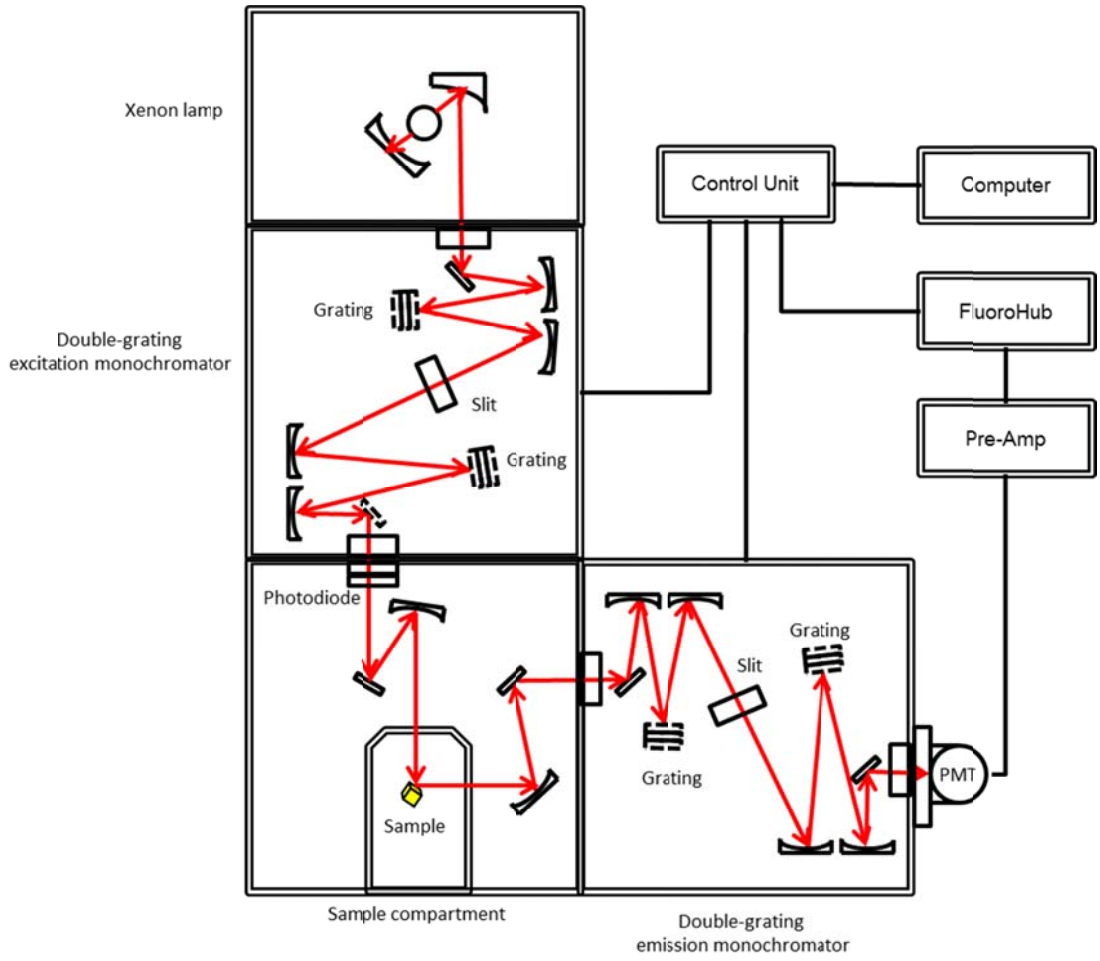

Figure 2.12 Schematic diagram of the experimental setup (HORIBA Jobin Yvon Fluorolog-3) for UV spectroscopy; the photodiode in the sample compartment is for correction of lamp intensity variation at different wavelengths; PMT is Hamamatsu R928

2.2.3. Pulse height spectra and absolute light output

Pules height spectra measurements are one of the most important tools to evaluate the scintillation properties of a scintillation material. Important information like scintillation light output and energy resolution can be extracted from the pulse height spectra.

In a common radiation detector setup, the scintillation material is coupled to a photo sensor, e.g. a photomultiplier tube (PMT), an avalanche photo diode (APD), or a silicon photo multiplier (SiPM). The light emitted by the scintillation material under the irradiation of ionizing radiation is detected by the photo-sensor and converted to electronic signals which are recorded by the readout electronics. When the radiation detector is operated in pulse mode, amplitude of each individual pulse is proportional to the number of photoelectrons generated in the photo-sensor. Thus, a distribution in pulse amplitude can be obtained by histograming a large number of such pulses. The pulse height distribution carries information about the energy of the incident radiation, physical interactions between radiation and scintillation materials, fluctuations in the inherent response of the detector and non-proportional responses of the scintillation materials to radiations with different energies.

Figure 2.13 shows the experimental setup for pulse height spectrum measurements. A ^{137}Cs radioactive source was used to irradiate the sample. ^{137}Cs decays by beta emission to a metastable nuclear isomer of ^{137m}Ba. ^{137m}Ba has a half-life of about 153 seconds and decays to ^{137}Ba with a gamma emission

of 662 keV. Samples were directly coupled to Hamamatsu R2059 PMT. Dow Corning Q2-3067 optical grease was used as optical couplant for packaged samples. Bare samples were coupled to the PMT by pure paraffin oil. A piece of Tetratex TX3104 PTFE film or a hemispherical Spectralon reflector of 25 mm radius was used as the light reflector depending on sample geometries. Light pulses from the sample were converted to electrical pulses (photoelectron pulses) by the PMT and then shaped and amplified by the readout electronics. A Tukan 8k Multi-Channel Analyzer was used to analyze distribution of the photoelectron pulses and output it in form of a histogram, which is the pulse height spectrum.

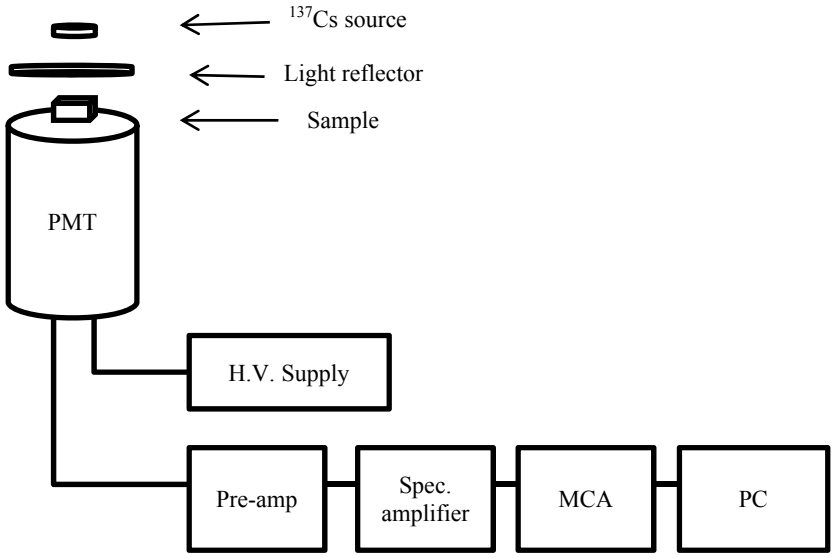

Figure 2.13 Schematic diagram of the experimental setup for pulse height spectra measurements, with PMT (Hamamatsu R2059), Pre-amp = pre-amplifier (Canberra 2005), Spectroscopy amplifier (ORTEC 672), MCA = Multi-channel analyzer (Tukan 8k), and PC is for data processing and recording

An example of pulse height spectrum measured on a $CsSrI_3$:Eu crystal with a ^{137}Cs is shown in Figure 2.14. The abscissa is a linear pulse amplitude scale that runs from zero to a value larger than the amplitude of any photoelectron pulse observed. The abscissa possesses units of pulse heights (volts), which are often displayed in “channel” numbers. Each channel represents for a certain range of pulse height. The ordinate is the number of counts which is collected within the range of each specific channel. Since the height of the electrical pulse is proportional to the number of photoelectrons generated inside the PMT and the number of photoelectrons is proportional to the number of photons detected by the PMT with some correction, the pulse height spectrum presents the amplitude distribution of light pulses emitted by a scintillator within a certain amount of time.

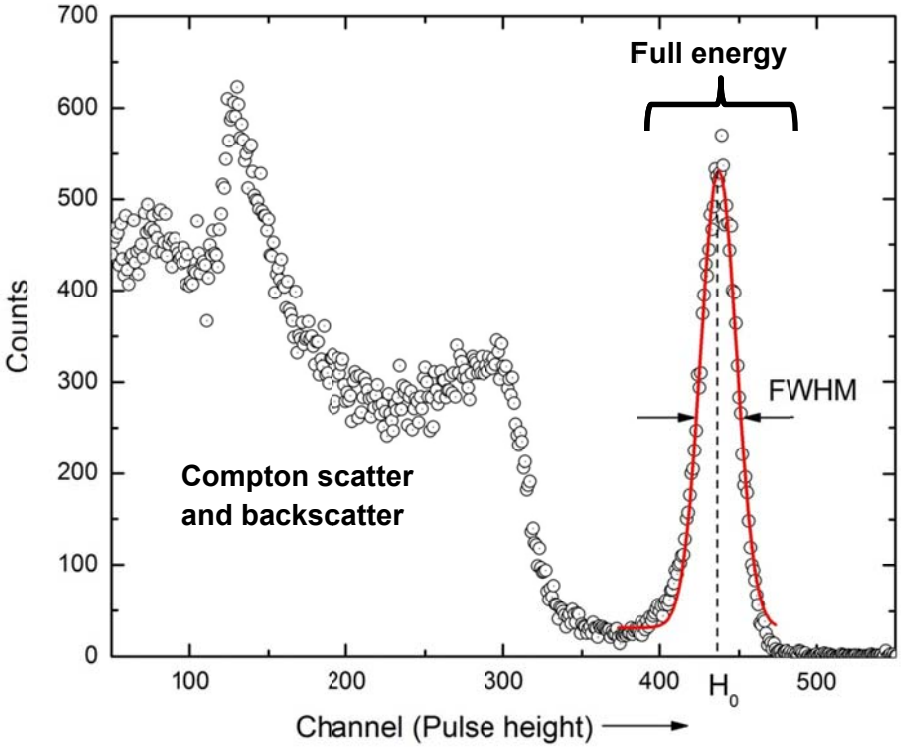

Figure 2.14 Pulse height spectrum of $CsSrI_3$:Eu measured by ^{137}Cs source; the full energy peak is fitted by a Gaussian function

There are two regions in pulse height spectrum of ^{137}Cs. The left part in the spectrum consists of a continuous region of counts, which is commonly referred as the Compton continuum. The Compton continuum is mainly caused by 662 keV photons which scatter in the sample with the scattered photon escaping the sample. Only part of the energy of the incident γ photon is absorbed in one Campton scattering event. There are also events in the Compton continuum which are caused by backscattered γ photon from the materials surrounding the sample. In this case, the absorbed energy is also lower than the full energy of the incidence γ photon. If the energy of an incident γ photon is entirely absorbed, the photoelectron pulses produced in the PMT is the highest. This gives rise to the full-energy photo peak which is the rightmost peak in the spectrum. Since height of pulses reflects the number of photo-electrons, the full-energy photo peak in Figure 2.14 represents the number of photoelectrons the scintillation material can produce in the PMT when one incident 662 keV γ-ray photon is completely absorbed.

Scintillation light output is defined as the number of photons produced by the scintillation material per MeV of absorbed γ-ray energy (photon/MeV). To calculate the number of photons (N_{ph}), we need to measure the number of photo electrons generated in the PMT per MeV of absorbed γ-ray energy (N_{phe}). The number of photoelectrons can be calculated by comparing the centroid of the full-energy photo peak with that of the single electron spectrum [41]. The conversion

ratio from photons to photoelectrons is given by the detection efficiency of the PMT, which is given by [41]:

$$\eta_D(\lambda) = Q.E.(\lambda) \times \varepsilon \times \eta_L$$

where $Q.E.(\lambda)$ is the wavelength-dependent quantum efficiency of the PMT, ε is the charge collection efficiency of the photoelectrons emitted from the photocathode of the PMT and η_L is the light collection efficiency. Because the samples are usually much smaller than the size of the PMT and the samples are situated in the center of the PMT entrance window during measurements, charge collection efficiency ε is assumed to be unity in all measurements. The light collection efficiency η_L is also assumed to be unity because the reflectance of both reflectors used in the measurements, Spectralon and Tetratex, is higher than 99%. The actual scintillation light output for a particular scintillator may be slightly higher than the measured value based on the above assumptions.

$Q.E.(\lambda)$ is dependent on the wavelength of the scintillation light. The integral quantum efficiency (*I.Q.E.*) can be calculated by:

$$I.Q.E. = \frac{\int I_{RL}(\lambda) \times Q.E.(\lambda) \times d\lambda}{\int I_{RL}(\lambda) \times d\lambda}$$

where $I_{RL}(\lambda)$ represent the relative intensity of X-ray excited emission spectrum of the sample at wavelength λ.

Finally, the absolute scintillation light output is given by:

$$N_{ph} = \frac{N_{phe}}{I.Q.E. \times \varepsilon \times \eta_L}$$

Energy resolution is another important characteristic of a scintillation material. It refers to the ability of a scintillation detector to distinguish different radiation energy peaks. Energy resolution (*R*) of scintillation detector is conventionally defined as the full width at half maximum (FWHM) of the full-energy photo peak divided by the location of the peak centroid H_0. FWHM can be obtained by fitting the photo peak with Gaussian function. The energy resolution (*R*) is a dimensionless quantity and is usually expressed in percentage.

$$R = \frac{FWHM}{H_0} \times 100\%$$

2.2.4. Scintillation decay time

For scintillation decay time determination, the time-correlated single photon technique originated by Bollinger and Thomas was used [42]. The schematic diagram of the experiment setup is shown in Figure 2.15. In this setup, samples were directly coupled to the START PMT for enhanced light collection. STOP PMT was at a distance from the sample. An adjustable aperture was used to ensure that only single photon could reach the STOP PMT. Samples were excited by 662 keV γ-rays from ^{137}Cs source. For a single event, the scintillation light pulse was detected by both START and STOP PMTs and converted by Constant Fraction Discriminators (CFDs) to timing pulses. A scaled pulse was generated by the Time-Amplitude-Converter (TAC). Height of the TAC pulse was proportional to the difference between the START and STOP pulses. Pulse height distribution of a large number of TAC pulses was analyzed by the Multi-

Channel Analyzer (MCA) and histogramed by the computer. The scintillation time profile was fit by single- or multiple- exponential decay functions In order to calculate the decay constant(s), which is the scintillation decay time(s) of a certain scintillation material. The fitting function was given by:

$$N = A_1 exp\left(-\frac{t}{\tau_1}\right) + A_2 exp\left(-\frac{t}{\tau_2}\right) + \cdots$$

where A_1, A_2, … are amplitudes for exponential components.τ_1 , τ_2 , … are scintillation decay times. An example for scintillation time profile is shown in Figure 2.16. The scintillation time profile is fit by a single exponential decay function. Scintillation decay time measured for this particular sample (SrI_2:1%Eu) is 670 ns.

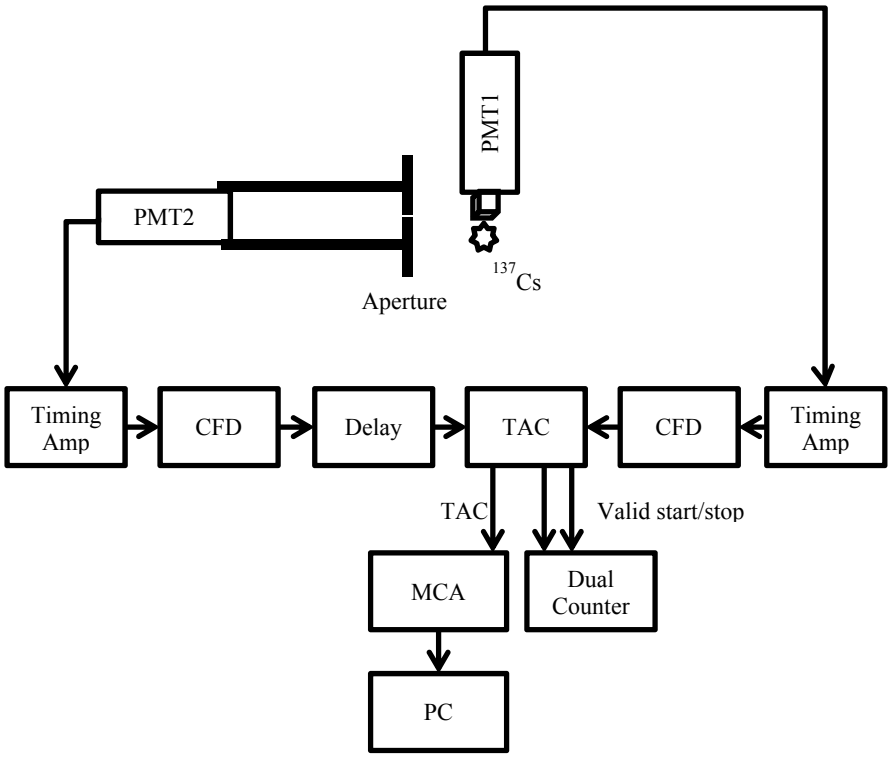

Figure 2.15 Schematic diagram of the experimental setup for scintillation decay time determination, with PMT1 = START PMT (Hamamatsu R2059), PMT2 = STOP PMT (Hamamatsu R2059), Timing Amp. = Timing amplifier (ORTEC 474), CFD = Constant Fraction Discriminator (ORTEC 935), Delay (ORTEC 425A), TAC = Time amplitude converter (ORTEC 576), MCA = Multi-channel analyzer (Tukan 8k), Dual Counter (ORTEC 994), and PC is for data processing and presentation.

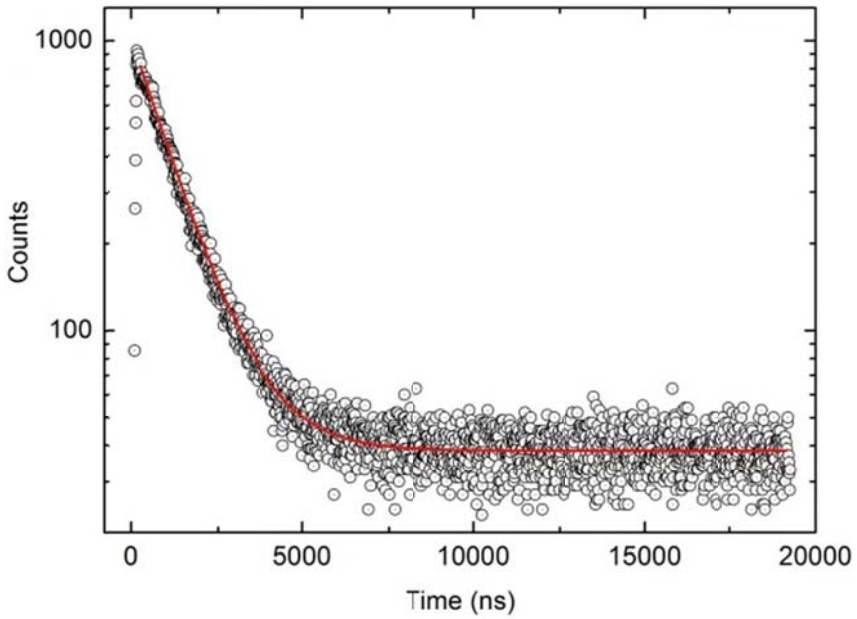

Figure 2.16 Scintillation time profile of SrI_2:1%Eu; the solid red curve is a single exponential fitting of the measured data

2.2.5. Scintillation non-proportionality

An ideal scintillation material would produce a number of scintillation photons that is directly proportional to the radiation energy deposited in the material. However, all inorganic scintillator are characterized by some degree of light output non-proportionality. One effect from the scintillation non-proportionality is the broadening of pulse height spectra [43], which decreases the energy resolution of the scintillation material. Scintillation non-proportionality also limits the applications of a scintillation material in proportional spectrometer [44].

For non-proportionality characterization, a set of γ-ray sources (namely ^{137}Cs, ^{22}Na, ^{109}Cd, ^{133}Ba, ^{57}Co, ^{60}Co, ^{241}Am, ^{54}Mn) were used to obtain various γ-ray excitation energies. Pulse height spectra were recorded under the excitation from these sources, respectively. Gaussian fitting functions were applied to determine the centroids for photopeaks related to various γ-ray energies. Scintillation light outputs were calculated and presented as a function of deposited γ-ray energies.

2.2.6. Thermoluminescence glow curve

Thermoluminescence is the thermally stimulated emission of light following the previous absorption of energy from radiation [45]. Information about energy levels of charger carrier traps can be extracted from thermoluminescence curve. A schematic diagram of the experimental setup for thermoluminescence measurement is shown in Figure 2.17. The crystal was first cut to approximately 3 × 3 × 3 mm^3 cubes. The sample was not polished to avoid any contamination

from polishing particles and oil. The sample was then bound to a copper sample holder (cold finger) on an Advanced Research Systems DE-202 closed cycle compressed helium cryostat by a piece of double-sided carbon tape. An L-shaped sample clamp was used to press the sample against the copper sample holder for enhanced thermal conductivity. After the sample was properly mounted, the vacuum shroud on the DE-202 cryostat was replaced and evacuation was started immediately. A schematic diagram of the ARS cryostat is shown in Figure 2.18. The radiant heat shield was not used because it would block the X-ray beam in the current configuration.

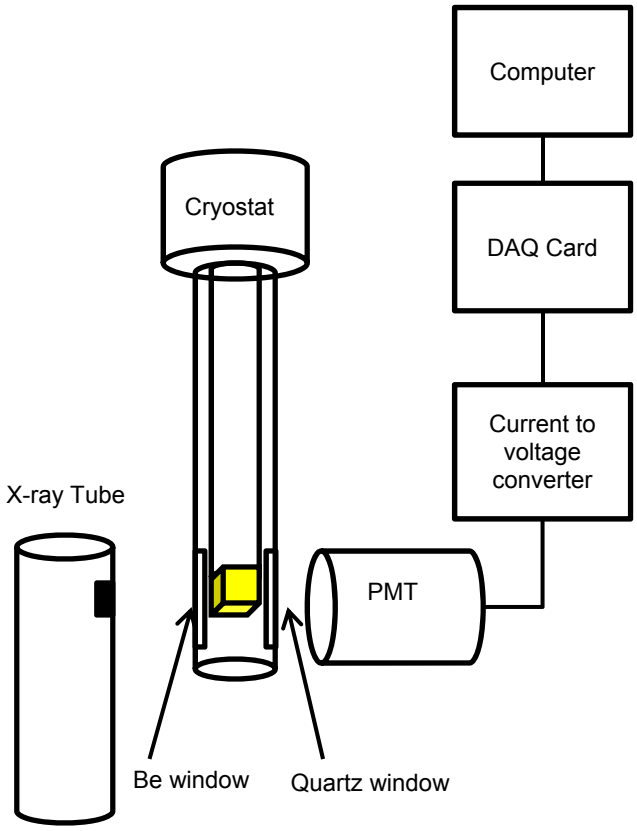

Figure 2.17 A schematic diagram of the experimental setup for thermoluminescence measurements; Cryostat = Advanced Research Systems DE-202 closed cycle compressed helium cryostat; PMT = Hamamatsu R2059; Current to voltage converter was custom-made; DAQ card = National Instruments data acquisition card PCI-1200

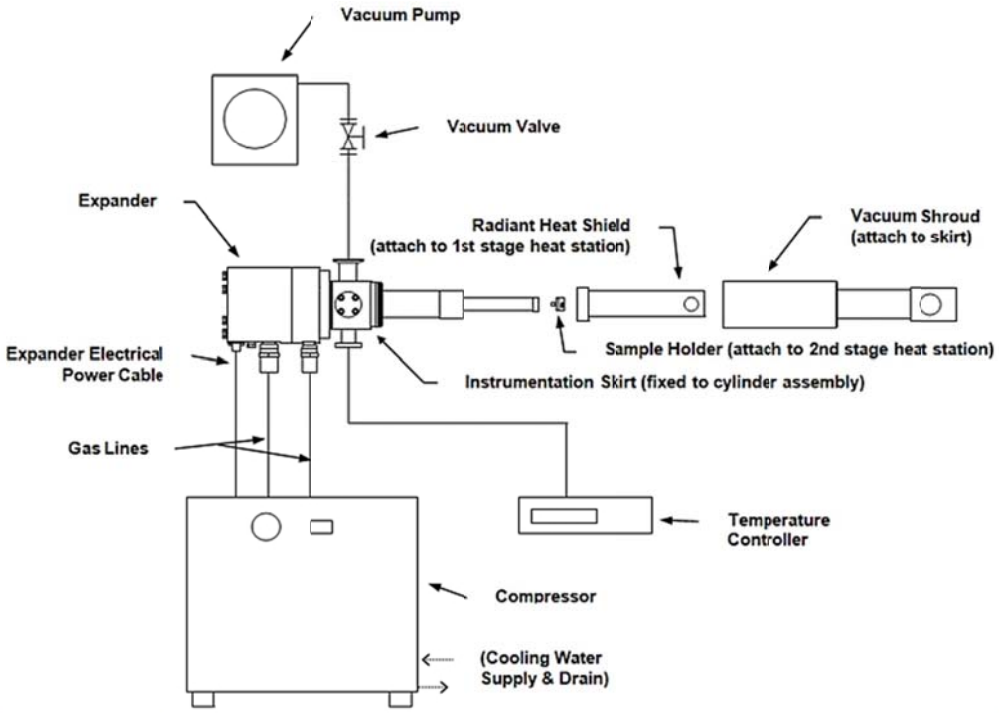

Figure 2.18 Schematic diagram of the Advanced Research Systems DE-202 closed cycle compressed helium cryostat

(http://www.arscryo.com/TechNotes/CryocoolerPrincipleofOperation.html)

Helium compressor was then turned on to cool down the sample to low temperature. After the sample was cooled to 30 - 40 K, the sample was irradiated with X-rays (35 kV, 0.1 mA) through a beryllium window on the vacuum shroud for approximately 15 min. The steady state luminescence from the sample was meanwhile recorded by a Hamamatsu R2059 PMT. After the X-ray generator was turned off, the sample was heated to 600 K at a constant rate of 0.15 K/s. At this heating rate, the temperature difference between the sample and the sample holder (thermal lag) was estimated to be 2 ~ 3 K. Temperature of the sample holder was measured by a Type E thermocouple and a Chromel/Gold thermocouple. During the process of heating, luminescence emitted by the crystal was recorded by the Hamamatsu R2059 PMT as a function of temperature. A custom-written LabView program was used for temperature control and data recording.

Figure 2.19 shows an example of thermoluminescence glow curve measured by the above described setup. For the purpose of easy comparison, the intensities of the thermoluminescence glow peaks are normalized to the level of steady state luminescence at low temperature. Detailed discussion on data analysis of thermoluminescence will be provided in the following chapter.

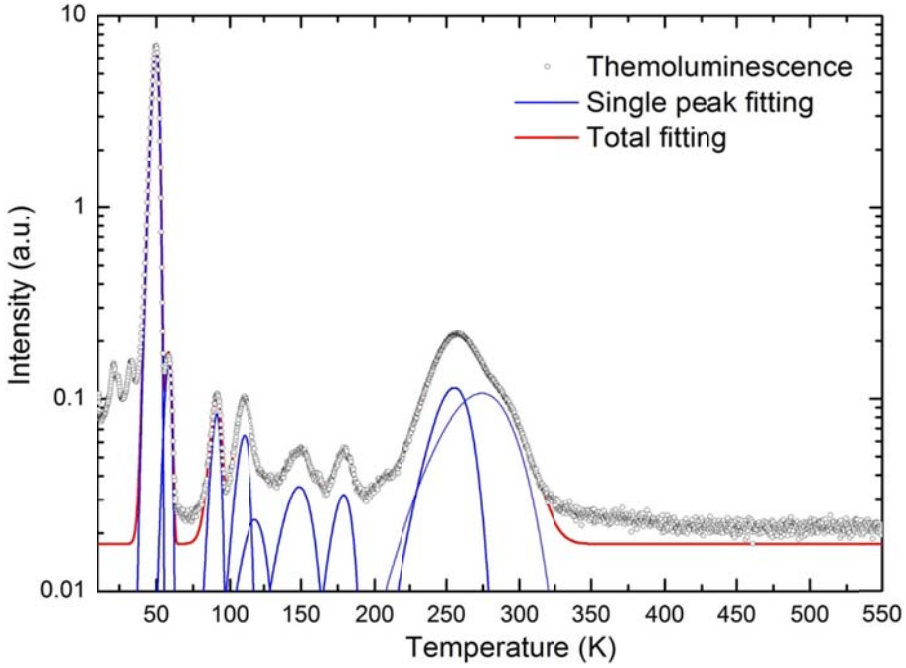

Figure 2.19 Thermoluminescence glow curve of SrI_2:1%Eu; The thermoluminescence peaks were fitted by the first-order-kinetic model.

CHAPTER III EXPERIMENTAL RESULTS

3.1. Materials screening

Ce^{3+} and Eu^{2+} activated scintillators in three binary systems: Alkali Halide – Rare Earth Halide ($AX–REX_3$), Alkali Halide – Alkaline Earth Halide ($AX–AEX_2$) and Alkaline Earth Halide – Rare Earth Halide ($AEX_2–REX_3$) were systematically studied.

The selection of candidate materials was based on: (a) the composition of the material must be a congruent melting composition. The criterion is required by the nature of melt growth; (b) there is no low temperature solid-solid phase transition for the specific composition. Low temperature solid to solid transformation is detrimental to the optical quality of the grown crystal, especially when there are big mismatch in lattice parameters, thermal expansion coefficients, and elastic modus between the two phases. These mismatches can easily cause crystal cracking in the cooling down process after crystal growth has finished. However, an optimized cooling thermal profile may minimize the problem. All available phase diagrams in these two systems will be studies and analyzed for candidate materials. (c) The constituent atoms are generally required to be optically inactive in order not to interfere with the luminescent activators. (d) The detection of gamma radiation requires high effective Z in the detector materials to get high stopping power. Otherwise the signal to noise ratio may to too low.

Candidates were synthesized in small quantities for rapid screening. Synthesized materials were evaluated in terms of their optical and scintillation properties including scintillation light output, scintillation decay time, X-ray excited luminescence. A UV lamp capable of producing 255 nm and 366 nm UV light was used for initial screening of the candidate materials. However, “no light” under the UV lamp does not necessarily mean luminescence from the particular sample was quenched at all light excitation. Scintillation light output measurements were later carried out to confirm whether there was any luminescence from the sample. A total of 42 candidate compositions were synthesized and characterized. Both Eu^{2+} and Ce^{3+} were introduced to the binary scintillation materials as activators. Eu^{2+} was used as dopants in compound which has 2+ cation sites which Ce^{3+} was used in compound with 3+ cation sites. Table 3.1 listed some materials synthesized and characterized.

Table 3.1 Selected results for melt synthesis

Host	***Dopant***	***Observations under 255 or 366 nm UV***	***L.O. (BGO is 100)***	***Scint. Decay (ns)***	***X-ray Ex. Emission Peak (nm)***
$CsGd_2Cl_7$	1% Ce	Bright	560	60	392
$CsSrI_3$	1% Eu	Bright	329	2200	458
$CsEuI_3$	None	Bright	300	3400	465
Cs_3EuI_5	None	Bright	n.p.*	300 (10%), 2600 (90%)	

*"n.p." means no resolvable photopeak.

Among all halide scintillation materials explored, about ten compositions were found not to produce any visible light under either 255 nm or 366 nm UV light. The quenching of light has several possible explanations. First, there might be an overlap between the energy levels of the activators and the valence band or conduction band of the host material. Electron hole pairs created by the incident radiation were not able to be captured by and recombine at the luminescence center. The majority of recombination was non-radiative and happened at defects levels in the crystal. Another possible might be that the distribution coefficient of the activator (Ce^{3+} or Eu^{2+}) in the host material was too small. Activator ions were not properly incorporated into the host crystal matrix to produce detectable light emission. This might be due to big difference in ionic radii between the activators and the cations in the host materials.

Fifteen candidate materials were found to be highly promising for radiation detection applications. Due to limited time and equipment availability, three binary halide materials: Ce_3EuI_5, $CsGd_2Cl_7:Ce^{3+}$ and $CsSrI_3:Ce^{3+}$ have been selected for single crystal growth and further exploration in this research. Crystal growth and characterization details of these three particular materials will be discussed in the following sections.

3.2. Single crystal Cs_3EuI_5 for γ-ray spectroscopy

3.2.1. Synthesis

Cs_3EuI_5 was pre-synthesized using the reaction $3CsI + EuI_2 \rightarrow Cs_3EuI_5$ before crystal growth. Stoichiometric mixture of CsI and EuI_2 was mixed. Both materials are anhydrous beads with at least 99.99% purity. The starting materials were then loaded to a pre-cleaned and pre-baked quartz ampoule for synthesis. The synthesis ampoule was evacuated to a vacuum of 1×10^{-6} mbar before sealing. After the synthesis, the material was loaded to a specially designed ampoule for single crystal growth. Cs_3EuI_5 single crystal was grown by the Vertical Gradient Freeze (VGF) technique. A Mellen 24-zone Sunfire Electro-Dynamic Gradient (EDG) furnace was used to grow crystals. The furnace is capable of dynamically controlling the thermal profile inside the furnace. The moving thermal gradient swept through the ampoule at a constant speed of 1 mm/hour. After the growth was finished, the crystal was cooled down to room temperature at a speed of 10 ℃/hour. The crystal was cut, ground and polished by hand in the glove box.

80 mm long and 10 mm in diameter single crystal Cs_3EuI_5 was grown by the VGF technique. The crystal has a few cracks and is translucent with light yellow color, which is possibly due to contamination in the raw materials. I was able to harvest and prepared ~3 mm thick polished sample slices for scintillation characterization. Figure 3.1 shows Cs_3EuI_5 in the crystal growth ampoule. Cs_3EuI_5 crystal is hygroscopic. Without any protection, Cs_3EuI_5 will absorb the moisture in the air, change color in several minutes and completely decompose

in several hours. Even if the crystal was stored in the glove box and immersed in extra-dry mineral oil, Cs_3EuI_5 still changes color gradually. The hygroscopicity of this crystal requires special packaging technique to maintain its optical and scintillation properties. Polished samples were carefully encapsulated in a custom-made packaging device with an optical quartz window for scintillation and optical measurements. Tetratex teflon membrane was used as the reflector.

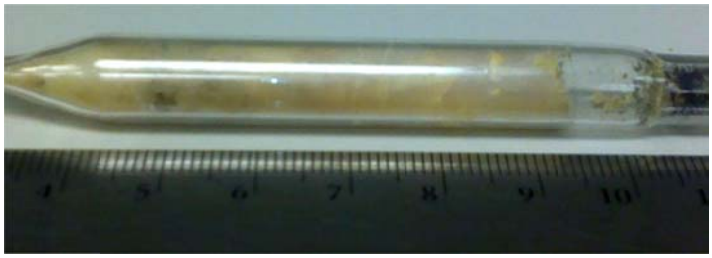

Figure 3.1 Cs_3EuI_5 single crystal in crystal growth ampoule

3.2.2. Characterizations

Figure 3.2 shows the X-ray excited luminescence spectra of Cs_3EuI_5 measured at room temperature. The X-ray excited luminescence spectrum shows a single emission peak at 463 nm, which is slightly shorter than the UV excited emission peak.

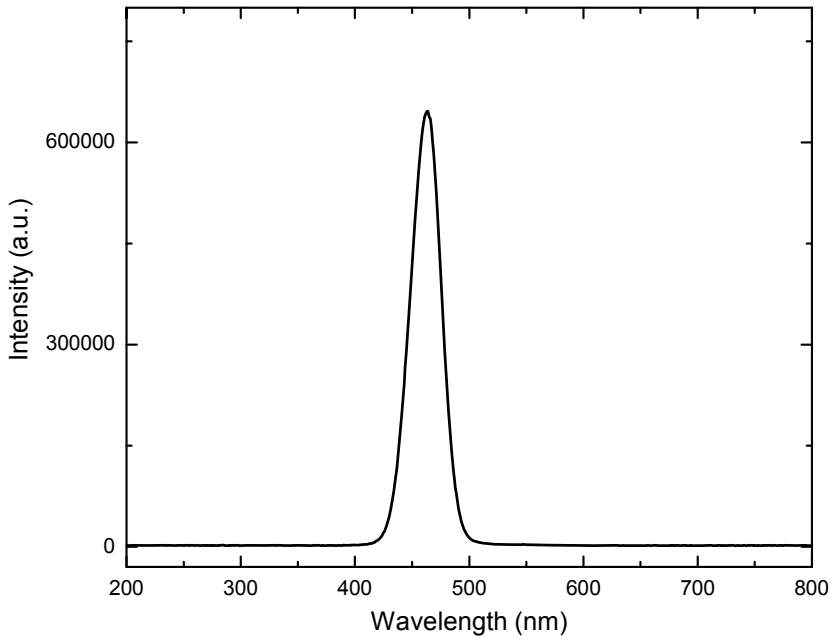

Figure 3.2 X-ray excited luminescence spectrum of Cs_3EuI_5

For UV-Vis emission and excitation, Cs_3EuI_5 exhibits a broad excitation band from 270 nm to 460 nm, as is shown in Figure 3.3. The broad excitation band was also observed in Ba_2CsI_5 and BaBrI [17, 18]. Emission spectrum of Cs_3EuI_5 shows a single emission peak at 473 nm with a Full Width Half Maximum (FWHM) of ~ 20 nm, which corresponds to the 5d-4f transition of Eu^{2+}.

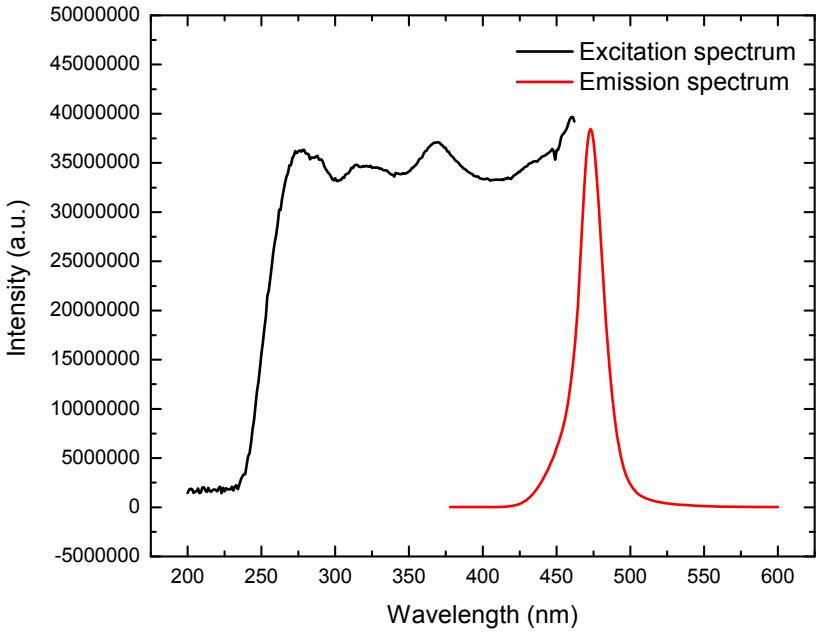

Figure 3.3 UV-Vis excitation and emission spectra of Cs_3EuI_5

Figure 3.4 shows the pulse height spectrum for Cs_3EuI_5. The photopeak was fitted with Gaussian functions to determine the centroid of the peak and the energy resolution. The fitting shows the full energy peak and an escape peak. To estimate the absolute light yield, the crystal-PMT quantum efficiency was calculated based on the wavelength response of Hamamatsu R2059 and X-ray excited luminescence spectra of the crystals (Figure 3.2). The absolute light output for Cs_3EuI_5 sample is calculated to be ~39,000 ph/MeV. The energy resolution is about ~10% for the particular sample we have measured. Better energy resolution can be expected for a higher quality crystal with better

transparency and less colorization.

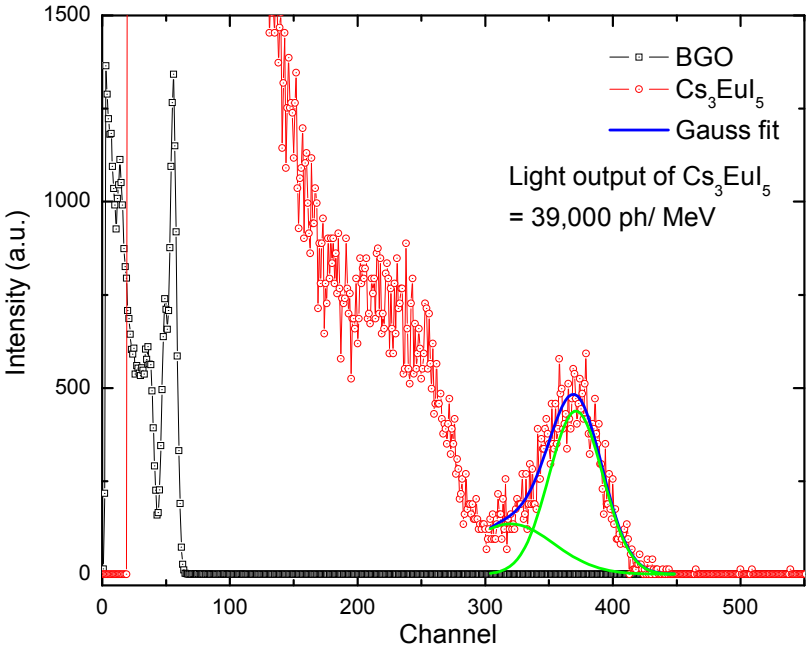

Figure 3.4 Pulse height spectrum of Cs_3EuI_5 measured with ^{137}Cs source compared with a BGO reference

Figure 3.5 shows the scintillation time profile for Cs_3EuI_5 measured with ^{137}Cs source. The decay curve was fitted with a double-exponential decay function. The primary decay component has a time constant of ~4040 ns and accounts for 95.6% of the total light output. A secondary component with a time constant of ~460 ns accounts for the remaining light emission.

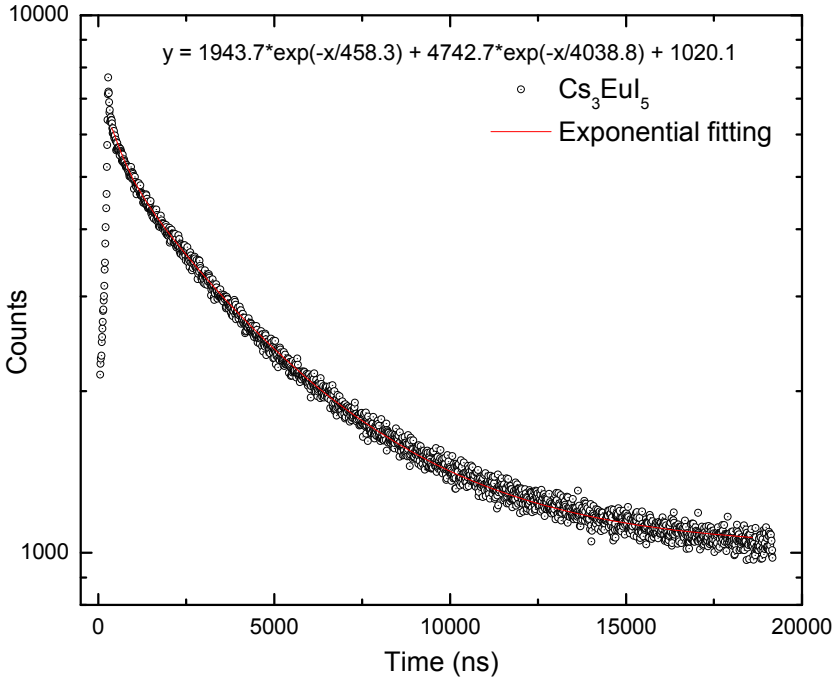

Figure 3.5 Scintillation time profile of Cs_3EuI_5

3.2.3. Summary

All UV and X-ray excited spectra suggest the emission from Cs_3EuI_5 is solely from Eu^{2+} 4d-5f transition. X-ray excited luminescence shows the emission of Cs_3EuI_5 is at 463 nm, which is a favorable wavelength for photomultiplier tube. The scintillation decay of Cs_3EuI_5 consists of two exponential components: a fast component of 460 ns (4.4%) and a slow component of 4040 ns (95.6%). The scintillation light yield is calculated to be 39,000 ph/MeV with ~10% energy resolution at 662 keV. These attractive scintillation properties make this material very promising for γ ray spectroscopy applications, especially for SPECT

imaging.

3.3. Single crystal $CsGd_2Cl_7:Ce^{3+}$ for γ-ray and neutron detection

3.3.1. Synthesis

First a stoichiometric mixture of anhydrous 99.99% pure CsCl, $GdCl_3$ and $CeCl_3$ (3 at% with respect to Gd) beads was made in a N_2 purged glovebox and loaded into a quartz ampoule. The ampoule was pre-cleaned and degreased by lightly etching with a dilute HF solution and rinsed with deionized water. After loading of the raw materials, the ampoule was evacuated to 10^{-6} mbar and sealed with a hydrogen torch. The sealed ampoule was heated in a box furnace to 850°C and held for 15 hours to melt and react the raw materials. Several single crystals of $CsGd_2Cl_7:Ce^{3+}$ with volumes of ~0.1-0.2 cm^3 spontaneously nucleated during cool-down.

After synthesis the crystals were removed from the ampoule and stored in a glove box to prevent exposure to the ambient atmosphere. Crystal plates ~ 10 × 10 mm and ~1-2 mm thick with freshly cleaved and unpolished surfaces were harvested and used for characterizations. Due to the small difference in ionic radii of Ce^{3+} and Gd^{3+}, some degree of Ce segregation could be expected, but no measurement of Ce distribution in the material was performed.

The $CsGd_2Cl_7$:Ce ingot was ~40 mm long and ~10 mm diameter and comprised a number of crystallites. The ingot exhibited a layered structure with weak cleavage planes. The cleaved plates were transparent with smooth and

shiny surfaces as seen in Figure 3.6. The thickness of the individual layers varied from 0.1 to 1 mm. Visual observations indicate $CsGd_2Cl_7:Ce^{3+}$ is less hygroscopic than, e.g. NaI:Tl, which makes handling and storing of the samples easier.

Figure 3.6 Crystals of $CsGd_2Cl_7:Ce^{3+}$ synthesized in a vacuum sealed ampoule; the above sample is approximately 5 mm long in the horizontal axis.

The X-ray excited luminescence spectrum of $CsGd_2Cl_7:Ce^{3+}$ recorded at room temperature is shown in Figure 3.7. The sample shows a Ce^{3+} emission band with peak maximum at 395 nm. Photoluminescence excitation and emission spectra of $CsGd_2Cl_7:Ce^{3+}$ are shown in Figure 3.8. The emission spectrum for the $CsGd_2Cl_7:Ce^{3+}$ 3% sample excited at 265 nm shows a peak with maximum emission at 388 nm. The excitation spectrum with emission wavelength at 388 nm shows two major excitation bands with maxima at 265 nm and 337 nm, which is typical for Ce^{3+} 5d-4f transitions. There are additional excitation bands at 273-

278 nm which can be attributed to the Gd^{3+} absorption [46, 47]. These excitation bands indicate possible $Gd^{3+} \rightarrow Ce^{3+}$ energy transfer since 388 nm is not an emission wavelength of Gd^{3+} in $CsGd_2Cl_7$ [46].

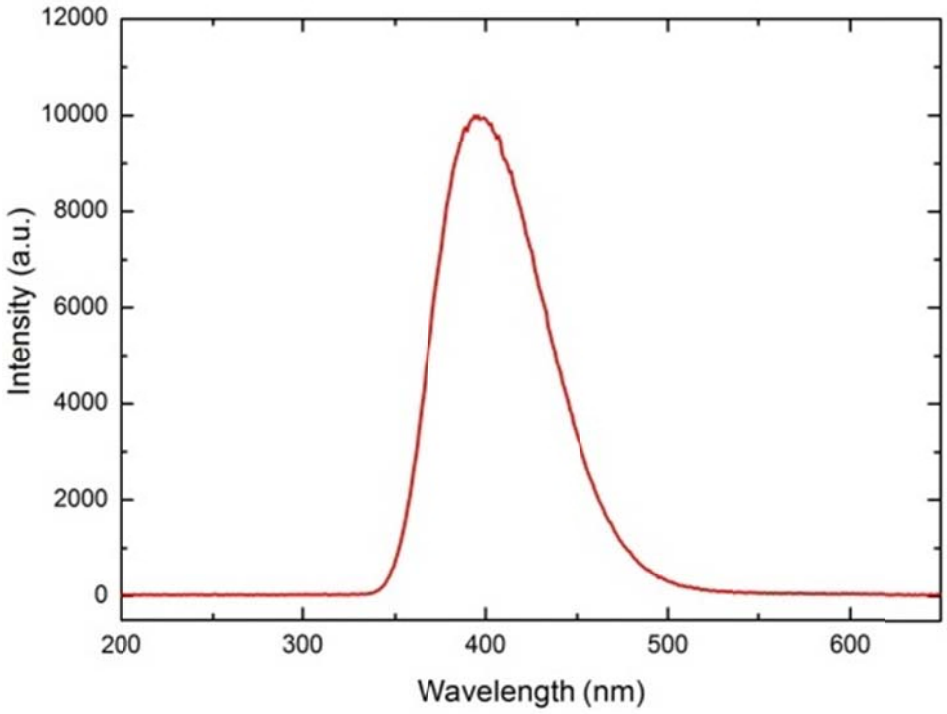

Figure 3.7 X-ray excited luminescence spectra of $CsGd_2Cl_7$: Ce^{3+}measured at room temperature

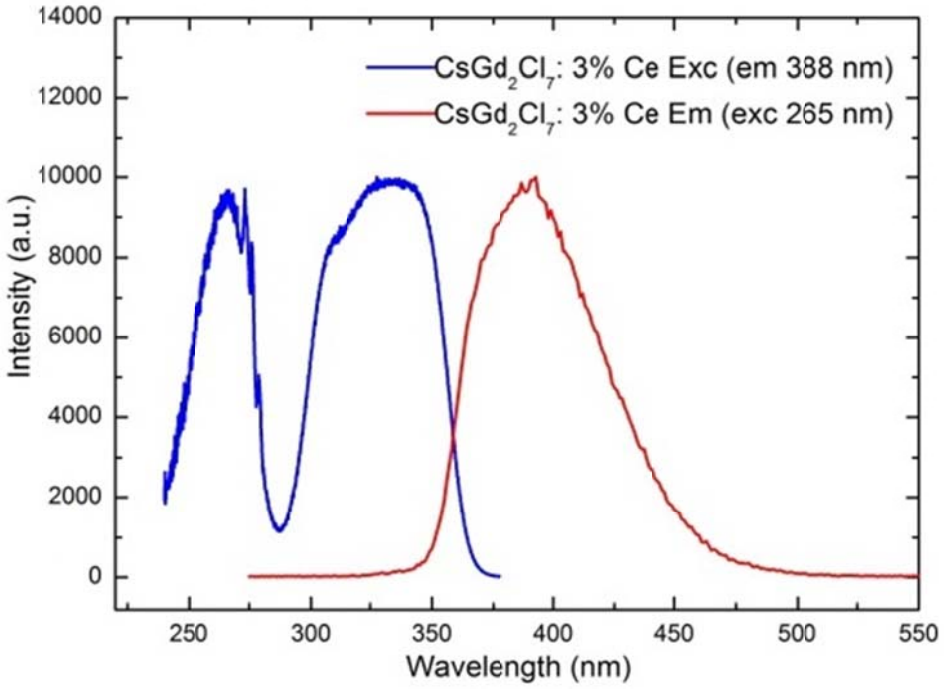

Figure 3.8 Emission and excitation spectra of $CsGd_2Cl_7$: Ce^{3+}

The scintillation decay profile of $CsGd_2Cl_7:Ce^{3+}$ can be described as double exponential decay with a principal component of ~60 ns (85% of total light), Figure 3.9. A secondary component of ~300 ns (15% of total light) was observed as well.

Figure 3.10 shows an energy spectrum of a $CsGd_2Cl_7:Ce^{3+}$ crystal compared with a BGO reference crystal. The 662 keV gamma ray photo peak demonstrates that the relative photoelectron yield of $CsGd_2Cl_7:Ce^{3+}$ is approximately 7 times that of BGO when using a PMT with a bi-alkali photocathode. The absolute light output was calculated to be ~38,000 ph/MeV when taking into account the quantum efficiency of the PMT for each crystal's emission spectrum. The energy resolution at 662 keV is ~10%. As the crystal growth technique is refined in the future, we expect that the light output and energy resolution will improve.

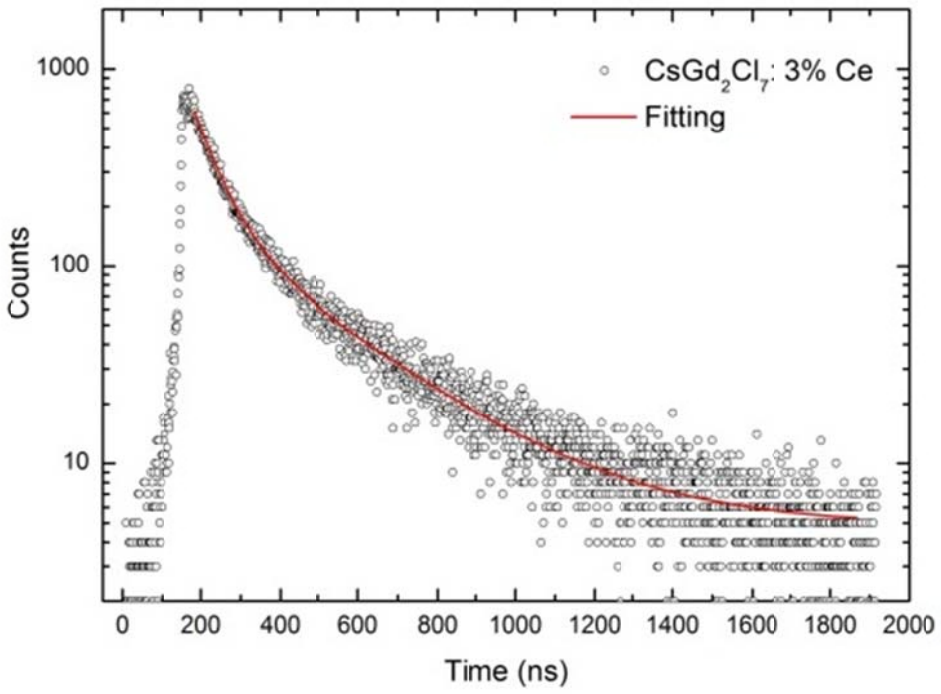

Figure 3.9 Scintillation time profile of $CsGd_2Cl_7:Ce^{3+}$

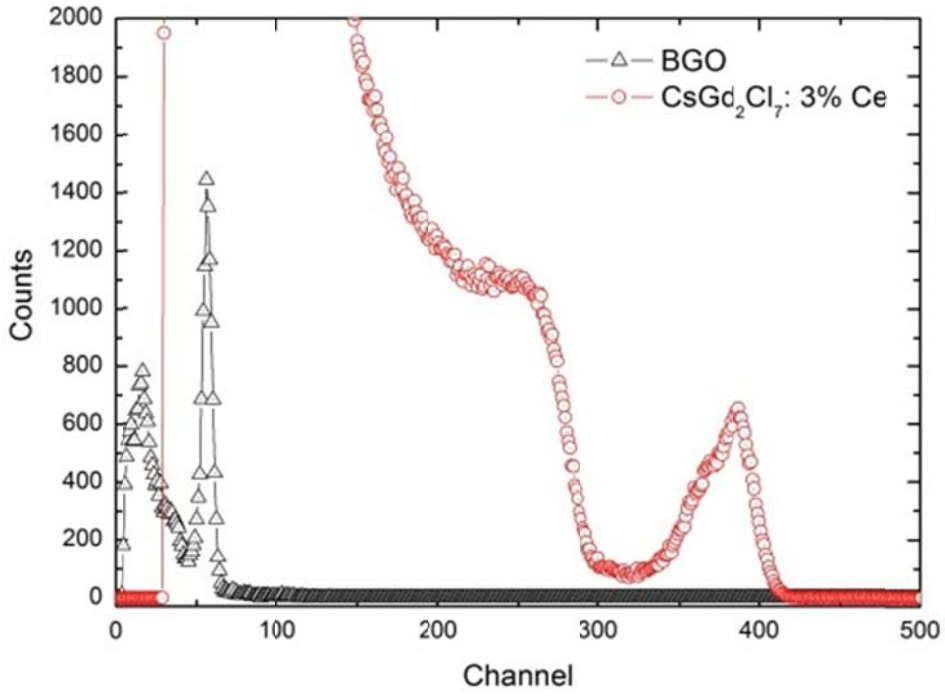

Figure 3.10 Energy spectra of $CsGd_2Cl_7:Ce^{3+}$ single crystals compared with a BGO reference crystal

In addition to gamma ray detection, $CsGd_2Cl_7:Ce^{3+}$ can operate as a thermal neutron detector due to the presence of Gd as one of the constituents. Two isotopes of Gd, ^{157}Gd and ^{155}Gd, have very high thermal neutron absorption cross-sections. About 80% of the captures in Gd with natural isotopic abundance occur in ^{157}Gd which is 15.65% abundant and has a thermal neutron cross section of 255,000 barns. About 18% of the neutron captures occur in ^{155}Gd which is 14.8% abundant and has a capture cross section of 61,000 barns [48]. The interaction of thermal neutrons with Gd results in two characteristic energy peaks, 33 keV and 77 keV. The peaks are from $2^+ \rightarrow 0^+$ transitions in ^{156}Gd and ^{158}Gd, which produce characteristic X-rays of 44 keV and conversion electrons. Due to the short range of the conversion electron, it does not escape the crystal, which by itself gives rise to the characteristic peak at 33 keV. The 44 keV X-ray has 50% chance of escaping the crystal and 50% chance of being absorbed [48]. When the X-ray is absorbed, together with the conversion electron, it gives rise to the energy peak at 77 keV.

Thermal neutron response was studied with a ^{252}Cf source. Neutrons from the source were moderated by 2” thick High Density Polyethylene (HDPE) between the ^{252}Cf source and the sample. The ^{252}Cf source was enclosed in a Pb container with 1/2” wall thickness and the sample was enclosed in a 1/8” thick Pb cylinder in order to shield the sample from gamma rays from the source. The sample was immersed in paraffin oil and coupled directly to a Philips 2202B photomultiplier tube. A light collection cap with reflective coating was used to

enhance the light collection efficiency. The gamma-ray background from the ^{252}Cf source was measured by shielding the sample from thermal neutrons with a 1/8" thick Cd cylinder in place of the Pb shielding. Figure 3.11 shows a schematic diagram of the experimental arrangement used to measure the thermal neutron response.

Figure 3.12 shows the energy spectrum of $CsGd_2Cl_7:Ce^{3+}$ excited by thermal neutrons from the ^{252}Cf source. The γ-ray and fast neutron background was measured by replacing the 1/8" Pb cylinder in Figure 1 with a Cd cylinder of the same thickness, which absorbs the thermal neutrons. The acquisition time for both measurements was kept the same. The γ-ray background was then subtracted from the overall energy spectrum to obtain the net thermal neutron response. As we see in Figure 7, we confirmed that the two clearly resolved energy peaks around 580 ch and 1330 ch are the two characteristic peaks of thermal neutron capture by Gd.

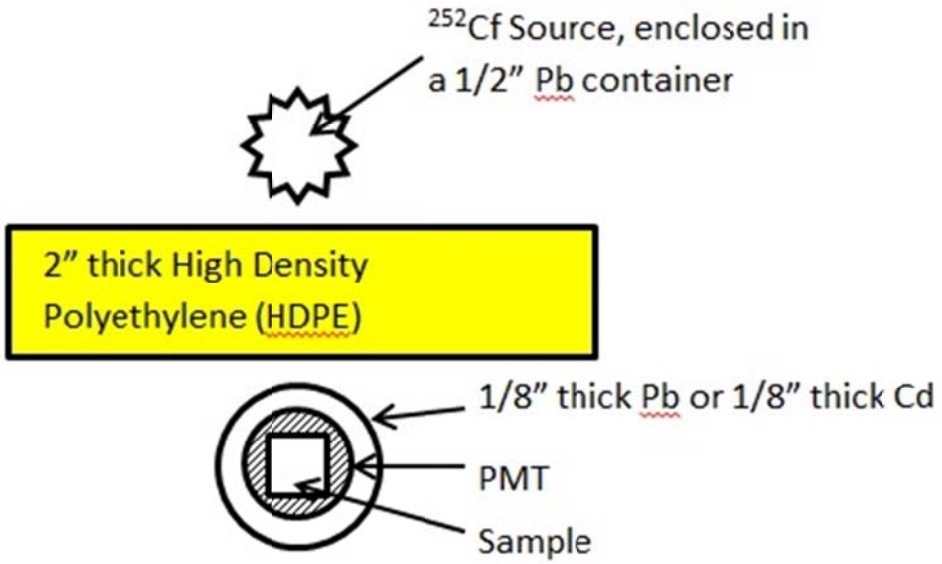

Figure 3.11 Schematic diagram of the experimental arrangement for measuring the neutron response of $CsGd_2Cl_7:Ce^{3+}$

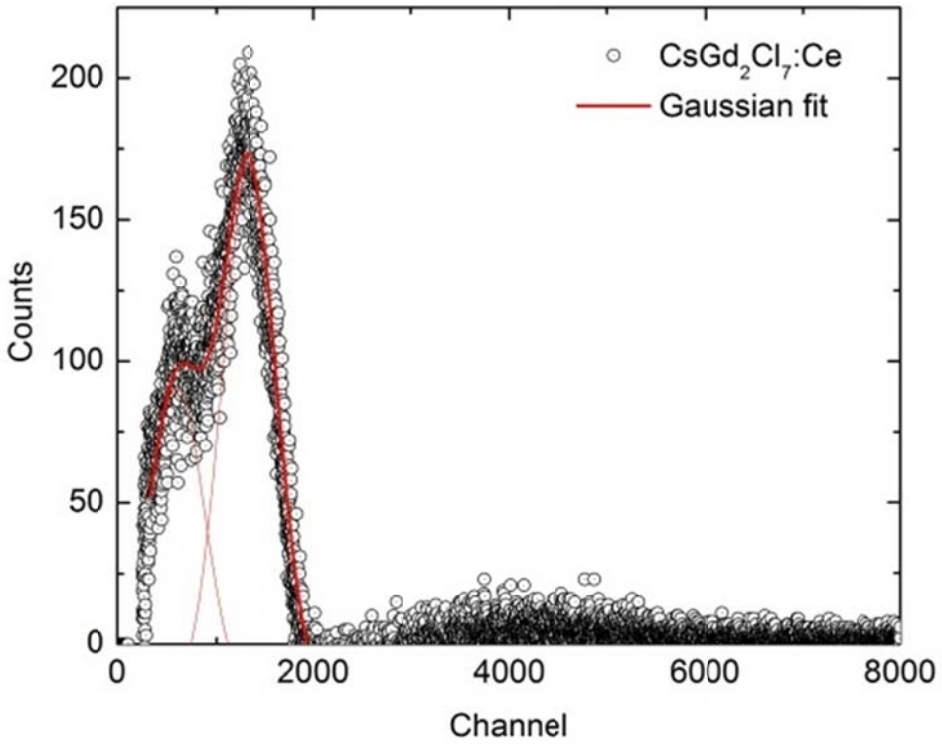

Figure 3.12 Energy spectrum of $CsGd_2Cl_7:Ce^{3+}$ excited by thermal neutrons, showing 33 and 77 keV peaks, characteristic for thermal neutron interaction with Gd; γ-ray background from the ^{252}Cs source has been subtracted from the spectrum

3.3.2. Summary

$CsGd_2Cl_7:Ce^{3+}$ exhibits good scintillation properties under γ ray excitation such as high light output and fast principal scintillation decay. Table 3.2 summarizes some of the most important physical and scintillation properties of $CsGd_2Cl_7:Ce^{3+}$. The detection of thermal neutrons was also confirmed. $CsGd_2Cl_7:Ce^{3+}$ crystals have a layered structure with weak cleavage planes, and it is likely that a refined crystal growth technique in which an oriented seed is used to control crystallization in a preferred direction will be beneficial for crystal quality and scintillation performance.

Table 3.2 Physical and scintillation properties of $CsGd_2Cl_7:Ce^{3+}$ compared with $NaI:Tl^+$

Composition	***Density, g/cm^3***	***Principal decay, ns***	***LO, ph/MeV***	***RL max, nm***
$CsGd_2Cl_7:Ce^{3+}$ 3%	3.84	60	38,000	400
$NaI:Tl^+$	3.67	230	38,000	415 [49]

3.4. Single crystal $CsSrI_3:Eu^{2+}$ for high energy resolution γ spectroscopy

The crystal structure of $CsSrI_3$ was first reported by Schilling et al[50]. $CsSrI_3$ has an orthorhombic structure with space group *Cmcm*. The density of $CsSrI_3$ is 4.25 g/cm^3. The phase diagram of the CsI – SrI_2 binary system is not available. However, $CsEuI_3$ was first synthesized via solid state reaction [51] and phase diagram study shows that $CsEuI_3$ is a congruently melting compound with melting point of 642℃ [52]. The Eu^{2+} and Sr^{2+} have same valence states and fairly similar ionic radii (1.09 Å for Eu^{2+}; 1.12 Å for Sr^{2+}) [53]. Presumably, Sr^{2+} substitutes for Eu^{2+} in the matrix of $CsEuI_3$ without disturbing crystal structure. There is high chance that $CsSrI_3$ would be a congruently melting composition as $CsEuI_3$, which makes this composition a good candidate for single crystal growth from the melt.

$CsSrI_3:Eu^{2+}$ crystals with various Eu^{2+} concentrations and sizes were successfully grown to explore the optical properties, scintillation properties and potential for bulk crystal growth of this promising scintillation crystal.

3.4.1. Synthesis

3.4.1.1. Optimization of Eu^{2+} concentration

Prior to single crystal growth, the optimal Eu^{2+} concentration was experimentally determined by melt synthesizing $CsSrI_3$ with 1%, 5%, 7.5% and 10% Eu^{2+} concentrations. The measured pulse height spectra of four CsSrI3 polycrystalline samples are shown in Figure 3.13. The measurement system was tuned so that the photopeak of a BGO

reference crystal was at channel 100. $CsSrI_3$ doped with 7.5% appeared to have the highest scintillation light output, which was about 5 times that of a BGO. Since crystal growth technique was not applied, higher scintillation light output could be expected on single crystal $CsSrI_3:Eu^{2+}$.

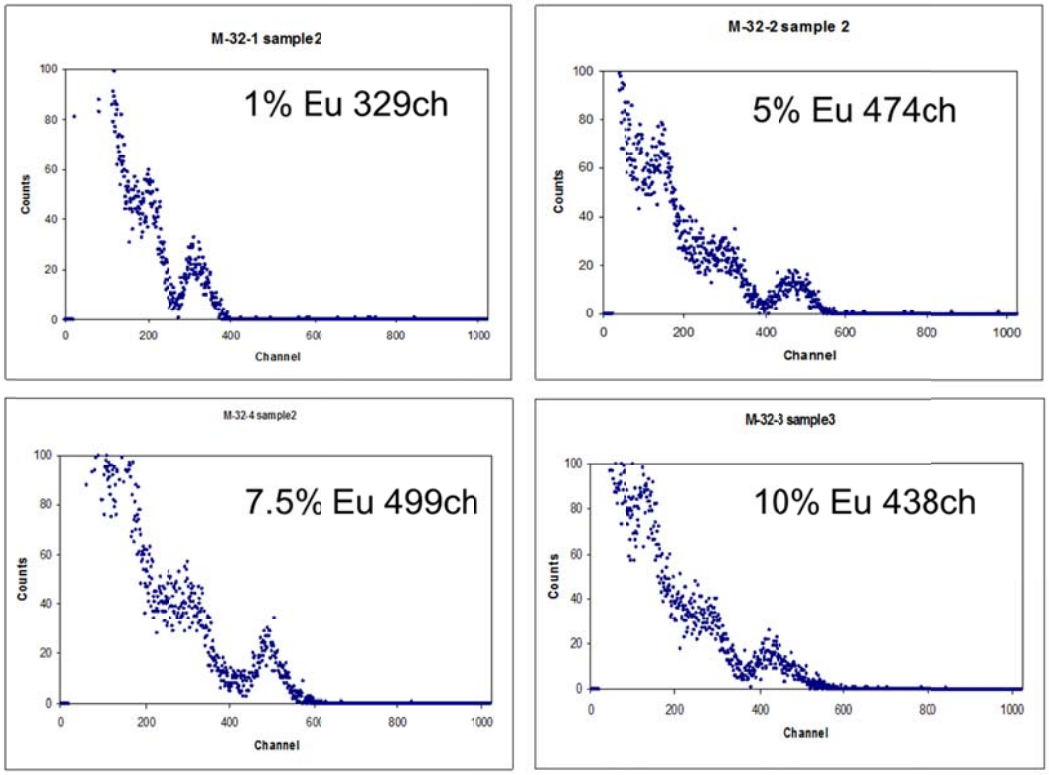

Figure 3.13 Pulse height spectra of melt synthesized $CsSrI_3$ doped with 1%, 5%, 7.5% and 10% Eu^{2+} for optimal Eu^{2+} concentration determination

Based on the melt synthesis experiments, the optimal Eu^{2+} doping concentration was estimated to be 7.5 atomic %, with respect to Sr^{2+}. The Eu^{2+} presumably substitutes for Sr^{2+} in the matrix of $CsSrI_3$, because these two cations have same valence states and fairly similar ionic radii (1.09 Å for Eu^{2+}; 1.12 Å for Sr^{2+}) [53]. For stoichiometry calculation, the atomic percent of Sr^{2+} was adjusted according to the atomic percent of doped Eu^{2+}. Three crystals of ½" diameter were grown to investigate the effect of Eu^{2+} doping concentration on the scintillation properties of these materials. Then, after modification of crystal growth apparatuses, a bulk crystal of 1" diameter was successfully grown by Bridgman method. Table 3.3 lists the single crystals which have been grown in this research.

Table 3.3 List of single crystal $CsSrI_3$:Eu

Host material	***Eu concentration***	***Diameter, inch***
$CsSrI_3$	1 at %	½
$CsSrI_3$	7 at %	½
$CsSrI_3$	8 at %	½
$CsSrI_3$	7 at %	1

3.4.1.2. Thermal analysis (Differential Scanning Calorimetry)

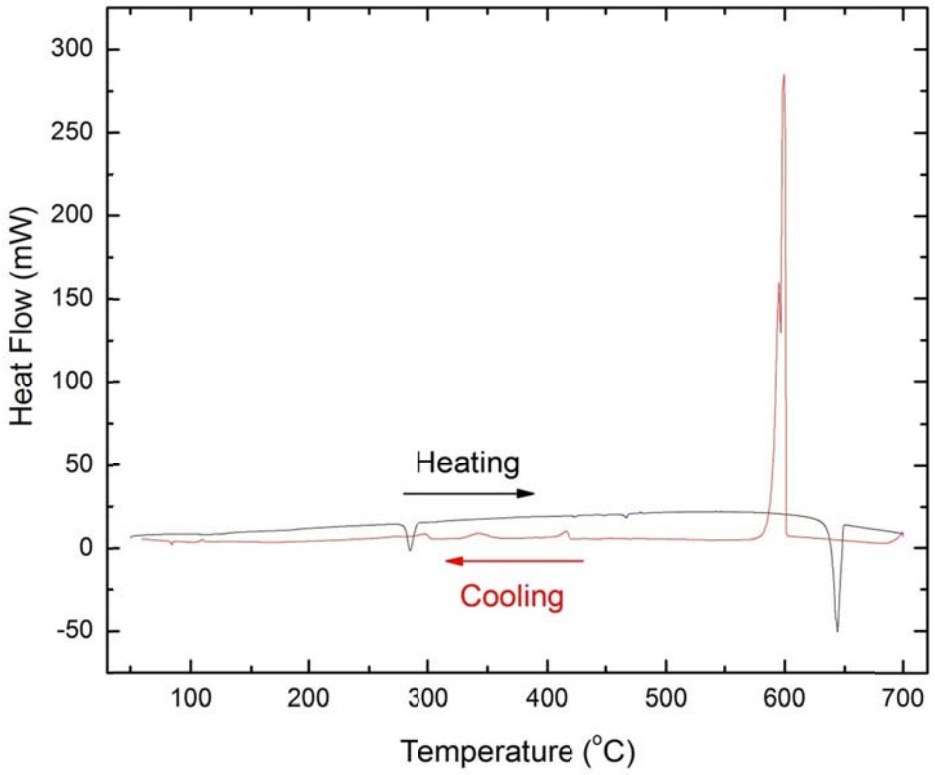

Figure 3.14 Differential scanning calorimetry (DSC) curve of $CsSrI_3$: 7% Eu

First of all, differential scanning calorimetry (DSC) was performed on a $CsSrI_3$: 7% Eu sample to determine the exact melting point of this compound. The weight of the particular sample was 48.1 mg. The sample was first ramped up to 700 ℃ at 10 ℃/min then cooled down to room temperature at 80 ℃/min. Measurement was done in an Argon purged chamber to prevent the sample oxidization.

Figure 3.14 shows the DSC curve for $CsSrI_3$: 7%Eu. The *x*-axis is temperature and the *y*-axis is the measured heat flow. The melting point of

$CsSrI_3$:Eu was determined to be 645 ± 1.5 ℃. Supercooling was observed for this material, which suggested that a slow growth rate was preferred to minimize the negative impact from the supercooling.

3.4.1.3. Single crystal growth

3.4.1.3.1. CsSrI3:1%Eu, ½" diameter single crystal

A stoichiometric mixture of at least 99.99% pure, anhydrous, CsI, SrI_2 and EuI_2 raw material beads from Sigma Aldrich were prepared in a N_2 purged MBraun Unilab glovebox. Table 3.4 lists the starting materials used for this crystal growth. Materials were then loaded to a ½" quartz ampoule for initial synthesis (Figure 3.15). The quartz ampoule was cleaned with hydrofluoric acid and pre-baked before using. The ampoule was evacuated to a vacuum of 1×10^{-6} mbar. A clamshell furnace was used to heat the ampoule at 200 ℃ for 14 hours in order to remove the residual moisture. The ampoule was then sealed and transferred to a Lindberg 1500℃ box furnace for synthesis. The ampoule was heated at 700℃ for 12 hours to ensure the completion of reaction and materials homogeneity. $CsSr_{0.99}Eu_{0.01}I_3$ was synthesized via $CsI + 0.99SrI_2 + 0.01EuI_2 \rightarrow CsSr_{0.99}Eu_{0.01}I_3$ reaction. After initial synthesis, the $CsSrI_3$:1%Eu ingot was polycrystalline and colorless. Grain size varied from 1-3 mm. The synthesis ampoule was then opened in the glovebox. The material ingot was c and loaded to a crystal growth ampoule. The ampoule was sealed under 1×10^{-6} mbar vacuum before crystal growth. Melt filtration was not applied in this crystal.

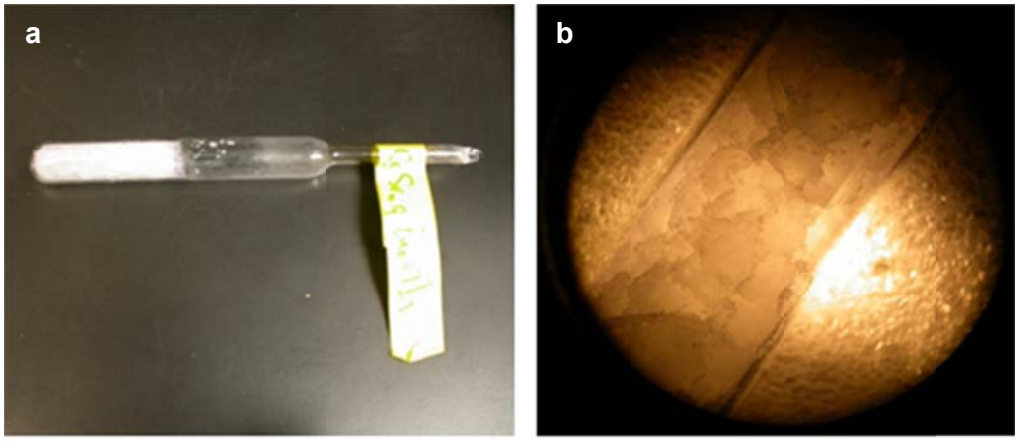

Figure 3.15 $CsSrI_3$:1%Eu ingot after initial synthesis

Table 3.4 Starting materials for ½" single crystal growth of $CsSrI_3$:1%Eu

Compound	***Mass (g)***
CsI_2	12.96
SrI_2	17.04
EuI_2	0.203
$CsSrI_3$:Eu	30.00

Single crystal of $CsSrI_3$:1%Eu was grown by the Bridgman method in a Mellen 24-zone Sunfire Electro-Dynamic Gradient (EDG) furnace. Details about the crystal growth techniques were discussed in Chapter II. The hot zone temperature was set at 700 ℃ and the cold zone temperature was set at 475 ℃. The transition zone between the hot and the cold zone had a width of 2". The crystal growth ampoule translated through the thermal gradient at a constant speed of 1.5 mm/h. At the end of growth, the crystal was cooled to room

temperature at a constant rate of 10℃/h.

Figure 3.16 shows the results of Bridgman single crystal growth of $CsSrI_3$:1%Eu. A zigzag shaped capillary tube was used for seeding (Figure 3.16a). Because melt filtration was not applied in this particular crystal growth, a contaminated layer (presumably by carbon) was observed at the surface of the melt. About 5 mm thick of material from the melt surface was cut and discarded. The grown crystal was 2" long with a relatively rough surface. The crystal only showed one crack which was about 45^o to the center axis of the ampoule. This should be initiated during the cooling process. High crystal quality was expected with slower cooling rate. The rest of the crystal was crack-free (Figure 3.16b). The crystal was then cut and hand polished for characterization. Figure 3.16c shows a polished sample slab with 5 mm thickness.

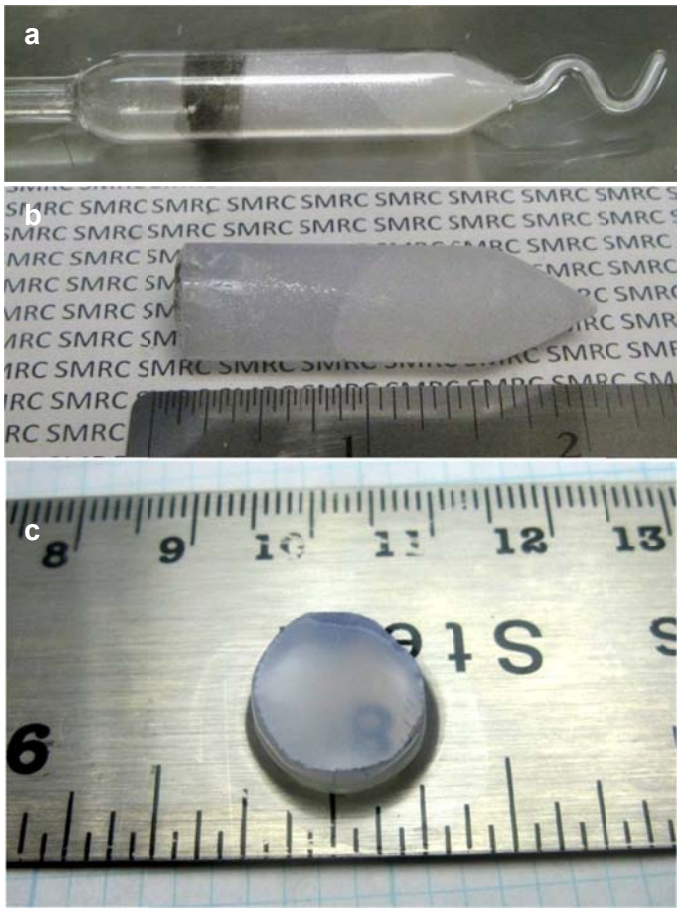

Figure 3.16 ½” diameter Single crystal $CsSrI_3$:1%Eu

3.4.1.3.2. $CsSrI_3$:7%Eu, ½" diameter single crystal

The material preparation procedure for the 1/2" $CsSrI_3$:7%Eu crystal was the same as the procedure for the 1/2" $CsSrI_3$:1%Eu. Table 3.5 lists the starting materials used for this crystal growth.

Table 3.5 Starting materials for ½" single crystal growth of $CsSrI_3$:7%Eu

Compound	***Mass (g)***
CsI_2	12.87
SrI_2	15.73
EuI_2	1.407
$CsSrI_3$:Eu	30.00

As to single crystal growth, a filtration tube was added to the crystal growth ampoule to filter the molten material in order to remove all refractory contaminations. Fig 3a shows the material was filtered by the quartz fritz and flowed into the crystal growth volume. The material ingot was colorless without any visible contaminations. The connecting tube between the melt filtration tube and the crystal growth volume was sealed after filtration was finished.

Bridgman method was used to grow this crystal. The hot zone was set at 680 ℃ and cold zone was set at 500 ℃. Transition zone was 2" wide. The translation speed for the ampoule was 1 mm/hour. In order to minimize thermal

shock to the grown crystal, I set the cooling rate at 8 ℃/hour, which was 20% smaller than the previous crystal.

Crystal growth results were shown in Figure 3.17. The crystal was colorless without any visible colored contamination. The surface of the crystal was smooth. The crystal was transparent with slight cloudiness, which might be due to low concentration contamination or bubbles in the crystal.

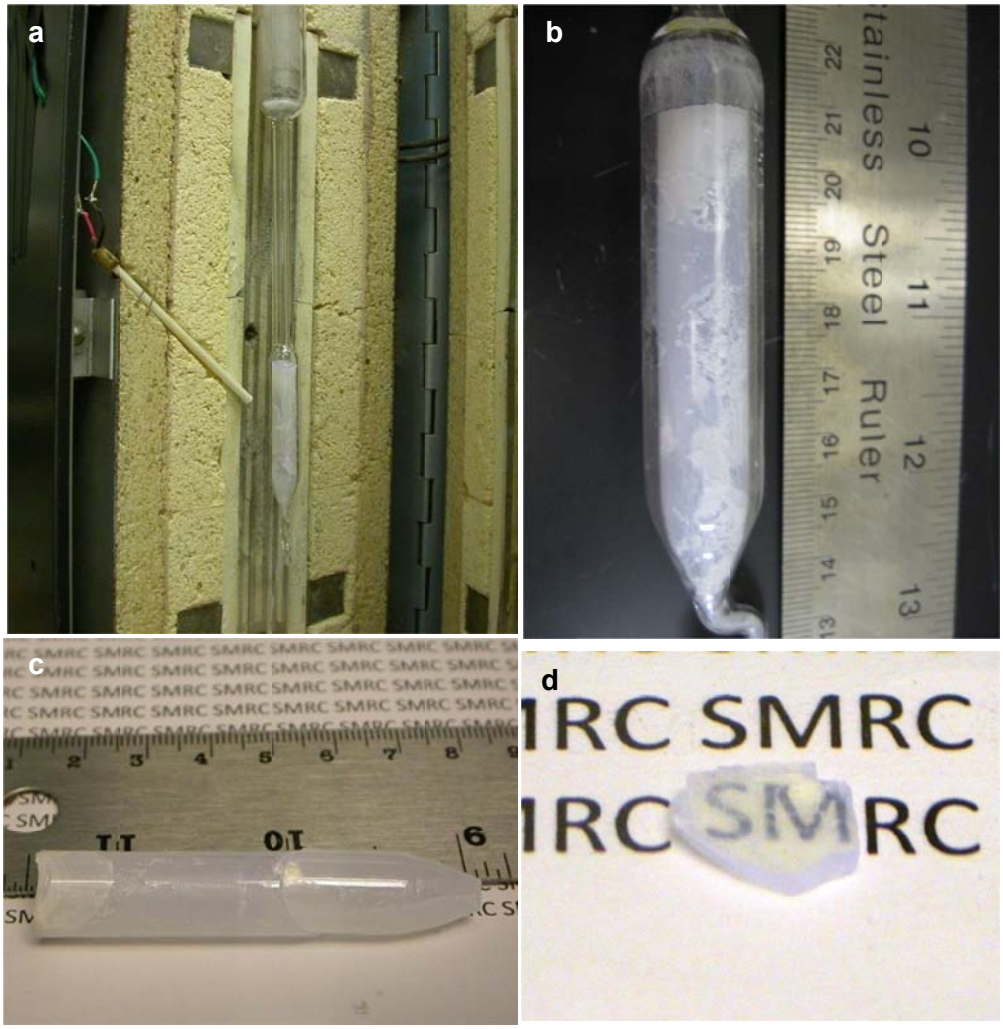

Figure 3.17 $CsSrI_3$:7%Eu single crystal (a) after melt filtration; (b) in the ampoule; (c) out of the ampoule; (d) a polished sample

3.4.1.3.3. $CsSrI_3$:8%Eu, ½" diameter single crystal

The ampoule preparation procedure for the 1/2" $CsSrI_3$:7%Eu crystal was the same as what was discussed in 3.4.1.1. Table 3.6 lists the starting materials used for this crystal growth.

Table 3.6 Starting materials for ½" single crystal growth of $CsSrI_3$:8%Eu

Compound	***Mass (g)***
CsI_2	16.28
SrI_2	19.68
EuI_2	2.034
$CsSrI_3$:Eu	38.00

Melt filtration tube was not used in this crystal growth practice. Bridgman method was used to grow this crystal. The hot zone was set at 700 ℃ and cold zone was set at 475 ℃. Transition zone was 2" wide. The translation speed for the ampoule was 1.5 mm/hour. In order to minimize thermal shock to the grown crystal, I set the cooling rate at 10 ℃/hour.

Crystal growth results were shown in Figure 3.18. The crystal was free of cracks (Figure 3.18a and 3.18b). Since the melt filtration was not used, a layer of black contaminations were observed at the melt surface. The contaminated layer was cut and discarded. A close-up photo (Figure 3.18b) clearly demonstrated

that the capillary tube successfully insured that only one dominant crystal grain entered crystal bulk. The surface of the crystal was smooth. The crystal was transparent with slight cloudiness. Crystal was cut and polished before characterizations. Figure 3.18e shows a comparison between a $CsSrI_3$:8%Eu crystal sample and a Lu_2SiO_5:Ce under the excitation from 255 nm UV light.

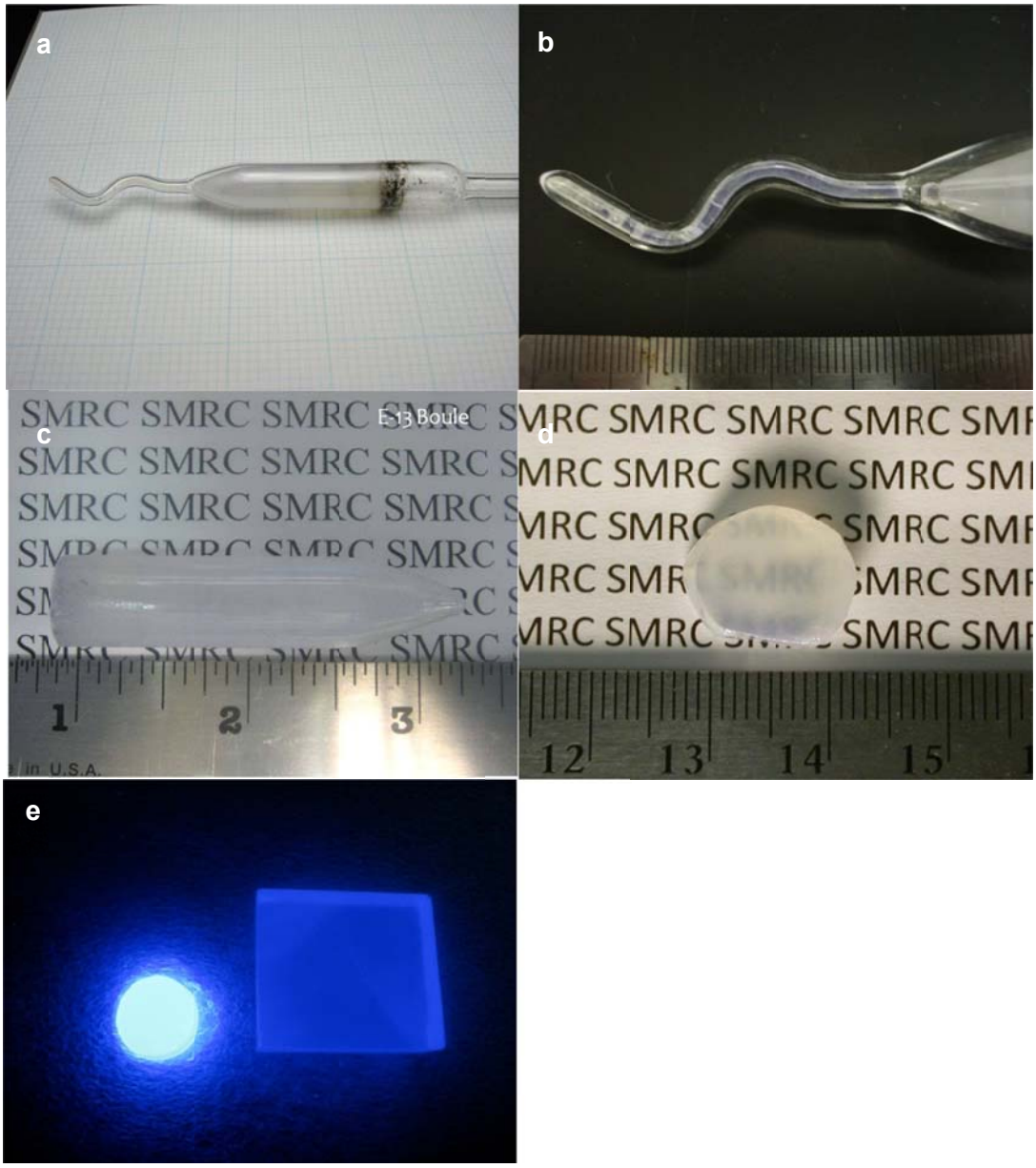

Figure 3.18 $CsSrI_3$:8%Eu ½" diameter single crystal (a) crystal in the ampoule; (b) capillary seeding tube; (c) crystal out of the ampoule; (d) a polished sample; (e) A $CsSrI_3$:8%Eu crystal compared with a Lu_2SiO_5:Ce crystal under the 255 nm UV

3.4.1.3.4. $CsSrI_3$:7%Eu, 1" diameter single crystal

Stoichiometric mixture of 99.99% pure CsI, SrI_2 and EuI_2 beads were prepared in the N_2-purged glovebox. Table 3.7 shows the exact amount of starting materials used for this growth. Starting materials were then loaded into an initial synthesis ampoule. Materials were evacuated to 10^{-6} mBar and heated at 320 ℃ for 12 hours in order to remove residual moisture. Then the initial synthesis ampoule was sealed, heated to 700 ℃ and soaked for 12 hours to ensure that the reaction was fully completed. $CsSrI_3$:7%Eu ingot was colorless and polycrystalline after initial synthesis (Figure 3.19a). Then the ingot was ground and loaded to the crystal growth ampoule for melt filtration and crystal growth.

Table 3.7 Starting materials for 1" single crystal growth of $CsSrI_3$:7%Eu

Compound	***Mass (g)***
CsI_2	30.02
SrI_2	36.69
EuI_2	3.282
$CsSrI_3$:Eu	70.00

Crystal growth ampoules and vacuum station were modified to grow 1” single crystal $CsSrI_3$ doped with 7% Eu. The detailed design of the crystal growth ampoule was shown in Figure 2.2. An additional sealing tube was inserted to facilitate ampoule sealing, which prevented contaminations from materials decomposition under heat of the torch. The loaded crystal growth ampoule was evacuated to 10^{-6} mBar vacuum and dried again at 320 ℃ for 12 hours by the clamshell furnace (Figure 3.19b and 3.19c). The clamshell furnace was later ramped up to 700 ℃. After all molten material passed through the quartz fritz and entered the crystal growth volume, the crystal growth ampoule was sealed and ready for crystal growth.

Bridgman method was used to grow this crystal. The hot zone was set at 680 ℃ and cold zone was set at 500 ℃. Transition zone was 2” wide. Since this crystal had by far the largest diameter, a slow growth rate was favorable in order to stabilize the growth. A slow cooling rate would help to eliminate thermal induced cracks, because it would be more difficult for the heat from the core of the crystal to be transmitted outside. The translation speed for the ampoule (growth rate) was set at 0.75 mm/hour. The cooling rate was 8 ℃/hour.

Crystal growth results were shown in Figure 3.19. A 1” diameter, 2” long and crack-free $CsSrI_3$:7%Eu crystal was successfully grown. The crystal was colorless and translucent. A polished crystal slab with 3 mm thickness was shown in Figure 3.19g.

The growth of 1” diameter $CsSrI_3$:7%Eu single crystal successfully demonstrated that large diameter crystal growth of this promising scintillation material was feasible and relatively easy compared to other high light yield crystals like $LaBr_3$:Ce [54, 55]. An oriented seed crystal was not required.

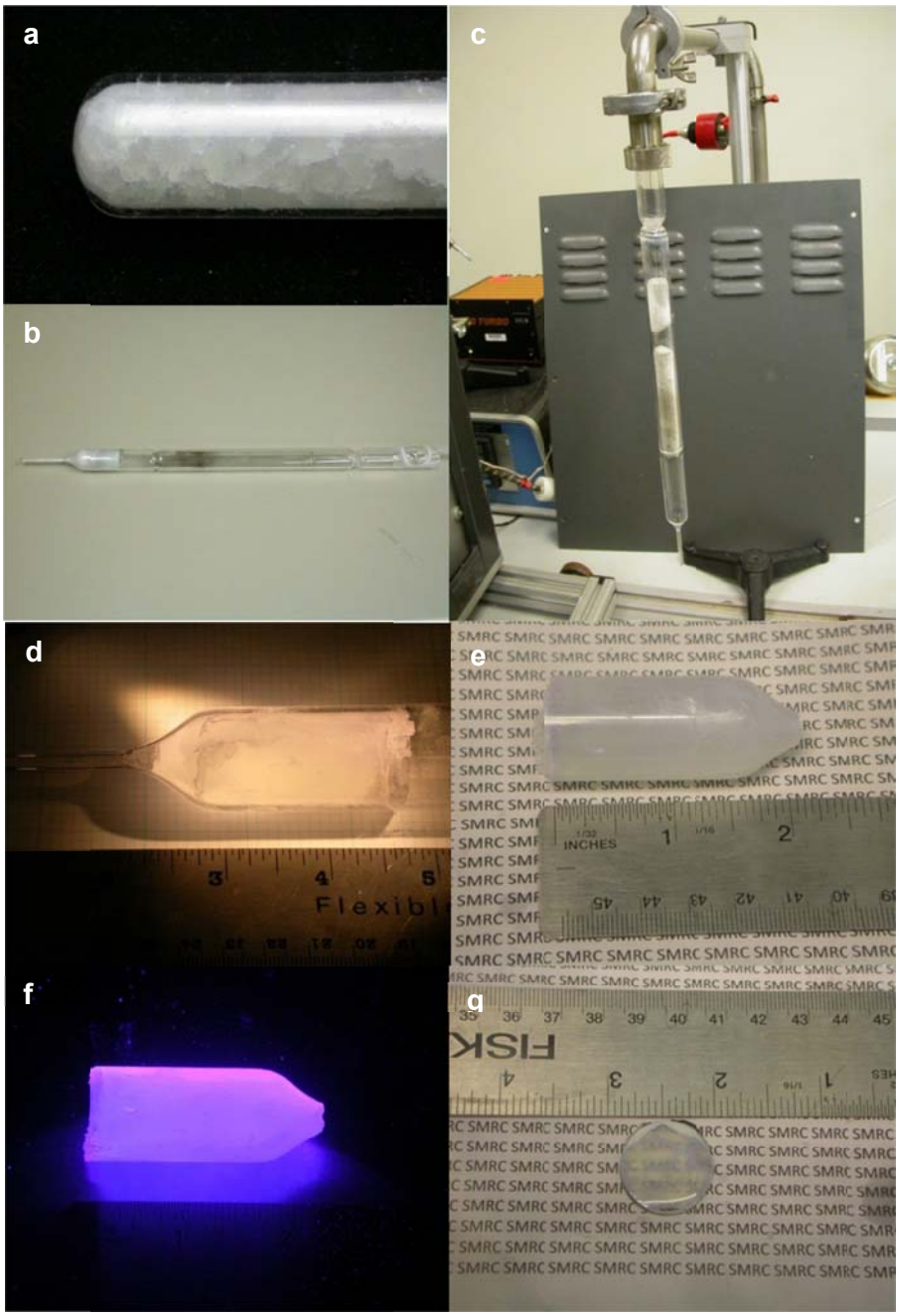

Figure 3.19 CsSrI3:7%Eu 1” diameter single crystal: (a) initial synthesis ampoule (b) prepared crystal growth ampoule; (c) crystal growth ampoule on vacuum station; (d) grown single crystal in the ampoule; (e) grown single crystal out of the ampoule; (f) the crystal boule under the 255 nm UV; (g) a polished sample slab

3.4.2. Characterizations

3.4.2.1. Energy level structure of Eu^{2+} in $CsSrI_3$

X-ray excited luminescence spectra of Eu^{2+} doped $CsSrI_3$ samples are shown in Figure 3.20. Spectra have been offset for easy comparison. The X-ray excited luminescence spectra of $CsSrI_3$ with various Eu^{2+} concentrations are very similar. They show a single emission peak at 450-455 nm with FWHM = ~40 nm. Since no additional emission peak was observed, this single emission peak can be solely attributed to the characteristic emission of Eu^{2+} $4f^6 5d$ -$4f^7$ transition. Eu^{2+} has the $4f^7$ configuration in the ground state and $4f^6 5d^1$ configuration in the excited state.

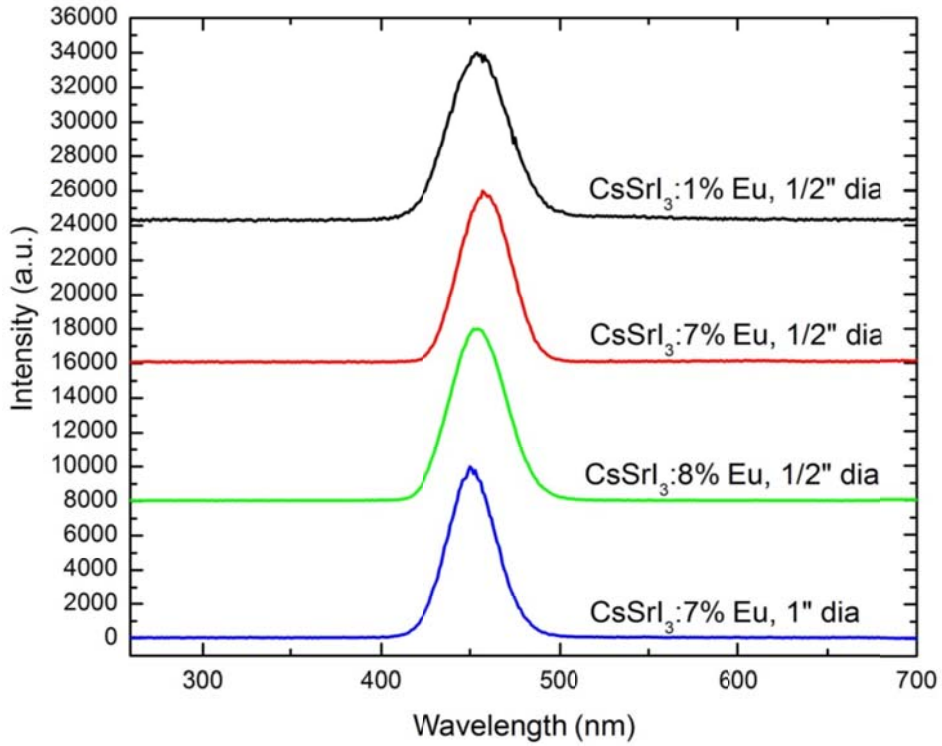

Figure 3.20 X-ray (35 keV 0.1 mA) excited luminescence spectra of $CsSrI_3$ doped with 1%, 7%, and 8% Eu^{2+}

Figure 3.21 shows the photoluminescence excitation and emission spectra of Eu^{2+} doped $CsSrI_3$ samples. The excitation spectra of these crystals are very similar. They all exhibit broad overlapping excitation bands from 260 nm to 440 nm. These overlapping excitation bands were also observed in Eu^{2+} activated SrI_2:Eu^{2+} [56], BaI_2:Eu^{2+} [56], MgI_2:Eu^{2+} [56], $KSrI_3$ [56], Ba_2CsI_5:Eu^{2+} [17], BaBrI:Eu^{2+} [18], $BaBr_2$:Eu^{2+} [57], and $KMgF_3$:Eu^{2+} [58]. The emission peaks of Eu^{2+} doped $CsSrI_3$ samples show one single peak ranging from 446 to 460 nm with increasing Eu concentration.

Eu^{2+} has identical electron configuration as Gd^{3+}. Referring to the Gd^{3+} energy

levels on the well-known Dieke diagram, we can see that all $4f^7$ levels of Eu^{2+} are lower than the lowest $4f^65d$ level for a free ion Eu^{2+} [24]. So for a free ion Eu^{2+} or a Eu^{2+} in weak crystal field, both $4f^65d$ -$4f^7$ ($4f^65d$ - $^8S_{7/2}$) and $4f^7$-$4f^7$ (^6P_j – $^8S_{7/2}$) transitions are possible. Since the $4f^7$-$4f^7$ transitions are parity forbidden, the emission peaks for such transitions are usually sharper comparing to the emission peaks of $4f^65d$ -$4f^7$ transitions. $4f^7$-$4f^7$ transitions are observed together with the parity allowed $4f^65d$ -$4f^7$ in crystals like $KMgF_3:Eu^{2+}$ [58] and $SrS:Eu^{2+}$ [59]. In the case of $CsSrI_3:Eu^{2+}$, only one intense single emission peak is observed. This peak can be solely ascribed to the emission from Eu^{2+} $4f^65d$ -$4f^7$ transition. Since additional $4f^7$-$4f^7$ peak is observed, we can speculate that the $4f^65d$ levels of Eu^{2+} in $CsSrI_3$ host splits and the lowest $4f^65d$ level is already lower than the ^6P_j levels in $4f^7$. Thus $4f^7$-$4f^7$ (^6P_j – $^8S_{7/2}$) transitions are not possible. Schematic energy diagram of both free ion Eu^{2+} and Eu^{2+} in $CsSrI_3$ are shown in Figure 3.22. The broad excitation band of $CsSrI_3:Eu^{2+}$ is also due to the large crystal field splitting of the $4f^65d$ levels. The broad excitation band consists of multiple overlapping bands from both $4f^7$-$4f^7$ and $4f^7$ - $4f^65d$ transitions.

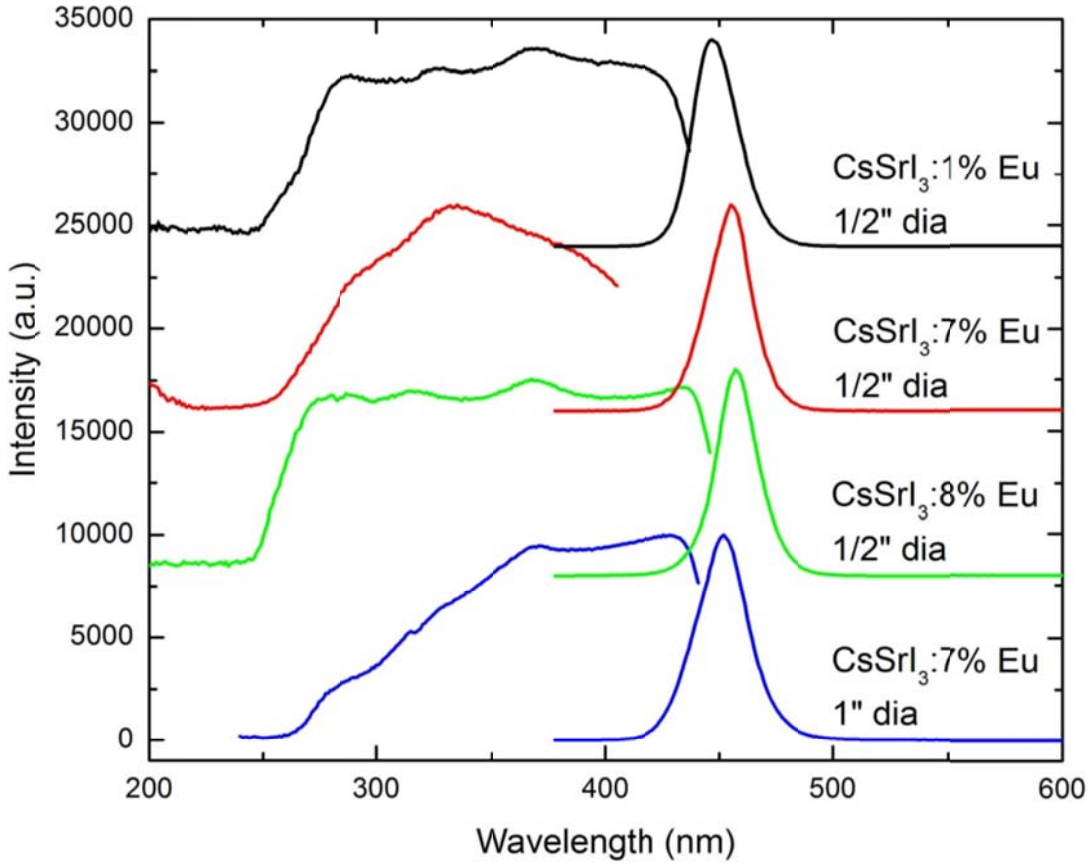

Figure 3.21 Photoluminescence excitation/ emission spectra of Eu doped $CsSrI_3$; Emission wavelengths for excitation spectra are 446, 457, 465 and 451 nm for ½" diameter $CsSrI_3$:1%Eu, ½" diameter $CsSrI_3$:7%Eu, ½" diameter $CsSrI_3$:8%Eu and 1" diameter $CsSrI_3$:7%Eu, respectively. All emission spectra are measured under 368 nm UV excitation.

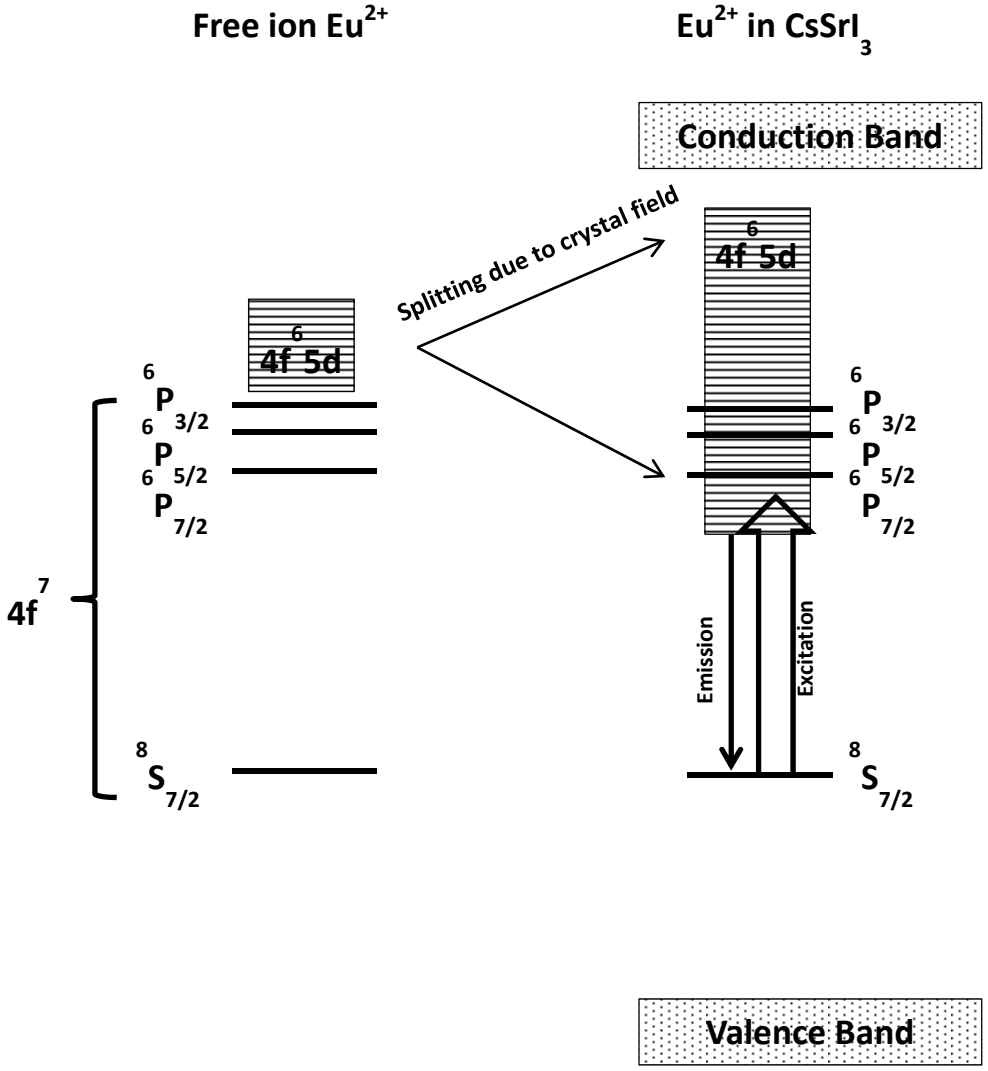

Figure 3.22 Energy level scheme of free ion Eu^{2+} and Eu^{2+} in $CsSrI_3$ crystal host

Moreover, the UV excited emission peak appears to shift towards the longer wavelengths as a function of increasing Eu^{2+} concentration. Comparing the emission and excitation spectra, we see partial overlapping of emission and excitation bands in the range from 425 nm to 450 nm for all crystals. This overlapping suggests these crystals might have self-absorption, which may modify the UV excited emission spectra when the Stokes shift is relatively small.

3.4.2.2. Scintillation light output

As was discussed in the experimental chapter, the integral quantum efficiency has to be calculated prior to the calculation of scintillation light output. The maximum sensitivity of a Hamamatsu R2059 photomultiplier tube is at 420 nm, which is close to the emission peak of $CsSrI_3:Eu^{2+}$. High integral quantum efficiency can be expected if we couple this crystal to a R2059 PMT. The spectral response of a Hamamatsu R2059 photomultiplier tube is shown in Figure 3.23 [60]. The integral quantum efficiencies of $CsSrI_3:Eu^{2+}$ crystals coupled with this PMT can be calculated by the equation below.

$$I.Q.E. = \frac{\int I_{RL}(\lambda) \times Q.E.(\lambda) \times d\lambda}{\int I_{RL}(\lambda) \times d\lambda}$$

where $I_{RL}(\lambda)$represent the relative intensity of X-ray excited luminescence of the sample at wavelength λ. The integral quantum efficiency (I.Q.E.) of $CsSrI_3$ couple with a R2059 PMTis calculated to be 23.0%

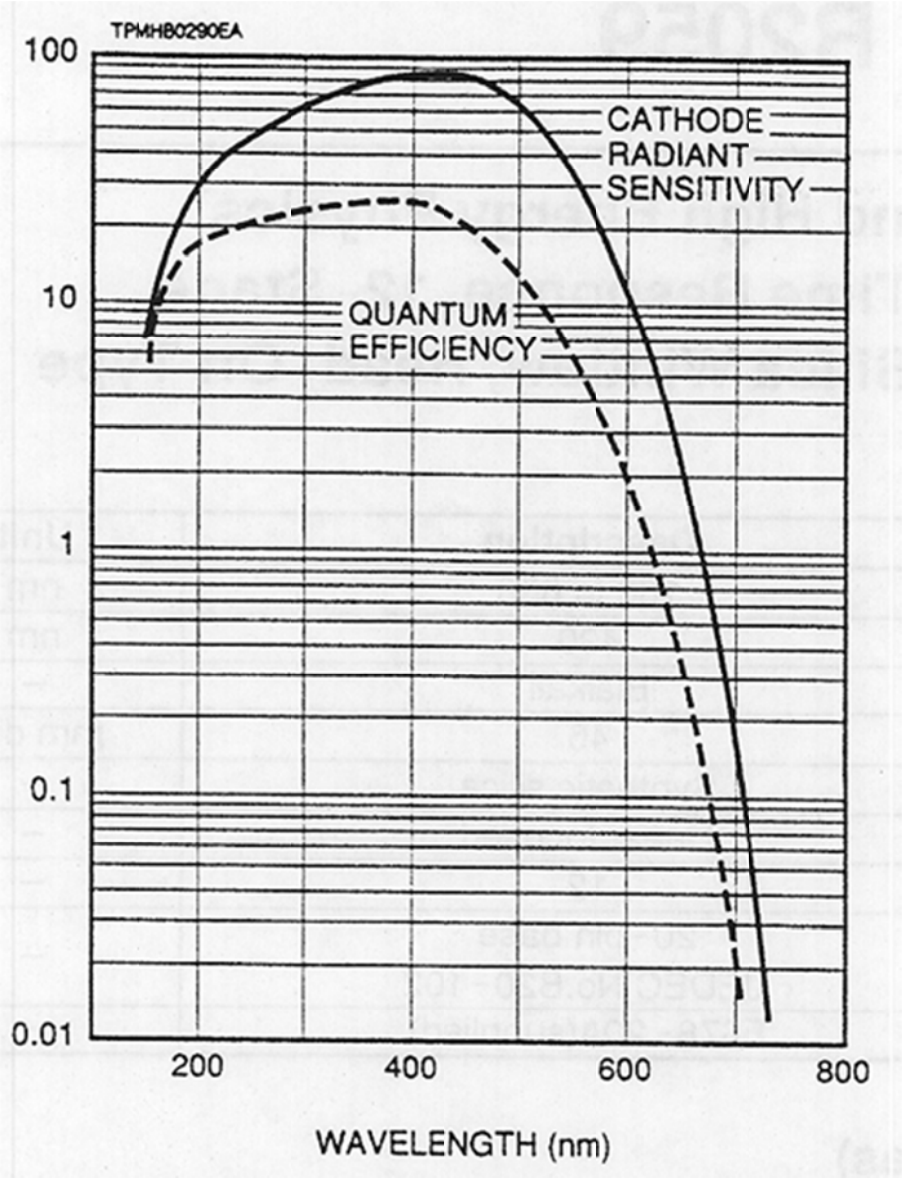

Figure 3.23 Spectral response of a Hamamatsu R2059 photomultiplier tube

The scintillation light outputs of $CsSrI_3:Eu^{2+}$ measured with a 662 keV γ-ray source are listed in Table 3.8. The absolute light outputs were calculated based on the photopeak position in the pulse height spectra and the integral quantum efficiency calculated in the previous section. Both highest absolute light yield and best energy resolution is found for samples from the ½" diameter crystal of $CsSrI_3$ doped with 7% Eu^{2+}. The 1" diameter $CsSrI_3$ crystal doped with same amount of Eu^{2+} shows less scintillation light output and worse energy resolution, which is possibly due to the variation in crystal quality. Because of hygroscopic nature of the $CsSrI_3:Eu^{2+}$ samples, the measured scintillation light output was found to be highly affected by the sample preparation procedure. Improper handling such as accidental air exposure will lower the optical quality of the sample and thus reduce the measured scintillation light output. Figure 3.24 illustrates the pulse height spectra of both $CsSrI_3$:7%Eu^{2+} and $CsSrI_3$:8%Eu^{2+} crystals compared with a BGO reference crystal under ^{137}Cs excitation. The absolute light output of $CsSrI_3$:7%Eu^{2+} is more than 8 times that of BGO and ~ 2 times that of LSO:Ce [61]. The scintillation light output of Eu^{2+} activated $CsSrI_3$ appear to be strongly related to the Eu^{2+} concentrations. This was also observed in Eu^{2+} activated SrI_2 [62, 63].

Table 3.8 Scintillation light output and energy resolution of $CsSrI_3$ doped with various concentrations of Eu^{2+}

Sample	***Light Output (ph/MeV)***	***Energy Resolution @662 keV***
1% Eu, ½" dia.	32,000	9.0%
7% Eu, ½" dia.	73,000	3.9%
8% Eu, ½" dia.	65,000	5.9%
7% Eu, 1" dia.	62,000*	6.0%

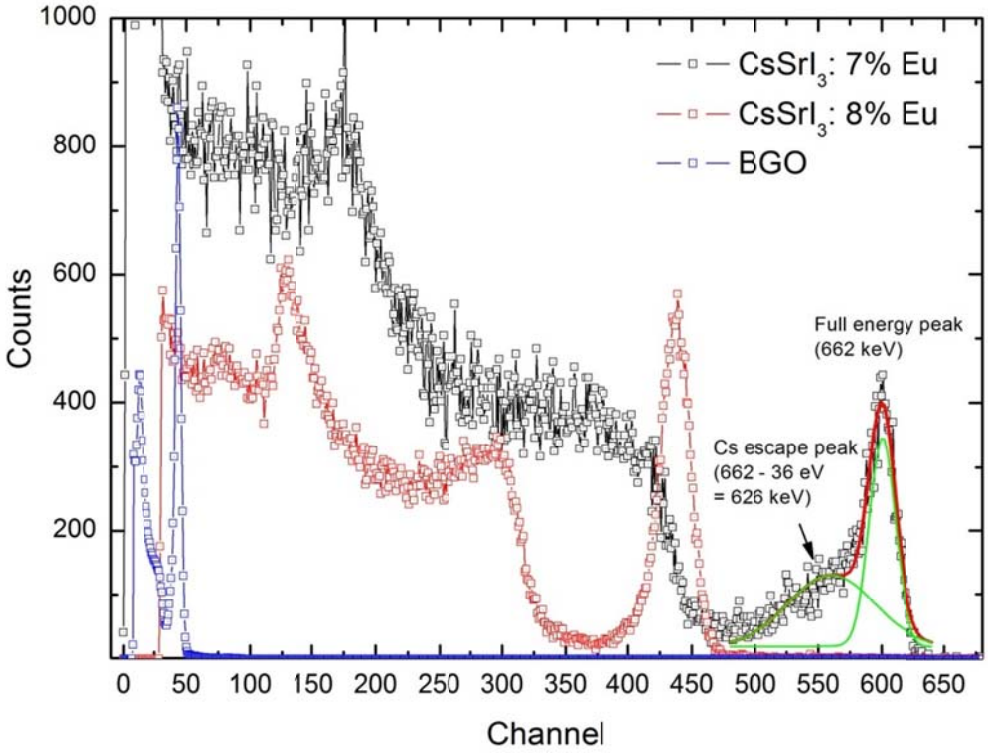

Figure 3.24 Scintillation light output of $CsSrI_3$:7%Eu^{2+}, $CsSrI_3$:8%Eu^{2+} and a BGO reference crystal measured with 662 keV γ-rays from a ^{137}Cs source

3.4.2.3. Scintillation decay time

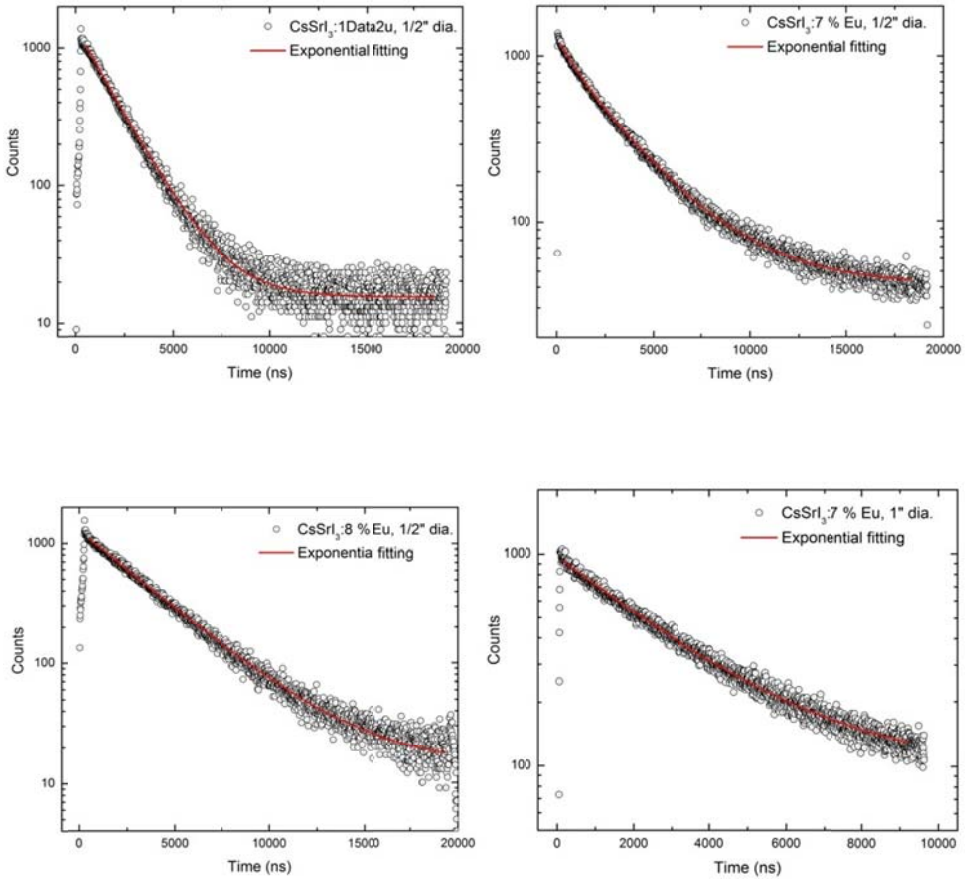

Figure 3.25 Scintillation time profiles of $CsSrI_3$ with various Eu^{2+} concentrations

Scintillation time profiles were shown in Figure 3.25. ^{137}Cs was used as the excitation source. All scintillation time profiles are fitted by single exponential decay functions with constant background. The scintillation decay times range from 1.7 μs to 3.4 μs. The scintillation decay time of $CsSrI_3:Eu^{2+}$ increases with Eu^{2+} concentration. This could be ascribed to self-absorption of the Eu^{2+} emission light. As we see in Figure 3, the excitation and emission spectra show

overlapping in the range from 425 nm to 450 nm. The light emitted by one Eu^{2+} center could be absorbed and re-emitted by another Eu^{2+} center. This would slow down the scintillation process and result in longer scintillation decay time. Light in a crystal with higher Eu^{2+} concentration will have higher probability to be absorbed and re-emitted. Similar effect has been discovered in Eu^{2+} doped SrI_2 crystals [64].

3.4.2.4. Scintillation non-proportionality

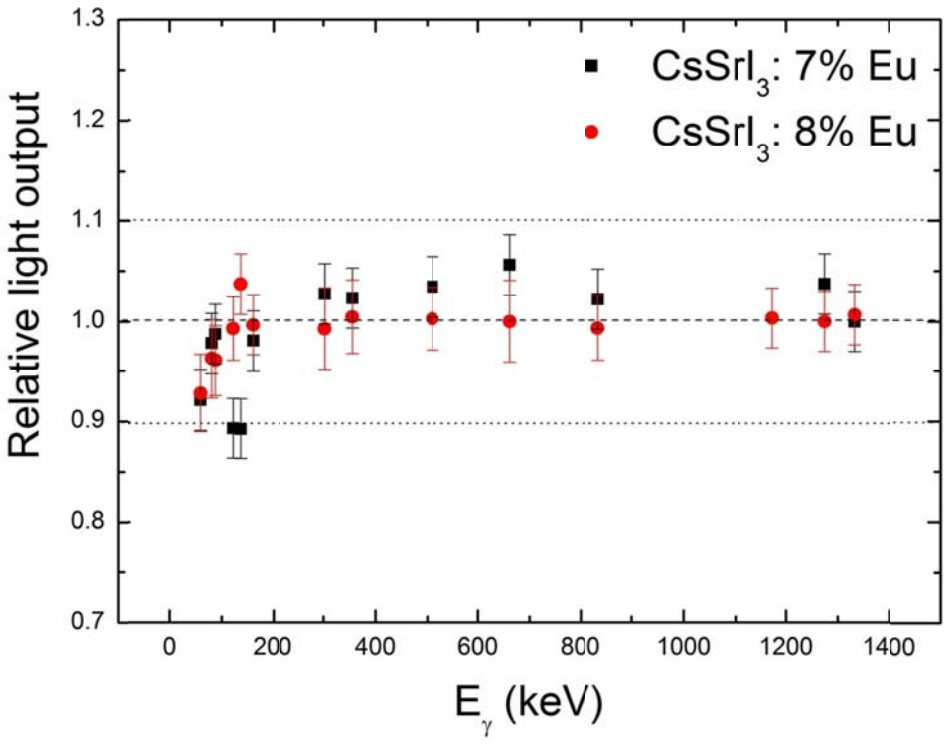

Figure 3.26 Scintillation non-proportionality measurement of $CsSrI_3$:7%Eu and $CsSrI_3$:8%Eu

For non-proportionality measurement, a set of γ-ray sources was used to obtain various γ-ray excitation energies. Scintillation light yields were measured as a function of deposited γ-ray energies, which are shown in Figure 6. The scintillation light yield from an ideal scintillator shall be strictly proportional to the deposited γ-ray energy. For γ-rays with energy higher than 100 keV, the light yield of a $CsSr_{0.92}Eu_{0.08}I_3$ crystal is proportional to the deposited γ-ray energy with less than 5% deviation. The relative light yield decreases when incident γ-rays have energy lower than 100 keV. For γ-rays with ~50 keV energy, the crystal maintains 90~95% of its scintillation light yield per unit energy at 662 keV.

3.4.2.5. Hygroscopicity

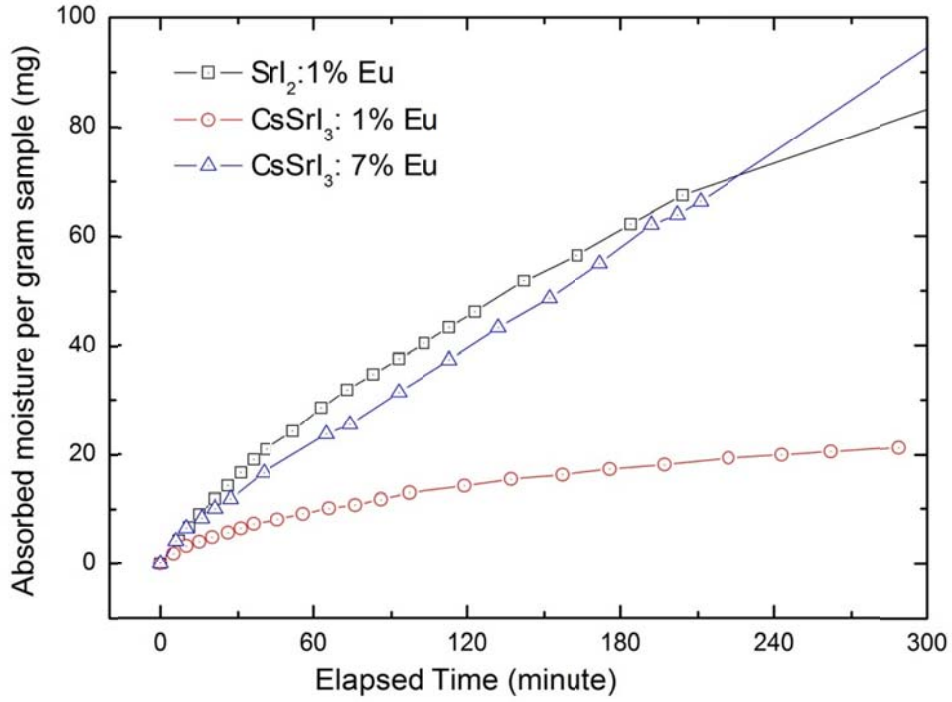

Figure 3.27 Hygroscopicity curves of SrI_2: 1%Eu $CsSrI_3$:1%Eu and $CsSrI_3$:7%Eu; the x-axis is elapsed time and the y-axis is the absorbed moisture per gram sample.

The hygroscopicity (Figure 3.27) of $CsSrI_3:Eu^{2+}$ appeared to be dependent of the Eu% concentration. $CsSrI_3$ with 1% Eu^{2+} was much less hygroscopic than the 7 % Eu^{2+} doped $CsSrI_3$. The rate of moisture absorbing for $CsSrI_3$:1% Eu^{2+} was less than 25% of that of both $CsSrI_3$:7%Eu^{2+} and SrI_3:1%Eu^{2+}. A less hygroscopic crystal would make sample handling and preparation easier.

3.4.3. Scintillation mechanism in $CsSrI_3:Eu^{2+}$

3.4.3.1. Thermal response

It is known that the efficiency of luminescence ions decrease with increasing temperature due to increased probability of non-radiative transitions [65]. Thermal quenching of the luminescence center must be taken into account before we analyze the thermoluminescence characteristics of $CsSrI_3:Eu^{2+}$ [66]. To correct for the thermal quenching effect, UV excited emission spectra were recorded at various temperature. Figure 3.28 illustrates the measured UV excited emission spectra at various temperatures. The sample was maintained at each specific temperature for at least 15 min before measurement was taken. UV light with 367 nm wavelength from a Xenon lamp was used to excite the samples. The Xenon lamp was stabilized for 20 min before the first measurement and maintained on continuously throughout the entire measurement series

As we can see in Figure 3.28, the emission peak intensities decrease monotonically with increasing temperature. The width of emission peak increases with increasing temperature due to thermal broadening [65]. In order to quantitatively analyze the temperature-dependent luminescence efficiency, we plotted the integrated intensities of emission spectra as a function of temperature (Figure 3.29). The luminescence intensity maintains roughly constant for temperature below ~400 K. A minor intensity drop around 300 K was observed, of which the reason was unclear. The emission intensity exhibits major intensity drop for temperature above 400 K. The Mott and Gurney formula was used to fit

the temperature response data [65].

.

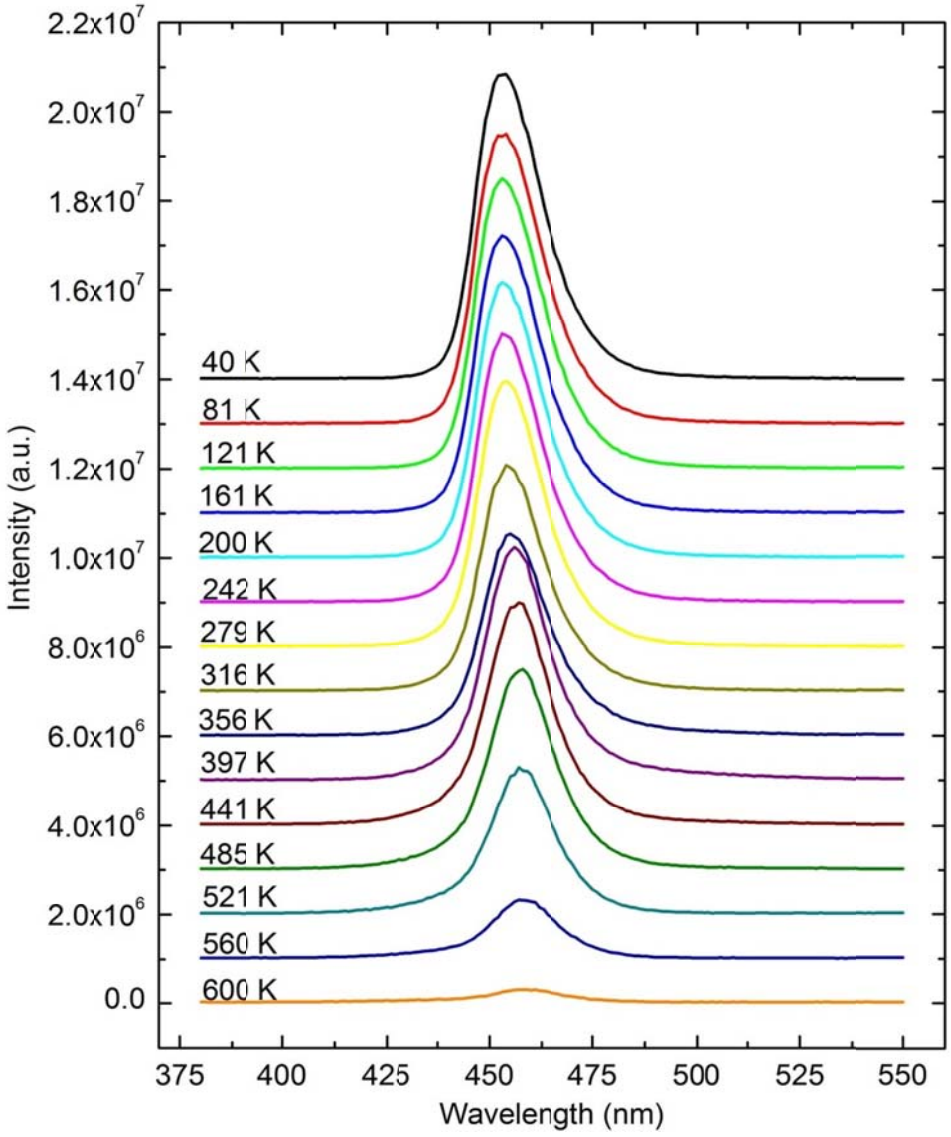

Figure 3.28 UV (367nm) excited emission spectra of $CsSrI_3$:7%Eu at various temperatures; emission spectra have been offset for easy comparison

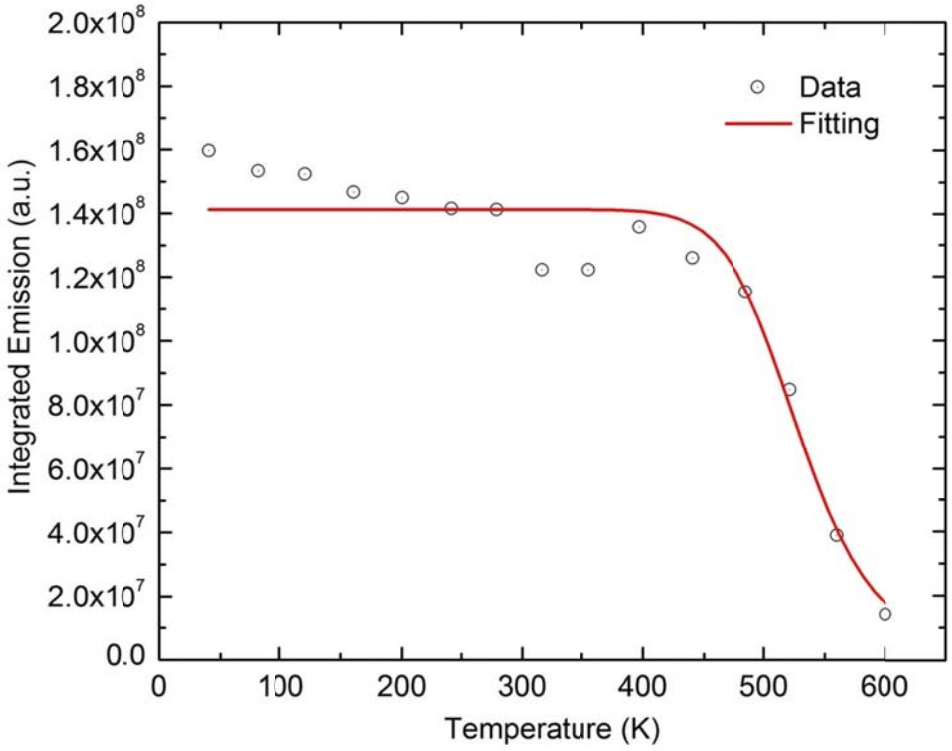

Figure 3.29 Integrated emission of $CsSrI_3$:7%Eu at various temperatures

$$Q(T) = \frac{1}{1 + \frac{k_n}{k_r} exp\left(-\frac{E_a}{\kappa T}\right)}$$

In this equation, k_r is the rate that Eu^{2+} de-excites itself from the excited state to its ground state radiatively, which means a photon is produced. k_n is the rate for Eu^{2+} taking the non-radiative transition. No light is emitted in this case. E_a is the thermal activation energy for non-radiative transition and κ is the Boltzmann constant. The calculated thermal activation energy for Eu^{2+} in the host of $CsSrI_3$ is E_a= 0.75 ± 0.23 eV.

3.4.3.2. Configurational coordinate diagram of Eu^{2+}

Based on the thermal activation energy, the configurational coordinate diagram of the Eu^{2+} center in the host of $CsSrI_3$ can be drawn in Figure 3.30. The Eu^{2+} ground state $^8S_{7/2}$ intercept with the lowest level in the Eu^{2+}'s $4f^6$5d levels. The activation energy is the measure of energy from the bottom of the lowest level in $4f^6$5d to the interception. The rate that an excited electon is de-excited through the interception to the ground the state $^8S_{7/2}$ without any photon emission could be expressed as

$$k_q = k_n exp\left(-\frac{E_a}{\kappa T}\right)$$

k_q is the thermal quenching rate. E_a= 0.75 eV

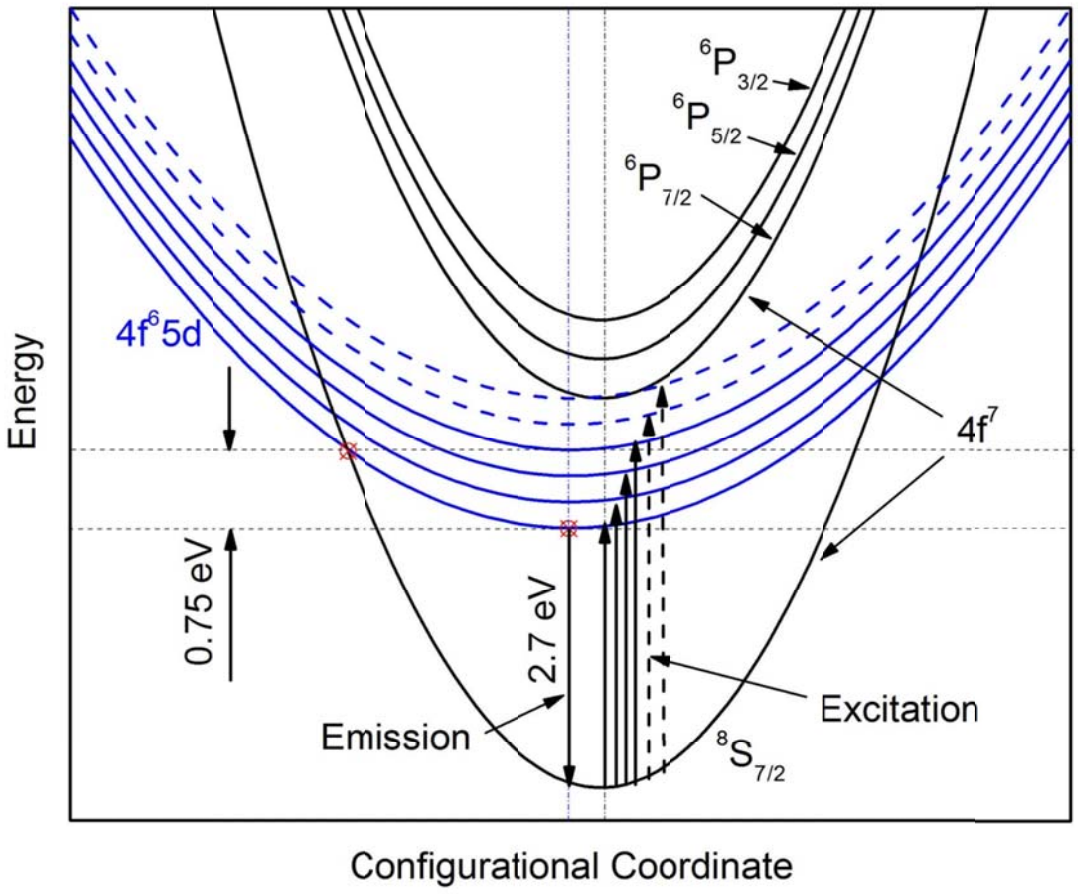

Figure 3.30 Configurational coordinate diagram of Eu^{2+} in $CsSrI_3$

3.4.3.3. Thermoluminescence

Figure 3.31 shows the thermoluminescence glow curve of $CsSrI_3$: 7% Eu^{2+}. The thermoluminescence curve has been corrected for the thermal quenching of Eu^{2+} luminescence based on the above discussed Mott and Gurney formula. The curve is also normalized to the steady state luminescence (SSL) of the sample which refers to the emission intensity under continuous X-rays during initial irradiation. Unity on the y scale is the steady state luminescence intensity of $CsSrI_3$: 7% Eu^{2+} measured under the irradiation of X-rays (35 keV, 0.1 mA) at 26 K.

Multiple thermoluminescence glow peaks are observed in a wide temperature range from 50 K to 350 K. Two thermoluminescence peaks at 173 and 180 K dominate the thermoluminescence glow curve.

The first order kinetic model introduced by Randall and Wilkins was applied to fit each individual thermoluminescence glow peak [67]. This model assumes that there is no re-trapping of charge carriers. The glow peaks in the thermoluminescence curve result from electrons or holes which are only trapped once before they hop to a luminescence center. A single trap is described by two parameters: the trap depth (*E*) and the frequency factor (*s*). The model is expressed by the equation below [67].

$$I(T-\Delta T) = n_0 s exp\left(-\frac{E}{\kappa T}\right) exp\left[-\left(\frac{s}{\beta}\right)\int_{T1}^{T2} exp\left(-\frac{E}{\kappa T'}dT'\right)\right]$$

ΔT is the thermal lag between the sample and the heating element (ΔT = 2~3 K for our experiments). β is the constant heating rate (0.15 K/s for our experiments), and n_0 is the initial concentration of filled traps. In addition, the trap life time (τ) at room temperature (T = 298 K) can be simply derived from the Arrhenius equation.

$$\tau = \frac{1}{s} exp\left(\frac{E}{\kappa T}\right)$$

Trap parameters calculated from curve fitting are listed in Table 3.9. T_{max} is the peak temperature of the thermoluminescence glow peak. n_0 is in the same arbitrary units as thermoluminescence intensity and *s* in sec^{-1}.

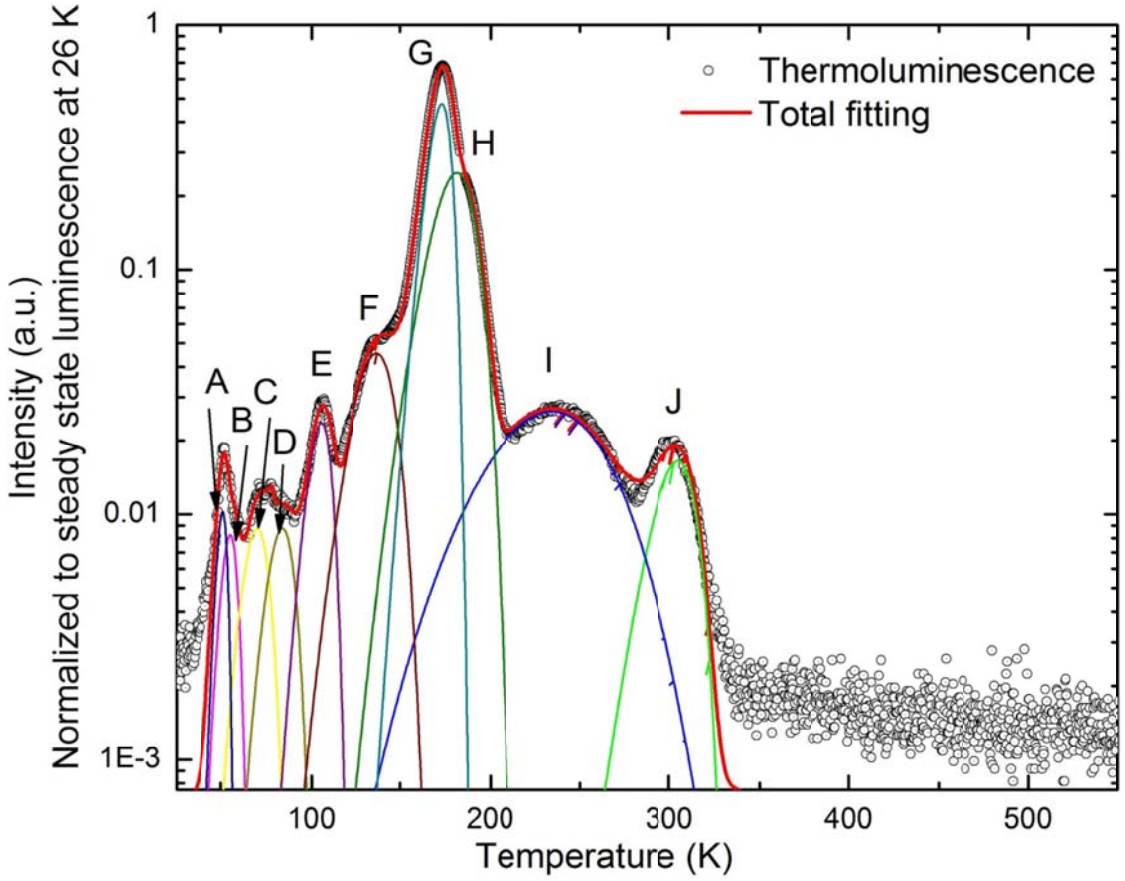

Figure 3.31 Thermoluminescence glow curve of $CsSrI_3$: 7% Eu^{2+}; thermoluminescence peaks were fit with the first-order kinetics model introduced by Randall and Wilkins

Table 3.9 Calculated charge carrier trap parameters

Trap	T_{max} *[K]*	n_0	*E [eV]*	*ln(s)* $[sec^{-1}]$	$\tau_{298\ K}$ *[s]*
A	51	0.52	0.063	12.23	5.78E-05
B	54	0.62	0.049	7.35	4.31E-03
C	66	1.04	0.050	4.62	6.86E-02
D	81	1.08	0.071	6.22	3.18E-02
E	105	2.51	0.138	11.86	1.55E-03
F	134	8.55	0.129	6.82	1.70E-01
G	173	49.19	0.408	24.14	2.72E-04
H	180	48.63	0.226	10.34	2.23E-01
I	194	14.83	0.117	0.31	7.14E+01
J	305	3.31	0.662	21.06	1.21E+02

The scintillation decay time of $CsSrI_3:Eu^{2+}$ is in the range from 1.7 μs to 3.4 μs. The trap with thermoluminescence peak at 51 K has a life time of 57.8 μs, which is one order of magnitude larger than the scintillation decay time of $CsSrI_3:Eu^{2+}$. This trap may contribute to long decay components in this material. However, due to its low concentration, this contribution would be limited.

The calculated charge carrier life times at room temperature for all other traps are orders of magnitude larger than the scintillation decay time of $CsSrI_3:Eu^{2+}$, including the two dominant thermoluminescence peaks at 173 K and 180 K. These traps may contribute to the afterglow of this material.

3.4.4. Summary and outlook

The new scintillation material $CsSrI_3$ doped with Eu^{2+} is a readily grow-able scintillator. This scintillation material is featured with a combination of high density (4.29 g/cm^3), high scintillation light output (73,000 ph/MeV under 662 keV γ-ray excitation) and high energy resolution (3.9% under 662 keV γ-ray excitation).

Bulk single crystal of $CsSrI_3:Eu^{2+}$ of 1" diameter has been successfully grown by Bridgman crystal growth method in vacuum sealed quartz ampoule. The crystal growth of $CsSrI_3$ does not require preparation of an orientated seed. The crystal of $CsSrI_3:Eu^{2+}$ is not prone to crack or cleave, which makes large diameter crystal growth of this material possible. The hygroscopic nature of $CsSrI_3:Eu^{2+}$ requires special encapsulation technique during crystal growth and hermetic packaging of the grown crystal, which might cause difficulties in future crystal production.

$CsSrI_3:Eu^{2+}$ shows high scintillation light output with excellent energy resolution, both of which are better or comparable to those of $LaBr_3:Ce^{3+}$. However, a major drawback for $LaBr_3:Ce^{3+}$ is that the crystal is reported to easily cleave during crystal growth [14]. $CsSrI_3:Eu^{2+}$ crystalizes readily and does not show tendency to cleave based on our observations. The scintillation decay time of $CsSrI_3:Eu^{2+}$is relatively slow compared to other commercially available

scintillators. This may limit this material in applications which request high count rate, such as Positron Emission Tomography.

CHAPTER IV SUMMARY AND CONCLUSIONS

I. Development of experimental apparatuses

A complete laboratory for raw materials handling, ampoule preparation, material rapid synthesis screening, single crystal growth, sample cutting, polishing and packaging of hygroscopic halide scintillation materials has been successfully established. The research scope of the Scintillation Materials Research Center has been expanded beyond the traditional Czochralski crystal growth of inert scintillation materials by this work.

The ampoule preparation system is designed for proper preparation of quartz ampoules for melt synthesis and crystal growth of hygroscopic materials. The system is capable of drying or melting raw materials under at least 10^{-6} mBar vacuum and a H_2-O_2 torch was used to seal the ampoules under vacuum. Specially designed ampoules for melt synthesis and crystal growth have been fabricated in order to grow halide single crystals of highest purity and optical quality. A hermetic packaging device has been also designed to facilitate optical and scintillation characterizations of halide materials in room atmosphere.

Two gloveboxes, an MBraun Unilab glovebox and a LC technology benchtop glovebox, have been purchased and set up for raw materials handling and sample preparation. An Electro-Dynamic Gradient furnace (Mellen 24-zone Electro-Dynamic Gradient furnace) has been purchased and modified in order to perform both Vertical Gradient Freeze crystal growth and Bridgman crystal

growth. Crystal growth parameters have been optimized for single crystal growth of $CsSrI_3:Eu^{2+}$. A diamond wire saw (South Bay Technology 810) has been purchased and integrated with the benchtop glovebox for cutting of hygroscopic halide crystals.

II. Development of screening techniques for halide scintillation materials

A process for rapid screening of new halide scintillation materials has been established. Based on appropriate selection rules, candidate materials in Alkali Halide – Rare Earth Halide ($AX–REX_3$), Alkali Halide – Alkaline Earth Halide ($AX–AEX_2$) and Alkaline Earth Halide – Rare Earth Halide ($AEX_2–REX_3$) binary systems have been selected and synthesized in evacuated quartz ampoules by small quantity. Scintillation measurements including scintillation light output, scintillation decay time and X-ray excited luminescence have been carried out on each composition to evaluate their potential in radiation detection applications.

A total of 42 Ce^{3+} or Eu^{2+} activated binary halide scintillation material candidates were synthesized and characterized for new scintillation materials discovery. Among all synthesized candidates, 15 candidate materials were found to be highly promising in terms of high scintillation light output, fast scintillation decay or desirable emission wavelength.

III. Single crystal growth of selected candidate materials

Three most promising candidates have been selected for single crystal growth and further development. Single crystals of Cs_3EuI_5, $CsGd_2Cl_7$: 3% Ce^{3+},

$CsSrI_3$:1% Eu^{2+}, $CsSrI_3$:7% Eu^{2+} and $CsSrI_3$:8% Eu^{2+} have been successfully grown to further evaluate these candidate materials in single crystal form. Bridgman and Vertical Gradient Freeze methods have been applied in single crystal growth practices. The binary halide $CsSrI_3$:Eu^{2+} crystalized readily. Large diameter $CsSrI_3$:Eu^{2+} single crystals (both ½" and 1" diameter) have been successfully grown by the custom-designed crystal growth apparatuses using either Bridgman or Vertical Gradient Freeze methods. No noticeable difference in crystal quality has been observed for $CsSrI_3$:Eu^{2+} crystals grown by Bridgman and Vertical Gradient Freeze methods.

IV. Characterizations of single crystal candidate materials

Optical and scintillation properties of candidate materials have been characterized to explore the potential of these materials in radiation detection applications like high resolution γ-ray spectroscopy, thermal neutron detection, medical imaging and homeland security.

Cs_3EuI_5 shows good scintillation light output (39,000 ph/MeV, with 10% energy resolution under 662 keV γ-ray excitation), favorable emission wavelength for conventional photomultiplier tube (463 nm) and is readily grow-able. UV and X-ray excited spectra suggest the emission from Cs_3EuI_5 is solely from Eu^{2+} 4d-5f transition. Good scintillation light output and ease of crystal growth make this material very promising for γ ray spectroscopy related security applications and Single Photon Emission Computed Tomography. However, the principal scintillation decay time of Cs_3EuI_5 is relatively slow (~ 4 μs). This would

limit this material in applications which requires fast scintillation response like Positron Emission Tomography and well-logging.

$CsGd_2Cl_7:Ce^{3+}$ exhibits good scintillation properties under γ ray excitation such as high light output (38,000 ph/MeV with 10% energy resolution under 662 keV γ-ray excitation) and fast principal scintillation decay (60 ns). Due to the presence of Gd, $CsGd_2Cl_7:Ce^{3+}$ can as well work as a thermal neutron detector. The detection of thermal neutrons was confirmed by using a moderated ^{252}Cf source. $CsGd_2Cl_7:Ce^{3+}$ crystals have a layered structure with weak cleavage planes. It is likely that a refined crystal growth technique in which an oriented seed is used to control crystallization in a preferred direction will be beneficial for crystal quality and scintillation performance.

$CsSrI_3:Eu^{2+}$ is featured with a combination of high density (4.29 g/cm^3), high scintillation light output (73,000 ph/MeV under 662 keV γ-ray excitation and excellent energy resolution (3.9% under 662 keV γ-ray excitation). The scintillation light output and energy resolution are comparable to that of the commercially available $LaBr_3:Ce^{3+}$ [10]. Unlike $LaBr_3:Ce^{3+}$, $CsSrI_3:Eu^{2+}$ crystalizes readily and is not prone to cracking. Characterizations also show that $CsSrI_3:Eu^{2+}$ has good scintillation proportionality and moderate hygroscopicity.

V. Thermal quenching effect and charge carrier traps in $CsSrI_3:Eu^{2+}$

Thermal quenching studies show the Eu^{2+} luminescence in $CsSrI_3$ is relatively stable at temperatures below ~ 400 K. But for temperature above 400 K, the luminescence efficiency of this material drops significantly. The light is almost

completely quenched when temperature reaches 600 K. This limits $CsSrI_3:Eu^{2+}$ in applications which require luminescence stability at elevated temperature, e.g. well-logging. The thermal activation energy for the thermal quenching effect in $CsSrI_3:Eu^{2+}$ is 0.75 eV.

Thermoluminescence studies show a complex glow peak structure from 50 K to 350 K with two dominant peaks located at 173 K and 180 K. This indicates there are multiple defect-related charge carrier traps in the lattice of $CsSrI_3:Eu^{2+}$. It is possible that these defects are partially induced by the high concentration Eu^{2+} dopant. On the other hand, the calculated trap life times for these traps are at least one order of magnitude longer than the measured scintillation decay time of $CsSrI_3:Eu^{2+}$. These traps may contribute to the possible afterglow of this material.

VI. Potential of $CsSrI_3:Eu^{2+}$ in various radiation detection applications

The combination of extraordinary scintillation light output (73,000 ph/MeV) and excellent energy resolution (3.9%) makes $CsSrI_3:Eu^{2+}$ highly competitive in applications like Single Photon Emission Computed Tomography (SPECT) and homeland security related radiation spectroscopy application. Both applications require the detector material to have high scintillation light output and energy resolution. Table 4.1 and 4.2 summarize the scintillation properties of $CsSrI_3$ doped with 7% Eu^{2+} compared with commercially available scintillation materials [38, 49, 68-70].

The scintillation material which is commonly used for Single Photon Emission Computed Tomography (SPECT) is NaI:Tl^+. The energy resolution achieved with a $CsSrI_3:Eu^{2+}$ single crystal (3.9%) is already much better than that of NaI:Tl^+ (7.1%). The density of $CsSrI_3:Eu^{2+}$ (4.29 g/cm^3) is also higher than that of NaI:Tl^+ (3.67 g/cm^3). If we calculate the attenuation length for 140 keV γ-ray in these two materials, which is the γ-rays (from ^{99m}Tc) conventionally used in a SPECT scan, the attenuation length for 140 keV γ-ray in $CsSrI_3:Eu^{2+}$ in ~20% shorter than in NaI:Tl^+. This means $CsSrI_3:Eu^{2+}$ has even higher detection efficiency than NaI:Tl^+, which would eventually reduce the amount of dose which a patience receives on one SPECT scan.

For homeland security related radiation spectroscopy applications, though $CsSrI_3:Eu^{2+}$ is slightly less dense than $LaBr_3:Ce^{3+}$ (5.29 g/cm^3), the effective atomic number of $CsSrI_3:Eu^{2+}$ (52) is higher than that of $LaBr_3:Ce^{3+}$ (47). The calculated photoelectric fraction of 511 keV γ-ray interacting with $CsSrI_3:Eu^{2+}$ is also slightly higher than that of $LaBr_3:Ce^{3+}$, which means $CsSrI_3:Eu^{2+}$ is capable of producing more photoelectrons under certain amount of energy deposition. Except for the difference in scintillation decay time, which is usually not the major concern in spectroscopy applications, $CsSrI_3:Eu^{2+}$ is comparable in most aspects with $LaBr_3:Ce^{3+}$. The biggest advantage of $CsSrI_3:Eu^{2+}$ is that this crystal is much easier to grow comparing to $LaBr_3:Ce^{3+}$. $CsSrI_3:Eu^{2+}$ is not prone to cracking and does not require an oriented seed crystal for single crystal growth. This significant difference will results in a major reduction in production cost. In

addition, unlike $LaBr_3:Ce^{3+}$ there is no rare earth elements in the constituent of $CsSrI_3:Eu^{2+}$. It is much less affected by the recent global rare earth shortage, which will potentially drive the production cost down in the foreseeable future.

Scaled-up crystal growth of multi-inch diameter $CsSrI_3:Eu^{2+}$ should be performed in order to fully evaluate the production cost of this promising scintillator. Materials purification techniques, like zone-refining, can also be applied to further improve the transparency of $CsSrI_3:Eu^{2+}$. This will result in additional improvement in the scintillation properties and make $CsSrI_3:Eu^{2+}$ more competitive in various radiation detection applications.

Table 4.1 Summary of scintillation characteristics of $CsSrI_3:Eu^{2+}$ compared with commercially available scintillators

Scintillator	***Density (g/cm^3)***	***Effective Atomic Number***	***Light Output (ph/MeV)***	***Energy Resolution at 662 keV***	***Scintillation Decay Time (ns)***	***Emission (nm)***
$CsSrI_3:Eu$	4.29	52	73,000	3.9%	3200	455
BGO	7.13	75	8200	9.0%	300	480
NaI:Tl	3.67	51	38,000	7.1%	230	415
$LaBr_3:Ce$	5.29	47	61,000	2.9%	30	380
$Lu_2SiO_5:Ce,Ca$	7.40	66	38,000	8.0%	37	420

Table 4.2 Summary of scintillation characteristics of $CsSrI_3:Eu^{2+}$ compared with commercially available scintillators – cont'd

Scintillator	***Attenuation Length for 140 keV γ (mm)***	***Photoelectric Fraction for 140 keV γ***	***Attenuation Length for 511 keV γ (mm)***	***Photoelectric Fraction for 511 keV γ***
$CsSrI_3:Eu^{2+}$	3.3	85%	2.6	20%
BGO	1.0	92%	1.2	39%
$NaI:Tl^+$	4.2	83%	3.1	18%
$LaBr_3:Ce^{3+}$	3.7	78%	2.2	14%
$Lu_2SiO_5:Ce^{3+}$	1.1	91%	1.2	34%

LIST OF REFERENCES

[1] T.A. Edison, Nature, 53 (1896) 470.
[2] W.C. Röngten, Nature, 53 (1896) 274-276.
[3] R. Hofstadter, Phys. Rev., 74 (1948) 100.
[4] R. Hofstadter, Phys. Rev., 75 (1948) 796.
[5] M.J. Weber, R.R. Monchamp, Journal of Applied Physics, 44 (1973) 5495-5499.
[6] B.A. L3. Collaboration, et al., Nucl. Instrum. Methods A, 289 (1990).
[7] C.L. Melcher, J.S. Schweitzer, Nuclear Instruments and Methods in Physics Research Section A: Accelerators, Spectrometers, Detectors and Associated Equipment, 314 (1992) 212-214.
[8] C.L. Melcher, US patent No 4958080, (1990).
[9] e.a. K. Wienhard, 2000 IEEE NSS-MIC Conference Record, 17 (2001) 2-6.
[10] E.V.D. van Loef, P. Dorenbos, C.W.E. van Eijk, K. Krämer, H.U. Güdel, Applied Physics Letters, 79 (2001) 1573.
[11] R. Hofstadter, Europium activated strontium iodide scintillators, US Patent 3,373,279, 1968.
[12] N.J. Cherepy, G. Hull, A.D. Drobshoff, S.A. Payne, E. van Loef, C.M. Wilson, K.S. Shah, U.N. Roy, A. Burger, L.A. Boatner, W.-S. Choong, W.W. Moses, Appl. Phys. Lett., 92 (2008) 083508-083503.
[13] M.J. Weber, Journal of Luminescence, 100 (2002) 35-45.
[14] W.M. Higgins, A. Churilov, E. van Loef, J. Glodo, M. Squillante, K. Shah, Journal of Crystal Growth, 310 (2008) 2085-2089.
[15] J.C. van't Spijker, P. Dorenbos, C.W.E. van Eijk, K. Kramer, H. Gudel, Proceedings of the International Conference on Inorganic Scintillators and their Applications, (1996) 411.
[16] K.S. Shah, L. Cirignano, R. Grazioso, M. Klugerman, P.R. Bennett, T.K. Gupta, W.W. Moses, M.J. Weber, S.E. Derenzo, Nuclear Science, IEEE Transactions on, 49 (2002) 1655-1660.
[17] E.D. Bourret-Courchesne, G. Bizarri, R. Borade, Z. Yan, S.M. Hanrahan, G. Gundiah, A. Chaudhry, A. Canning, S.E. Derenzo, Nucl. Instrum. Meth. A, 612 (2009) 138-142.
[18] E.D. Bourret-Courchesne, G. Bizarri, S.M. Hanrahan, G. Gundiah, Z. Yan, S.E. Derenzo, Nucl. Instrum. Meth. A, 613 (2010) 95-97.
[19] P. Dorenbos, J.C. van't Spijker, O.W.V. Frijns, C.W.E. van Eijk, K. Krämer, H.U. Güdel, A. Ellens, nucl. Instrum. Meth. B, 132 (1997) 728-731.
[20] H. Geiger, W. Müller, 16 (1928) 617-618.
[21] P.A. Rodnyi, in, CRC Press, New York, 2002.
[22] P. Lecoq, A. Annenkov, A. Gektin, M. Korzhik, C. Pedrini, Inorganic Scintillators for Detector Systems, Springer, Heidelberg, 2006.
[23] S. Shionoya, W.M. Yen, CRC Press, (1998) 192-193.
[24] G.H. Dieke, Aerican Institue of Physiscs Handbook, 3rd edition, McGraw-Hill, 1972.
[25] P. Dorenbos, Nucl. Instrum. Meth. A, 486 (2002) 208-213.

[26] H. Merenga, J. Andriessen, C.W.E. van Eijk, Radiation Measurements, 24 (1995) 343-346.
[27] U. Happek, S.A. Basun, J. Choi, J.K. Krebs, M. Raukas, Journal of Alloys and Compounds, 303-304 (2000) 198-206.
[28] H. Alterthum, Z. phys. Chem, 110 (1924).
[29] Y. Sun, S. Wang, Z. Qiao, M. Wang, Journal of Solid State Chemistry, 136 (1998) 134-136.
[30] J. Czochralski, Zeitschrift Fur Physikalische Chemie--Stochiometrie Und Verwandtschaftslehre, 92 (1917) 219-221.
[31] D.C. Stockbarger, Review of Scientific Instruments, 7 (1936) 133-136.
[32] P.W. Bridgman, Proceedings of the American Academy of Arts and Sciences, 60 (1925) 305-383.
[33] J.M. Parsey Jr, F.A. Thiel, Journal of Crystal Growth, 73 (1985) 211-220.
[34] S. Kyropoulos, Z. Anorg. Chem., 154 (1926) 308.
[35] D. Viechnicki, F. Schmid, Journal of Crystal Growth, 26 (1974) 162-164.
[36] C.P. Khattak, F. Schmid, Journal of Crystal Growth, 225 (2001) 572-579.
[37] D.C. Harris, in: R.W. Tustison (Ed.), SPIE, Orlando, FL, USA, 2009, pp. 730202-730212.
[38] E.V.D.v. Loef, P. Dorenbosa, C.W.E.v. Eijk, K.W. Kr.amer, H.U. Gudel, Nucl. Instrum. Meth. A, 486 (2002) 254-258.
[39] F. Moravec, M. Pelikán, Crystal Research and Technology, 20 (1985) 21-25.
[40] E.D. Bourret, J.B. Guitron, E.E. Haller, Journal of Crystal Growth, 85 (1987) 124-129.
[41] M. Moszynski, M. Kapusta, M. Mayhugh, D. Wolski, S.O. Flyckt, Nuclear Science, IEEE Transactions on, 44 (1997) 1052-1061.
[42] L.M. Bollinger, G.E. Thomas, Review of Scientific Instruments, 32 (1961) 1044-1050.
[43] C.D. Zerby, A. Meyer, R.B. Murray, Nuclear Instruments and Methods, 12 115-123.
[44] D.W. Aitken, B.L. Beron, G. Yenicay, H.R. Zulliger, Nuclear Science, IEEE Transactions on, 14 (1967) 468-477.
[45] S.W.S. McKeever, Thermoluminescence of solids, Page 1, Cambridge University Press, 1985.
[46] A.S. Voloshinovskii, V.B. Mikhailik, O.T. Antonjyak, P.A. Rodnyi, C.W.E. van Eijk, P. Dorenbos, G.F. Zimmerer, V. Mikhailin, Proceedings of the Fifth International Conference on Inorganic Scintillators and their Applications, Moscow, (1999) 492-496.
[47] H. Suzuki, T.A. Tombrello, C.L. Melcher, C.A. Peterson, J.S. Schweitzer, Nucl. Instrum. Meth. A, 346 (1994) 510-521.
[48] P.L. Reeder, Nucl. Instrum. Meth. A, 340 (1994) 371-378.
[49] G.F. Knoll, Radiation Detection and Measurement, fourth edition, Wiley, New York, (2010) 238.

[50] G. Schilling, G. Meyer, Zeitschrift für anorganische und allgemeine Chemie, 622 (1996) 759-765.
[51] C. Baopeng, W. Shihua, Z. Xinhua, J. Alloy. Compd., 181 (1992) 511-514.
[52] R. Guang-Ming, J. Sheng-Bang, W. Shihua, Acta Chimica Sinica, 53 (1995) 947-951.
[53] R.C. Weast, Handbook of Chemistry and Physics, 56th ed., CRC Press, 1975.
[54] K.S. Shah, J. Glodo, M. Klugerman, W.W. Moses, S.E. Derenzo, M.J. Weber, Nuclear Science, IEEE Transactions on, 50 (2003) 2410-2413.
[55] W.M. Higgins, J. Glodo, E. Van Loef, M. Klugerman, T. Gupta, L. Cirignano, P. Wong, K.S. Shah, J. Cryst. Growth, 287 (2006) 239-242.
[56] D.H. Gahane, N.S. Kokode, P.L. Muthal, S.M. Dhopte, S.V. Moharil, Optical Materials, 32 (2009) 18-21.
[57] T. Tröster, S. Schweizer, M. Secu, J.M. Spaeth, Journal of Luminescence, 99 (2002) 343-347.
[58] K. Winskiewski, S. Mahlik, M. Grinberg, H.J. Seo, Journal of Luminescence, 131 (2011) 306-309.
[59] T. Baby, V.P.N. Nampoori, Solid State Communications, 81 (1992) 367-369.
[60] Photomultiplier Tubes R2059 Datasheet, Hamamatsu Photonics.
[61] K. Yang, C.L. Melcher, P.D. Rack, L.A. Eriksson, IEEE Trans. Nucl. Sci., 56 (2009) 2960-2965.
[62] N.J. Cherepy, G.Hull, A.D. Drobshoff, S.A. Payne, E.V. Loef, C.M. Wilson, K.S. Shah, U.N. Roy, A. Burger, L.A. Boatner, W.S. Choong, W.W. Moses, Appl. Phys. Lett., 92 (2008).
[63] N.J. Cherepy, S.A. Payne, S.J. Asztalos, G. Hull, J.D. Kuntz, T. Niedermayr, S. Pimputkar, J.J. Roberts, R.D. Sanner, T.M. Tillotson, E.v. Loef, C.M. Wilson, K.S. Shah, U.N. Roy, R. Hawrami, A. Burger, L.A. Boatner, W.-S. Choong, W.W. Moses, IEEE Trans. Nucl. Sci., 56 (2009) 873-880.
[64] J. Glodo, E.V. van Loef, N.J. Cherepy, S.A. Payne, K.S. Shah, Nuclear Science, IEEE Transactions on, 57 (2010) 1228-1232.
[65] R.W. Gurney, N.F. Mott, Trans. Faraday Soc., 35 (1939) 69-73.
[66] P. Dorenbos, C.W.E.v. Eijk, A.J.J. Bos, C.L. Melcher, Journal of Physics: Condensed Matter, 6 (1994) 4167-4180.
[67] J.T. Randall, M.H.F. Wilkins, Proceedings of the Royal Society of London. Series A, Mathematical and Physical Sciences, 184 (1945) 365-389.
[68] T.K. Kumar, K.V. Reddy, Radiation Physics and Chemistry, 50 (1997) 545-553.
[69] M.A. Spurrier, P. Szupryczynski, K. Yang, A.A. Carey, C.L. Melcher, Nuclear Science, IEEE Transactions on, 55 (2008) 1178-1182.
[70] E. Sakai, Nuclear Science, IEEE Transactions on, 34 (1987) 418-422.

LIST OF PUBLICATIONS

Referred Journal Articles

[1] **K. Yang**, M. Zhuravleva, M. Urffer, L.F. Miller, C.L. Melcher, "Synthesis and scintillation properties of $CsGd_2Cl_7:Ce^{3+}$ for gamma-ray and neutron detection", *in press, Nuclear Instruments and Methods, A*, 2011

[2] **K. Yang**, M. Zhuravleva, C.L. Melcher, "Crystal growth and characterization of $CsSr_{1-x}Eu_xI_3$ high light yield scintillators", *physica status solidi (RRL) – Rapid Research Letters*, 5 (2011) 43-45.

[3] **K. Yang**, C.L. Melcher, M.A. Koschan, and M. Zhuravleva, "Effect of Ca co-doping on the Luminescence Centers in LSO:Ce Single Crystals", *IEEE Transactions on Nuclear Science*, 58 (2011) 3 1394-1399

[4] **K. Yang**, M. Zhuravleva, C.L. Melcher, "Crystal growth and scintillation properties of Cs_3EuI_5 crystals", *Journal of Crystal Growth*, 318 (2010) 833-835.

[5] **K. Yang**, C.L. Melcher, P.D. Rack, L.A. Eriksson, "Effects of Calcium Codoping on Charge Traps in LSO:Ce Crystals", *IEEE Transactions on Nuclear Science*, 56 (2009) 2960-2965.

[6] **K. Yang**, M.A. Spurrier, H. Rothfuss, L. Eriksson, C.L. Melcher, "The Effect of Calcium Co-Doping on Praseodymium Doped LSO", *IEEE Transactions on Nuclear Science*, 56 (2009) 968-971.

[7] M. Zhuravleva, **K. Yang**, C.L. Melcher, "Crystal growth and scintillation properties of Cs_3CeCl_6 and $CsCe_2Cl_7$", *Journal of Crystal Growth*, 318 (2011) 809-812.

[8] M. Zhuravleva, **K. Yang**, A. Green, C.L. Melcher, "Crystal growth and scintillation properties of Ce^{3+}-doped KGd_2Cl_7", *Journal of Crystal Growth*, 318 (2011) 796-799.

[9] M. Zhuravleva, **K. Yang**, M. Spurrier-Koschan, P. Szupryczynski, A. Yoshikawa, C.L. Melcher, "Crystal growth and characterization of LuAG:Ce:Tb scintillator", *Journal of Crystal Growth*, 312 (2010) 1244-1248.

[10] M.A. Spurrier, P. Szupryczynski, H. Rothfuss, **K. Yang**, A.A. Carey, C.L. Melcher," The effect of co-doping on the growth stability and scintillation properties of lutetium oxyorthosilicate", *Journal of Crystal Growth*, 310 (2008) 2110-2114.

[11] M.A. Spurrier, P. Szupryczynski, **K. Yang**, A.A. Carey, C.L. Melcher, "Effects of Ca^{2+} Co-Doping on the Scintillation Properties of LSO:Ce", *IEEE Transactions on Nuclear Science*, 55 (2008) 1178-1182.

Conference proceedings

[1] **K. Yang**, M. Zhuravleva, H. Rothfuss, C.L. Melcher, "Crystal Growth and Scintillation Properties of $AGd_2Cl_7:Ce^{3+}$ (A = Cs, K) for Gamma and Neutron Detection", *The Proceedings Of the 2010 IEEE Nuclear Science Symposium and Medical Imaging Conference, 2010*

[2] **K. Yang**, M. Zhuravleva, H. Rothfuss, C.L. Melcher, "Optical and Scintillation Properties of Single Crystal $CsSr_{1-x}Eu_xI_3$", *The Proceedings Of the 2010 IEEE Nuclear Science Symposium and Medical Imaging Conference, 2010*

[3] **K. Yang**, M. Zhuravleva, P. Szupryczynski, C.L. Melcher, "Temperature Response and Thermoluminescence of $SrI_2:Eu^{2+}$ Single Crystals" , *The Proceedings Of the 2010 IEEE Nuclear Science Symposium and Medical Imaging Conference, 2010*

[4] M. Zhuravleva, **K. Yang**, H. Rothfuss, C.L. Melcher, "Crystal growth and scintillation properties of Cs_3CeX_6 and $CsCe_2X_7$ (X = Cl, Br)", *The Proceedings Of the 2010 IEEE Nuclear Science Symposium and Medical Imaging Conference, 2010*

[5] **K. Yang**, C.L. Melcher, M. Zhuravleva, "Luminescence centers in Ca co-doped LSO:Ce crystals", *The Proceedings Of the 2009 IEEE Nuclear Science Symposium and Medical Imaging Conference, 2009*

[6] **K. Yang**, C.L. Melcher, P.D. Rack, L. Eriksson, "Effects of Calcium Co-doping on Charge Traps in LSO Crystals", *The Proceedings Of the 2007 IEEE Nuclear Science Symposium and Medical Imaging Conference, 2007*

Patent applications

[1] **K. Yang**, M. Zhuravleva, C.L. Melcher, and P. Szupryczynski, "Chloride scintillator for radiation detection", U.S. Patent Application *61/332,972,* European Patent Application 11165489.3-1218, 2010, *patent pending*

[2] **K. Yang**, M. Zhuravleva, C.L. Melcher, and P. Szupryczynski, "Iodide scintillators for radiation detection", U.S. Patent Application *61/332,945,* European Patent Application 11165485.1-1218*,* 2010, *patent pending*

[3] M. Zhuravleva, **K. Yang**, C.L. Melcher, and P. Szupryczynski, "Halide scintillator for radiation detection", U.S. Patent Application *61/332,934,* European Patent Application 11165494.3-1218, 2010, *patent pending*

[4] M. Zhuravleva, **K. Yang**, "New ternary Ca-containing halide scintillators for radiation detection", U.S. Patent Application 61/443,076, 2011, *patent pending*

VITA

Kan Yang was born on May 17th, 1983 in Hangzhou, China, to the parents of Shaoqing Yang and Yeqing Wu. He graduated from Shanghai Guangming high school in 2002. He then pursued his Bachelor of Engineering in Materials Science and Engineering at the Shanghai Jiao Tong University in Shanghai, China. After he obtained his B.E. in 2006, he moved to the United States and continued study in Materials Science and Engineering in the Scintillation Materials Research Center at the University of Tennessee, Knoxville. In 2009, Kan Yang received his Master of Science degree in Materials Science and Engineering at the University of Tennessee, Knoxville. On September 9th, 2010, Kan Yang was married to his wife, Xiang Wu. He completed his Doctor of Philosophy degree in Materials Science and Engineering in August 2011.